A DISCRETE TIME-DOMAIN ELECTROMAGNETICS FORMULATION WITH MINIMIZED NUMERICAL ARTIFACTS

by

Anastasios Panaretos

A Dissertation Presented in Partial Fulfillment
of the Requirements for the Degree
Doctor of Philosophy

ARIZONA STATE UNIVERSITY

May 2007

INFORMATION TO USERS

The quality of this reproduction is dependent upon the quality of the copy submitted. Broken or indistinct print, colored or poor quality illustrations and photographs, print bleed-through, substandard margins, and improper alignment can adversely affect reproduction.

In the unlikely event that the author did not send a complete manuscript and there are missing pages, these will be noted. Also, if unauthorized copyright material had to be removed, a note will indicate the deletion.

ProQuest Information and Learning Company
300 North Zeeb Road
P.O. Box 1346
Ann Arbor, MI 48106-1346

A DISCRETE TIME-DOMAIN ELECTROMAGNETICS FORMULATION WITH MINIMIZED NUMERICAL ARTIFACTS

by

Anastasios Panaretos

has been approved

April 2007

Graduate Supervisory Committee:

James T. Aberle, Co-Chair
Rodolfo E. Díaz, Co-Chair
George W. Pan
Abbas Abbaspour-Tamijani
Konstantinos S. Tsakalis

ACCEPTED BY THE DIVISION OF GRADUATE STUDIES

ABSTRACT

A class of finite-difference time-domain (FDTD) schemes is developed, for the solution of Maxwell's equations, that exhibits improved isotropy and dispersion characteristics. This is achieved by improving the two-dimensional Laplacian approximation associated with the curl-curl operator. The development of this method is based on the observation that in a two-dimensional space the Yee-algorithm approximates the aforementioned Laplacian operator via a strongly anisotropic 5-point representation. It is demonstrated that with the aid of a transversely extended curl operator any 9-point Laplacian can be mapped onto FDTD update equations. Our analysis shows that the mapping of an isotropic Laplacian approximation results in an isotropic and less dispersive FDTD scheme. The properties of the extended curl are further explored and it is proved that a unity Courant number can be achieved without the resulting scheme suffering from grid decoupling, an artifact of staggered-collocated grids. Then it is demonstrated that the above methodology is directly applicable in three-dimensions. The properties of the resulting schemes are analyzed and it is found that they exhibit the same favorable characteristics as their two-dimensional counterparts. Additionally, possible modifications for the extended curl operator are proposed which result in higher order performing schemes. First an alternative extended curl operator is derived based on a 25-point isotropic Laplacian discretization. It is shown that the corresponding scheme is fourth order accurate in space, exhibits isotropy up to sixth order and has a higher Courant number than other candidate schemes. Second, the extended-curl operator is combined with fourth order time derivatives via a modified equation approach. The resulting scheme is sixth order isotropic and exhibits a Courant number that is almost unity. Finally, a rigorous, simple and accurate methodology is described which allows the optimization of the original extended curl scheme for a given grid resolution. Representative numerical simulations are performed that validate the theoretically derived results.

To Vasilikoula, Hristos and Thanasis

'Αμμες δέ γ' ἐσσόμεσθα πολλῶ κάρρονες.

Πλουτάρχου *Βίοι*, *Λυκούργος* 21

We shall be sometime mightier men by far than everyone else.

Plutarch's Lives, Lycurgus 21

ACKNOWLEDGMENTS

I would like to express my gratitude to my advisors Dr. James T. Aberle and Dr. Rodolfo E. Díaz for their trust, guidance and generous financial support. My appreciation is extended to the other members of my committee Dr. George W. Pan, Dr. Abbas Abbaspour-Tamijani and Dr. Konstantinos S. Tsakalis for their valuable discussions and advices.

Particularly, I am grateful to Dr. Rodolfo E. Díaz for helping me during the course of my studies both at an academic as well as at a personal level. The discussions we had on several subjects helped me understand better electromagnetics and finite difference methods, but also motivated me and kept me optimistic, during the challenging and difficult moments of my research.

Also, I wish to thank my colleagues of the MWILAB Richard Ormeno, Ben Butler, Richard Lebaron and Kivanc Inan, as well as Sung-Hoon Oh, Kyong-Hwa Bae, Hyungsoo Kim, and Robert Romak for their support, and personal friendship which extended far beyond our common working environment.

Finally, I would like to thank and express my deep appreciation to my mother Vasiliki, my father Hristos and my brother Thanasis for their love, support and continuous encouragement.

This project was funded by DARPA. The author would like to thank Dr. Ben Mann, DARPA-DSO, and Dr. Reza Malek-Madani, ONR, for their continued interest and support of this project.

TABLE OF CONTENTS

Page

LIST OF TABLES x

LIST OF FIGURES xi

1 INTRODUCTION 1

2 AN INTRODUCTION TO THE FINITE-DIFFERENCE TIME-DOMAIN METHOD . 5

2.1. Basic principles 5

2.2. The Yee grid 6

2.3. Numerical dispersion 9

2.4. Stability 12

2.5. Absorbing boundary conditions 12

3 TWO DIMENSIONAL EXTENDED-CURL SCHEMES 18

3.1. Introduction 18

3.2. Motivation 19

3.3. Formulation 22

3.4. Stability and dispersion analysis 27

3.5. Extended-curl realizations for a higher Courant number 30

3.6. Anisotropy and dispersion error 33

3.7. Some remarks on the conservation properties of the extended curl scheme 37

3.8. Numerical Examples 39

3.8.1. Free space propagation 39

3.8.2. Cavity resonances 42

CHAPTER Page

3.8.3. Radiation pattern 44

3.8.4. Waveguide propagation constant 46

3.8.5. Scattering width 48

3.9. Maximization of $S_x^2 C_y + S_y^2 C_x$ 51

4 THREE DIMENSIONAL EXTENDED-CURL SCHEMES 53

4.1. Introduction 53

4.2. Formulation 53

4.3. Stability analysis 58

4.4. Dispersion analysis 62

4.5. Extended-curl and grid decoupling 65

4.6. Numerical experiments 68

4.7. Maximization of $S_x^2 C_y C_z + S_y^2 C_x C_z + S_z^2 C_x C_y$ 74

5 HIGHER ORDER EXTENDED-CURL SCHEMES 77

5.1. Introduction 77

5.2. A higher order Laplacian realization 78

5.2.1. Formulation 78

5.2.2. Dispersion and stability analysis of the HOL-based scheme 81

5.3. A higher order isotropic FDTD scheme using artificial dispersion via controllable higher order time derivatives 86

5.3.1. Motivation 86

5.3.2. Formulation 87

5.3.3. Dispersion and stability analysis 90

CHAPTER Page

5.4. Numerical examples 92

6 PERFORMANCE OF EXTENDED CURL SCHEMES FOR A FIXED GRID RESOLUTION 97

6.1. Introduction 97

6.2. A brief introduction to the diakoptics technique 98

6.3. Diakoptics implementation in the finite-difference time-domain method 99

6.3.1. A simple example 100

6.4. Single frequency optimization of 2-D extended curl schemes 102

6.4.1. Formulation 102

6.4.2. Stability and dispersion 109

6.5. Single frequency optimization of 3-D extended curl schemes 116

6.5.1. Formulation 116

6.5.2. Stability and dispersion analysis 121

6.6. Numerical examples 121

7 CONCLUSIONS AND FUTURE WORK 126

REFERENCES 129

LIST OF TABLES

Table		Page
3.1	Comparison of the most representative extended-curl realizations.	34
3.2	L_2 error comparisons for radiation pattern predictions.	44
3.3	L_2 error comparisons for scattering width predictions of a dielectric cylinder. . . .	51
4.1	The most representative three dimensional extended-curl schemes.	63

LIST OF FIGURES

Figure		Page
2.1	Yee grid. (a) **E** field components. (b) **H** field components.	7
2.2	Numerical phase velocity anisotropy for two different resolutions.	11
2.3	TM_Z wave impinging on a PML half space.	13
2.4	Conductivity profile.	15
2.5	PML performance. (a) Normalized total energy. 2-D domain (TE_Z). (c) Normalized total energy. 3-D domain .	17
3.1	Curl-curl approximation in the Yee scheme.	21
3.2	Update equations' modification for a 9-point Laplacian representation. The thick arrows indicate curl-related components between the first half time-step.	24
3.3	Determination of parameters α and β.	31
3.4	Alternative extended-curl realization.	32
3.5	Normalized phase velocity.	35
3.6	Maximum dispersion error.	36
3.7	Anisotropy error.	37
3.8	Pulse propagation in a 2-D domain with TE_Z fields. (a) Case 1. (b) Case 2.	40
3.9	Contour plots of pulse propagation in a 2-D domain with TE_Z fields. (a) Case 1. (b) Case 2.	41
3.10	Resonant frequency prediction error.	42
3.11	2-D cavity resonances. (a) Case 1 (Yee). (b) Case 2.	43
3.12	Radiation pattern predictions of two infinite current sources uniformly excited. Discretization $h = \lambda/6$.	45
3.13	Normalized propagation constant β/β_0 versus frequency.	47

Figure Page

3.14 Normalized propagation constant β/β_0 versus frequency. Case 3 48

3.15 Scattering width predictions of an infinite circular dielectric cylinder. 49

3.16 Scattering width predictions of an infinite circular dielectric cylinder. 50

4.1 Extended-curl stencil for E_z and H_z. 56

4.2 Determination of parameters α and β. 61

4.3 Normalized phase velocity. 64

4.4 Reformulated extended-curl discretization. 65

4.5 Numerical experiments. Cell-size $h = 1$ cm and $h/c = 0.03$ ns. (a) Excitation pulse frequency content. (b) Case 2. Notice that E_θ has been scaled to the elevation angle sine. 69

4.6 Numerical experiments. Cell-size $h = 1$ cm and $h/c = 0.03$ ns. (a) Case 1. (b) Case 3. Notice that E_θ has been scaled to the elevation angle sine. 70

4.7 (a) PEC boundary treatment. (b) Pulse propagation in parallel plate waveguide. . . 72

4.8 Bistatic radar cross-section (RCS) of a PEC sphere on the $y - z$ plane. ($a = 10h$, $h = \lambda/40$) 73

5.1 Higher order extended-curl discretization. The weights correspond to E_x components. Due to symmetry only half of them are denoted. The same weighting applies to E_y. 79

5.2 Maximum algebraic dispersion error. 82

5.3 (a) Maximum dispersion error. (b) Phase velocity velocity deviation. Optimization at $N_\lambda = 30$. 83

5.4 Anisotropy error. 85

5.5 Extended-curl stencil for H_z update. The E_x and E_y components are updated according to the Yee algorithm. 88

5.6 Additional components required for the approximation of $\partial_t^3 H_z$. 89

5.7 (a) Normalized phase velocity deviation versus propagation angle at $N_\lambda = 10$. (b) Anisotropy error versus cells per wavelength. 93

5.8 Maximum algebraic dispersion error. 94

5.9 (a) Resonant frequency prediction error. (b) 2-D cavity resonances computed by Fang (2,4). 95

5.10 (a) 2-D cavity resonances computed by HOL. (b) 2-D cavity resonances computed by extended-curl (4,2). 96

6.1 Electric circuit equivalent of a solution domain. 99

6.2 Multiport networks. (a) Initial network configuration. (b) The second multiport network has been replaced by its equivalent impulse response. 100

6.3 (a) Field components arrangement in the FDTD grid. (b) Implementation of FDTD diakoptics. 101

6.4 FDTD solution vs. diakoptics FDTD solution. 103

6.5 Optimal β versus grid resolution $N_\lambda = \lambda/h$ (2-D case). 107

6.6 Deviation of R with respect to its mean value versus angle of propagation ϕ. β optimal has been calculated for $\tilde{k}\,h = 2\,\pi/10$. 108

6.7 (a) Normalized phase velocity versus angle of propagation ϕ, at $N_\lambda = 10$. (b) Maximum dispersion error. 111

6.8 Anisotropy error. 112

6.9 Courant stability limit for the scaled scheme versus grid resolution N_λ. The calculation assumes $\beta = 1/12$. 113

6.10 (a) Normalized phase velocity versus angle of propagation ϕ, at $N_\lambda = 10$. (b) Maximum dispersion error. 115

6.11 Optimal β versus grid resolution $N_\lambda = \lambda/h$ (3-D case). 119

6.12 Deviation of R with respect to its mean value versus angle of propagation θ. β optimal has been calculated for $\tilde{k}\,h = 2\,\pi/10$. 120

6.13 (a) Anisotropy error. (b) Maximum dispersion error. 122

6.14 Plane wave injection error, $\beta = 1.12$. 124

6.15 Plane wave injection error, β optimized at $N_\lambda = 30$. 125

CHAPTER 1

INTRODUCTION

The Yee [1] algorithm is undoubtedly one of the most popular finite-difference approximations to Maxwell's equations, mainly due to its conceptual simplicity and ease to implement. Its main characteristic is that Maxwell's equations are treated in a coupled curl form, and in a leapfrog time-stepping manner. In addition the involved first order partial derivatives are approximated via second order accurate central finite differences, on a staggered spatio-temporal grid arrangement. Yet, the scheme suffers from numerical dispersion as well as phase velocity anisotropy [2]. Their deteriorating effects become very pronounced when the problems under study involve long integration times or results are required over a wide frequency range. Obviously, the naive approach to mitigate the effects of these drawbacks is to use finer grids, however this is not always feasible due to the increase of computational cost. Hence, despite its level of maturity the development of FDTD is still a topic that attracts a lot of attention, and efforts are made to expand its applicability and improve its accuracy.

The inherent dispersion and anisotropy errors of the Yee algorithm have so far stimulated a great research effort towards the development of improved FDTD schemes. The latter can be viewed as different flavors of the Yee algorithm since they retain many of its characteristics. The reasonable trend in order to tackle the dispersion and anisotropy errors is to employ higher order approximation to the first order partial derivatives. This path has been successfully followed by many researchers. Selectively we mention the work of Fang in [3] and Yefet and Petropoulos in [4], where second order accurate in time and fourth order accurate in space schemes were presented. Along similar lines Zygiridis and Tsiboukis in [5] as well as Sun and Trueman in [6] derived optimized versions of the Fang scheme by appropriately modifying the weights of the spatial derivatives' approximation.

Also Hadi and Piket-May in [7] attempted an improved (2,4) scheme by applying Ampere's law on several loops. An alternative formulation is the one presented by Young *et al.* in [8]. The proposed scheme combined compact finite-differences [9] for the spatial derivatives, with a Runge-Kuta integrator for time advancement. Of particular interest are those FDTD schemes developed on hexagonal grids, such as the one presented by Liu in [10] and recently by Xiao *et al.* in [11], which exhibit superior isotropy characteristics and reduced dispersion errors. Furthermore, in [12] dispersion error reduction was achieved by introducing artificial anisotropy in the regular FDTD update equations. This can be done through appropriate modification of the constitutive parameters of the modeled material. The material properties can be tuned and dispersion characteristics can be optimized with respect to a single frequency. Finally Wang and Teixeira in a series of papers [13–17] gave an elaborate analysis on how to eliminate the dispersion error over a certain frequency bandwidth or a particular angular span. Note that a detailed comparison of several low-dispersion schemes can be found in [18], while a very informative listing of past and current trends in FDTD improvement can be found in [19]. A very detailed overview of higher-order time-domain methods has been given by Hesthaven in [20].

The work presented in this dissertation examines the performance of FDTD schemes from a different standpoint. This approach is motivated by the fact that Maxwell's equations essentially propagate electromagnetic waves through the curl-curl operator, whose fundamental element is the two-dimensional transverse Laplacian operator. The importance of the Laplacian term for accurate modeling of wave propagation phenomena has been demonstrated in [21], where it was shown that in the case of the 2-D scalar wave equation, a more isotropic Laplacian representation ensures highly isotropic wave propagation. Unfortunately, since FDTD works with Maxwell's equations in individual curl form, the existence of this term is masked and hence its importance can be easily neglected. This is further supported by the fact that the Yee algorithm, during a time-step, indirectly

approximates the "hidden" Laplacian term via a strongly anisotropic 5-point representation. As lucidly demonstrated in the following Chapter this is solely responsible for the scheme's poor isotropy performance. Consequently, its amelioration is likely if the Laplacian term is approximated more accurately. Obviously since the direct mapping of a Laplacian approximation into FDTD updating in impossible, the goal is to improve the curl operator in FDTD in such a way that it yields indirectly a "good" and "as isotropic as possible" transverse Laplacian. It is demonstrated that with the aid of a *transversely extended curl* operator any 9-point Laplacian can be mapped onto FDTD update equations. Our analysis shows that this modified curl operator discretization results in a family of schemes with improved dispersion and isotropy characteristics.

The following remarks should be made regarding to the material of this dissertation. The presented approach should not be confused with those that approximate the 2-D and 3-D Maxwell's equations with the 2-D and 3-D scalar wave equations respectively. This is better justified from the 3-D formulation of our method, where the extended curl operators are defined with respect to the 3 transverse 2-D Laplacians and not by the 3-D one. Moreover the following guidelines were followed during the course of this research. First of all we were parsimonious with respect to the finite-difference stencil extension. Our main objective was to examine what is the best we can get by modifying, simple and as localized as possible finite-difference approximations. Second, the optimization of "exotic" stencils was avoided. For these cases there is the ultimate alternative, pseudospectral methods, which take into account the entire computational domain. In addition, optimization problems may not be challenging anymore as characteristically John von Neuman had mentioned: "With four parameters I can fit an elephant, and with five I can make him wiggle his trunk." [1] Third, we had to mathematically justify every suggested modification and by no means treat the scheme as a black box which obeys prescribed rules. Finally, it was desired to preserve

[1] Freeman Dyson, "A meeting with Enrico Fermi" (2004) Nature 427, p. 297

FDTD simplicity and hence make the resulting schemes easy to program and easy to incorporate in existing FDTD codes. Also it should be noted that throughout this document the second order accurate leapfrog scheme is adopted for time integration.

The outline of this dissertation is as follows. In Chapter 3 the implementation of an extended curl operator in 2-D finite-difference time-domain schemes is described. The appropriate stability and dispersion analyses are performed and their improved characteristics are demonstrated. The properties of the extended curl are further explored and it is proved that a unity Courant number can be achieved without the resulting scheme suffering from grid decoupling.

In Chapter 4 the extended curl operator is implemented for 3-D finite-difference time-domain schemes. As before a stability analysis is performed and the dispersion characteristics of the proposed scheme are investigated. It is shown that in this case the proposed scheme exhibits the same favorable characteristics as its 2-D counterpart.

The ability to achieve higher order performance by utilizing the extended-curl operator is examined in Chapter 5. Hence the mapping of a 25-point isotropic Laplacian on FDTD update equations is demonstrated, and it is shown that the corresponding scheme is fourth order accurate in space and exhibits isotropy up to sixth order. In addition a higher order isotropic FDTD scheme is described which combines an extended-curl discretization along with artificial dispersion terms, realized though weighted third order temporal derivatives.

Finally in Chapter 6 a simple and accurate methodology is described in order to achieve super-isotropic characteristics and eliminate the numerical dispersion of an extended curl operator based scheme. The methodology is rigorously developed for both 2-D and 3-D schemes and a detailed stability and dispersion analysis of the resulting schemes, is performed.

CHAPTER 2

AN INTRODUCTION TO THE FINITE-DIFFERENCE TIME-DOMAIN METHOD

2.1. Basic principles

Electromagnetic phenomena on the macroscopic scale are governed by Maxwell's equations which for a linear, isotropic and non-dispersive medium, can be written as:

$$\nabla \times \mathbf{E} = -\partial_t \mathbf{B} - \mathbf{J}_i^m - \sigma^* \mathbf{H} \tag{2.1}$$

$$\nabla \times \mathbf{H} = \partial_t \mathbf{D} + \mathbf{J}_i^e + \sigma \mathbf{E} \tag{2.2}$$

where the terms $\mathbf{J}_i^m$ and $\mathbf{J}_i^e$ correspond to the impressed magnetic and electric current sources, respectively. Notice that Maxwell's equations in their above form account for the existence of both lossy dielectric and magnetic material by including the corresponding conduction current terms, i.e. $\sigma \mathbf{E}$ and $\sigma^* \mathbf{H}$. If we move the temporal and spatial partially differentiated terms to opposite sides, then the system of (2.1) and (2.2) yields the following system of initial value problems:

$$\partial_t \mathbf{B} = -\nabla \times \mathbf{E} - \mathbf{J}_i^m - \sigma^* \mathbf{H} \tag{2.3}$$

$$\partial_t \mathbf{D} = \nabla \times \mathbf{H} - \mathbf{J}_i^e - \sigma \mathbf{E} \tag{2.4}$$

The above coupled system of equations forms the basis of the FDTD algorithm for solving, in the time-domain, three dimensional electromagnetic wave interaction problems. More precisely, the basic concept of FDTD is the solution of (2.3) and (2.4) in a discrete space and time. This requires that all temporal and spatial derivatives be approximated numerically using finite differences. Obviously the accuracy of the FDTD solutions depends on the accuracy of the finite difference schemes used. The latter is determined by calculating the local truncation error of the numerical approximation which is usually achieved by Taylor-expanding the appropriate quantities.

2.2. The Yee grid

In 1966 Kane Yee presented a set of finite difference equations for the system of Maxwell's equations [1]. This set of finite differences exist on a structured grid which consists of orthogonal parallelepipeds with a size of $\Delta x \times \Delta y \times \Delta z$, usually referred to as cells. A unit cell of Yee's grid along with the spatial arrangement of the field components is shown in Figs. 2.1(a) and 2.1(b). Notice that the electric and magnetic field components are staggered by a half cell size along each direction. Based on this spatial field arrangement Yee constructed centered second order finite difference approximations for the spatial derivatives. For example the partial derivative of E_y with respect to x is given by:

$$\partial_x E_{y,i+1/2} = \frac{E_{y,i+1} - E_{y,i}}{\Delta x} + \mathcal{O}(\Delta x^2) \tag{2.5}$$

Moreover, a similar staggering is applied in time where the electric field components are computed at integer time-steps $n\Delta t$, while the magnetic field components at $(n + 1/2)\Delta t$ time steps. Hence the partial derivative of E_y with respect to t is given by:

$$\partial_t E_y^{n+1/2} = \frac{E_y^{n+1} - E_y^{n-1}}{\Delta t} + \mathcal{O}(\Delta t^2) \tag{2.6}$$

This leapfrog time-stepping is a very desirable property of FDTD mostly because it is non-dissipative. For example, consider the case where the gain of an antenna or the scattering intensity of some object needs to be calculated. Any artificial dissipation will affect the radiated power, and results in erroneous predictions, especially if long integration times are involved. In addition the leap-frog scheme is fully explicit and hence the burden of matrix inversion is avoided. Conceptually the leapfrog scheme suggests that a "future" field value is predicted by the "present" one, plus the appropriate correction-source term. Hence, the field components are computed at each spatial point and then moved forward in time, in a time marching scheme also known as "update equations".

In what follows we derive the update equations for the E_z and H_z components. From (2.3)

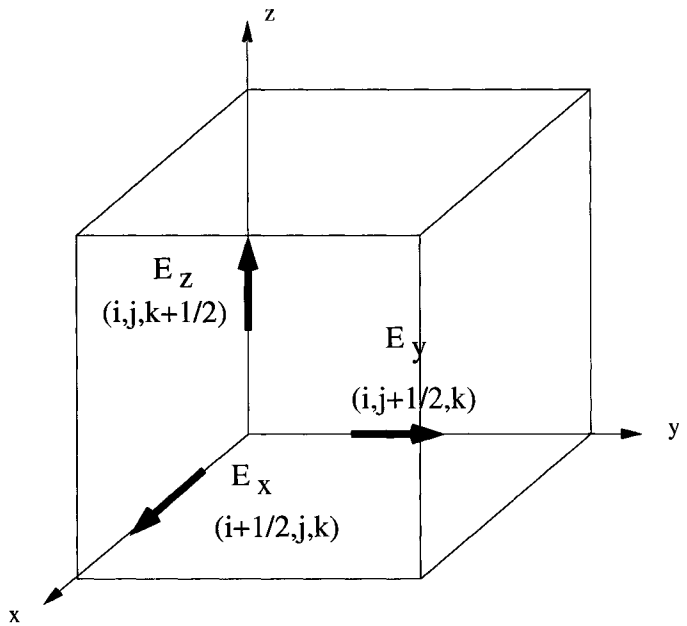

(a)

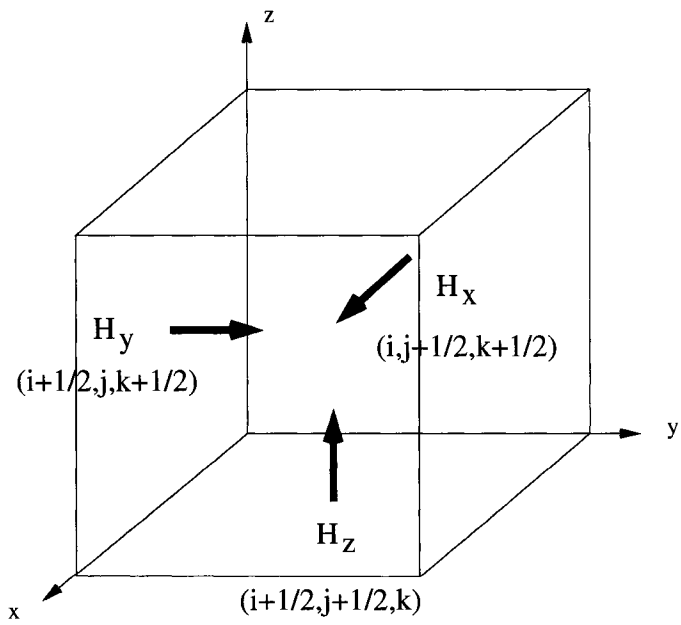

(b)

Fig. 2.1: Yee grid. (a) **E** field components. (b) **H** field components.

and (2.4) we have:

$$\partial_t E_z = \frac{1}{\varepsilon}\left(\partial_x H_y - \partial_y H_x - J^e_{z,i} - \sigma E_z\right) \tag{2.7}$$

$$\partial_t H_z = \frac{1}{\mu}\left(\partial_y E_x - \partial_x E_y - J^m_{z,i} - \sigma^* H_z\right) \tag{2.8}$$

Hence, according to the Yee-cell based FDTD conventions described previously, the corresponding update equations for these components are given by:

$$E_z\Big|^{n+1}_{i,j,k+1/2} = \frac{1-\frac{\sigma\Delta t}{2\varepsilon}}{1+\frac{\sigma\Delta t}{2\varepsilon}} E_z\Big|^{n}_{i,j,k+1/2} + \frac{\frac{\Delta t}{\varepsilon}}{1+\frac{\sigma\Delta t}{2\varepsilon}} \times$$
$$\times \left(\frac{H_y\Big|^{n+1/2}_{i+1/2,j,k+1/2} - H_y\Big|^{n+1/2}_{i-1/2,j,k+1/2}}{\Delta x} - \right.$$
$$\left. \frac{H_x\Big|^{n+1/2}_{i,j+1/2,k+1/2} - H_x\Big|^{n+1/2}_{i,j-1/2,k+1/2}}{\Delta y} - J^e_{z,i}\Big|^{n+1/2}_{i,j,k+1/2} \right) \tag{2.9}$$

$$H_z\Big|^{n+1/2}_{i+1/2,j+1/2,k} = \frac{1-\frac{\sigma^*\Delta t}{2\mu}}{1+\frac{\sigma^*\Delta t}{2\mu}} H_z\Big|^{n+1/2}_{i+1/2,j+1/2,k} + \frac{\frac{\Delta t}{\mu}}{1+\frac{\sigma^*\Delta t}{2\mu}} \times$$
$$\times \left(\frac{E_x\Big|^{n}_{i+1/2,j,k} - E_x\Big|^{n}_{i+1/2,j+1,k}}{\Delta y} - \frac{E_y\Big|^{n}_{i,j+1/2,k} - E_y\Big|^{n}_{i+1,j+1/2,k}}{\Delta x} - J^m_{z,i}\Big|^{n}_{i+1/2,j+1/2,k} \right) \tag{2.10}$$

The material properties involved in the update equations can in general be functions of space; consequently they have to be evaluated at the same spatial point as the updated quantity. For example, for the values of permittivity related to the E_z update equation we have:

$$\varepsilon(x,y,z) \equiv \varepsilon\Big(i\Delta x, j\Delta y, (k+1/2)\Delta z\Big) \tag{2.11}$$

Obviously the update equations for the other field components can be derived in a similar manner. The Yee cell is used consistently throughout this dissertation.

2.3. Numerical dispersion

The discrete nature of the numerical algorithms that solve Maxwell's equations using finite-difference approximations cause dispersion of the simulated wave modes in the computational grid. Therefore, in general, the group and phase velocities of a discrete propagating wave in the FDTD grid are different from the velocities of the same wave propagating in a continuous medium. The existence of numerical dispersion can severely deteriorate the accuracy of numerical results, and hence it must be dealt with. The dispersive nature of the FDTD algorithm and its mitigation is extensively analyzed in the following chapters. Hence, for completeness only the most important conclusions are mentioned here. A dispersion analysis can be performed by taking the spatio-temporal discrete Fourier transform of the the FDTD update equations, which is equivalent to substituting a solution of the form

$$u_{i,j,k}^{n} = \mathrm{e}^{\mathrm{j}\left(\omega n\Delta t - \tilde{k}_x i\Delta x - \tilde{k}_y j\Delta y - \tilde{k}_z k\Delta z\right)} \tag{2.12}$$

This procedure yields an equation that relates the numerical wavenumber $\tilde{k}$ to the wave frequency ω.

$$\left[\frac{1}{c\Delta t}\sin\left(\frac{\omega\Delta t}{2}\right)\right]^2 = \left[\frac{1}{\Delta x}\sin\left(\frac{\tilde{k}_x\Delta x}{2}\right)\right]^2 + \left[\frac{1}{\Delta y}\sin\left(\frac{\tilde{k}_y\Delta y}{2}\right)\right]^2 + \left[\frac{1}{\Delta z}\sin\left(\frac{\tilde{k}_z\Delta z}{2}\right)\right]^2 \tag{2.13}$$

where $c = 1/\sqrt{\mu\epsilon}$ is the velocity of light in the medium. Notice that in the case of a very fine discretization ($\Delta x, \Delta y, \Delta z \rightarrow 0$), the above equation yields:

$$\left(\frac{\omega}{c}\right)^2 \approx \tilde{k}_x^2 + \tilde{k}_y^2 + \tilde{k}_z^2 \tag{2.14}$$

which is the well know constraint equation that governs the propagation of a monochromatic wave, in a general 3-D medium. Qualitatively this suggests that numerical dispersion can be reduced to any desired degree if a fine enough mesh is employed.

An interesting result can be obtained if we rewrite Maxwell's equations in matrix form. It is

$$\begin{bmatrix} \mathbf{T} & \frac{1}{\varepsilon}\mathbf{C} \\ -\frac{1}{\mu}\mathbf{C} & \mathbf{T} \end{bmatrix} \begin{bmatrix} \mathbf{E}^0 \\ \mathbf{H}^0 \end{bmatrix} = \mathbf{0} \tag{2.15}$$

where $\mathbf{C}$ corresponds to the Fourier transform of the discrete curl operator given by

$$\mathbf{C} = \begin{bmatrix} 0 & -\frac{1}{\Delta z}\sin\left(\frac{\tilde{k}_z\Delta z}{2}\right) & \frac{1}{\Delta y}\sin\left(\frac{\tilde{k}_y\Delta y}{2}\right) \\ \frac{1}{\Delta z}\sin\left(\frac{\tilde{k}_z\Delta z}{2}\right) & 0 & -\frac{1}{\Delta x}\sin\left(\frac{\tilde{k}_x\Delta x}{2}\right) \\ -\frac{1}{\Delta y}\sin\left(\frac{\tilde{k}_y\Delta y}{2}\right) & \frac{1}{\Delta x}\sin\left(\frac{\tilde{k}_x\Delta x}{2}\right) & 0 \end{bmatrix} \tag{2.16}$$

$\mathbf{T}$ corresponds to the Fourier transform of the temporal finite differences, given by

$$\mathbf{T} = \frac{1}{\Delta t}\sin\left(\frac{\omega\Delta t}{2}\right)\mathbf{I}_{3\times 3} \tag{2.17}$$

and $\left[\mathbf{E}^0\ \mathbf{H}^0\right]^T = \left[E_x^0\ E_y^0\ E_z^0\ H_x^0\ H_y^0\ H_z^0\right]^T$. Now, if we multiply the first three equations in (2.15) by $\frac{1}{\Delta x}\sin\left(\frac{\tilde{k}_x\Delta x}{2}\right)$, $\frac{1}{\Delta y}\sin\left(\frac{\tilde{k}_y\Delta y}{2}\right)$, and $\frac{1}{\Delta z}\sin\left(\frac{\tilde{k}_z\Delta z}{2}\right)$ respectively, and then add the resulting equations by parts we obtain

$$\begin{aligned} &\frac{1}{\Delta t}\sin\left(\frac{\omega\Delta t}{2}\right)\times \\ &\times\left[\frac{1}{\Delta x}\sin\left(\frac{\tilde{k}_x\Delta x}{2}\right)\varepsilon E_x^0 + \frac{1}{\Delta y}\sin\left(\frac{\tilde{k}_y\Delta y}{2}\right)\varepsilon E_y^0 + \frac{1}{\Delta z}\sin\left(\frac{\tilde{k}_z\Delta z}{2}\right)\varepsilon E_z^0\right] = 0 \end{aligned} \tag{2.18}$$

The above relation is the spatio-temporal Fourier transform of the finite-difference approximation to Gauss' Law, or

$$\partial_t\nabla\cdot(\varepsilon E_x, \varepsilon E_y, \varepsilon E_z) = 0 \tag{2.19}$$

which essentially proves the flux-conservative nature of the Yee algorithm. In the same manner, one can prove the conservation of the magnetic flux.

Although numerical dispersion is introduced individually by the temporal and spatial discretization, the latter also introduces numerical phase velocity anisotropy. This artifact is described as the wave speed being a function of the propagation angle. Its effects are demonstrated, for a 2-D

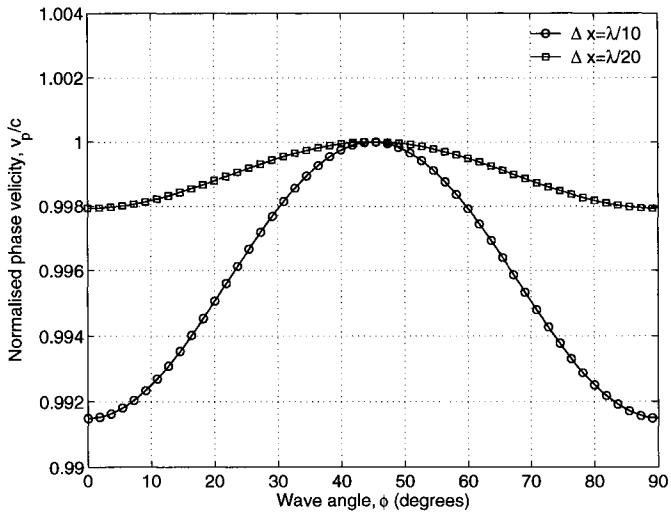

Fig. 2.2: Numerical phase velocity anisotropy for two different resolutions.

space, in Fig. 2.2. First of all it can be seen that anisotropy can be reduced by increasing the resolution. In addition, we observe that for this case the best approximation to propagation in a continuous medium can be achieved along the diagonal of the Yee cell ($\phi = 45°$). The same can be achieved in a 3-D grid for propagation along the long diagonal of the Yee cell, that is $(\phi, \theta) = (45°, 54.7°)$. This behavior is due to the fact that the order of the temporal and spatial errors are the same and opposite in sign. Hence, they can cancel each other and given that the maximum allowable time-step (Courant limit) is used, the numerical wave speed can acquire its physical value. This is a very favorable characteristic of the Yee algorithm which is not observed in alternative schemes with spatial accuracy higher than the temporal one. In these cases maximum accuracy at a specific frequency can be achieved if time-steps smaller than the Courant limit are used.

Furthermore, dispersion analysis reveals that the Yee grid exhibits characteristics similar to that of a low-pass filter, whose response is controlled by the grid sampling resolution $N_\lambda = \lambda/\Delta x$. Therefore, to obtain un-disrupted pulse propagation in an FDTD grid, its resolution should be chosen so that the frequencies of interest are far below this equivalent filter's cutoff frequency.

2.4. Stability

Finite difference schemes require the time increment Δt to have a specific bound relative to the spatial discretization Δx, Δy and Δz. This bound is necessary to prevent numerical instability, which is an undesirable property of explicit schemes. The derivation of this bound for Yee's algorithm is based on the von-Neumann stability criterion which results in the following condition:

$$\Delta t \leq \frac{1}{c\sqrt{\frac{1}{\Delta x^2}+\frac{1}{\Delta y^2}+\frac{1}{\Delta z^2}}} \tag{2.20}$$

This is usually referred to as the *Courant-Friedrichs-Lewy* (CFL) condition. Qualitatively the above condition suggests that in order to ensure the stability of a numerical scheme, for a hyperbolic equation, the temporal and spatial discretization have to be properly chosen so that we can "catch the fastest possible propagating wave"[1] in the grid. It has to be mentioned that the CFL condition is a necessary condition but not a sufficient one.

2.5. Absorbing boundary conditions

The most important issue for the development of the FDTD method has been the efficient and accurate solution of electromagnetic problems in unbounded regions. This requires the truncation of the computational domain with appropriate absorbing boundary conditions (ABCs). These boundary conditions should allow the outward propagating waves to exit the computational domain with as little reflection as possible. Several ABC schemes have been proposed so far with the one introduced by Mur [22] being the most popular and the most widely used. However these ABCs exhibit best performance only in particular cases, for instance if the impinging wave is plane and is incident normally upon the ABC boundary.

[1] A tactic initially introduced in the area of surfing!

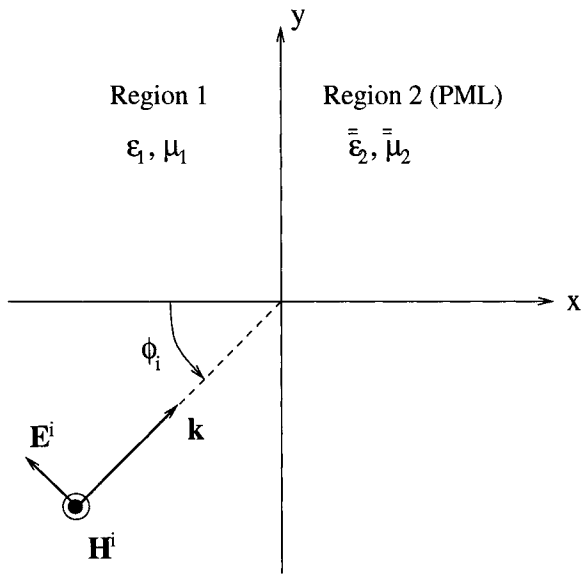

Fig. 2.3: TM_z wave impinging on a PML half space.

A major breakthrough in this area was made by Berenger when he introduced a highly effective ABC, usually referred to as the perfectly matched layer (PML) [23], [24], [25]. The PML can be considered as a lossy material that surrounds the problem domain, and it can absorb electromagnetic waves at arbitrary frequencies and angles of incidence. This is achieved by splitting the field components, inside the PML, into two orthogonal subcomponents. Hence, the waves impinging upon the PML, are decomposed into artificial plane waves traveling along the major axis. Then, by properly choosing the PML's electric and magnetic conductivity these plane waves can be attenuated, and ideally vanish.

For the studies documented in this dissertation, a PML based on a "lossy uniaxial medium" was implemented. This was initially proposed by Sacks *et al.* in the context of the Finite-Element-Method [26], and was later successfully extended for the FDTD method by Zhao and Cangellaris [27] as well as by Gedney [28]. This PML implementation has the advantage that it does not require field-splitting and hence its formulation is not based on a mathematical "trick", but rather on designing a medium with the appropriate material properties. In the aforementioned papers it

was shown that by properly choosing the material parameters of a uniaxial medium, the latter can be perfectly matched to free space for any angle of incidence, and at the same time attenuate the transmitted waves in it.

Although a very comprehensive analysis of this PML realization can be found in the previously mentioned papers, for completeness some of its details will be reported here. More precisely, with respect to the scattering scenario shown in Fig. 2.3, a reflectionless interface between Region 1 and Region 2 can be created if the permittivity and the permeability tensors of Region 2 are chosen to be:

$$\overline{\overline{\varepsilon}}_2 = \varepsilon_1 \begin{bmatrix} s_x^{-1} & 0 & 0 \\ 0 & s_x & 0 \\ 0 & 0 & s_x \end{bmatrix} \qquad \overline{\overline{\mu}}_2 = \mu_1 \begin{bmatrix} s_x^{-1} & 0 & 0 \\ 0 & s_x & 0 \\ 0 & 0 & s_x \end{bmatrix} \tag{2.21}$$

Furthermore, it is quite straightforward to show that, the wave velocities along the x-direction in Region 1 and Region 2 are related as shown below:

$$\beta_{2x} = s_x \beta_{1x} \tag{2.22}$$

Therefore, if we set $s_x = 1 + \frac{\sigma}{\mathrm{j}\omega\varepsilon_1}$ the wave velocity in Region 2 becomes:

$$\beta_{2x} = \left(1 + \frac{\sigma}{\mathrm{j}\omega\varepsilon_1}\right) \beta_{1x} = \beta_{1x} - \mathrm{j}\,\sigma\,\eta_1 \cos\phi_i \tag{2.23}$$

Consequently, the transmitted wave in the PML, along the x-axis normal to the interface between Regions 1 and 2, propagates with the same velocity as the incident wave, while simultaneously it gets attenuated. It has to be mentioned that the wave velocities along the y-axis are also identical, which stems from the fact that the two media are matched.

Of particular importance for the realization of an effective PML is the choice of the conductivity profile. The properties of the PML have been chosen so that the latter is perfectly matched to the solution domain medium in a continuous space. However the FDTD domain is inherently

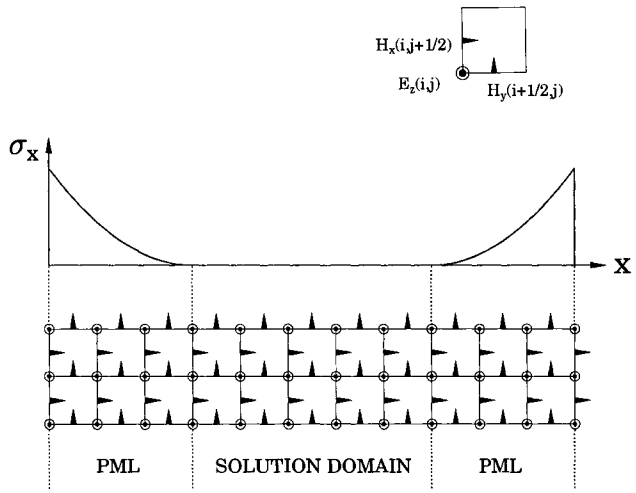

Fig. 2.4: Conductivity profile.

discrete and hence the electric and magnetic field components, along with the material properties, are spatially staggered. Therefore, a direct FDTD implementation of the PML without taking into account the staggering field component arrangement, will result in undesired reflections. To reduce this reflection error the PML losses along the direction normal to the interface should gradually rise from zero. More precisely the conductivity is chosen to vary spatially as:

$$\sigma_x(x) = \sigma_{max} \left(\frac{x}{d}\right)^m \tag{2.24}$$

where d is the PML depth and m is the order of the polynomial variation. A graphical representation of typical conductivity profile is shown in Fig. 2.4.

In what follows numerical experiments are presented that demonstrate the effectiveness of the PML. A 2-D domain, 100×50 cells long, was examined, as well as a 3-D one, $100 \times 50 \times 50$ cells long. In both cases space was uniformly discretised with a cell size of $\Delta x = 0.01$ m, and the maximum allowable time-step was chosen. The 2-D as well as the 3-D computational domains were excited at their centers by imposing a soft source condition on the H_z and E_z components, respectively. The excitation source was a Rayleigh pulse with significant frequency content up to

3 GHz. Two different PML thicknesses were examined (4 and 12 layers) and the theoretical reflection coefficient was set equal to $\ln R(0) = -12$. A parabolic conductivity profile was used with $m = 4$. After exciting the computational domain we let the waves propagate for a sufficient amount of time-steps, and we calculated the total stored energy with respect to time. The corresponding results are illustrated in Figs. 2.5(a) and 2.5(b), and evidently the uniaxial PML is very effective for the truncation of an FDTD grid.

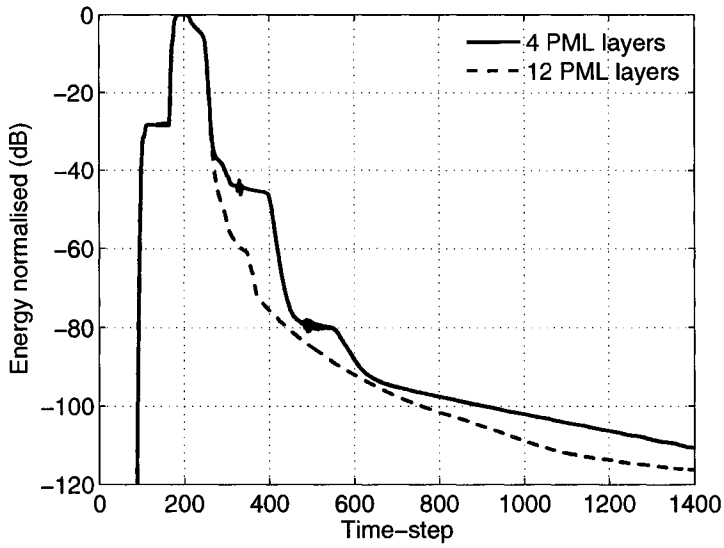

(a)

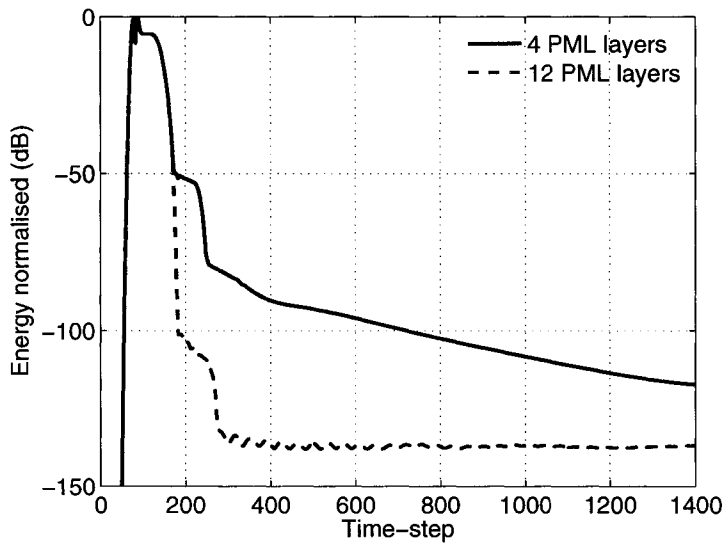

(b)

Fig. 2.5: PML performance. (a) Normalized total energy. 2-D domain (TE_z). (c) Normalized total energy. 3-D domain .

CHAPTER 3

TWO DIMENSIONAL EXTENDED-CURL SCHEMES

3.1. Introduction

In this Chapter the development and analysis of a two-dimensional (2-D) FDTD based on an extended-curl operator is presented. Our approach is motivated by the fact that Maxwell's equations essentially propagate electromagnetic waves throuh the curl-curl operator, whose fundamental element is the 2-D transverse Laplacian operator. Unfortunately, since FDTD works with Maxwell's equations in coupled curl form, the existence of this term is masked and hence its importance can be easily neglected. Furthermore, it can be shown that the Yee algorithm, during a time-step, indirectly approximates the "hidden" Laplacian term via a strongly anisotropic 5-point representation. As demonstrated in Section 3.2, this is solely responsible for the scheme's poor isotropy performance. Consequently, amelioration of this problem is expected if the Laplacian term is approximated more accurately. Obviously since the direct mapping of a Laplacian approximation into FDTD updating is impossible, the goal is to improve the curl operator in FDTD in such a way that it yields indirectly a "good" and "as isotropic as possible" transverse Laplacian.

The development presented here will proceed as follows: In Section 3.3 it is shown that in a 2-D space, only the curl operator that lies on the same plane with the transverse Laplacian needs to be modified resulting in what we refer to as the extended curl operator. As further demonstrated in Section 3.3, the latter allows mapping of any 9-point Laplacian onto FDTD update equations. The scheme that corresponds to the most isotropic 9-point Laplacian is shown to be characterized by superior isotropy, less dispersion, and a higher Courant number. Moreover, further experimentation with the extended-curl schemes reveals that a unity Courant number can be supported (Section 3.5). As a matter of fact there is an infinite number of extended-curl realizations that exhibit this feature.

3.2. Motivation

The approach presented herein stems from the fact that Maxwell's equations, in the case of a linear, isotropic, and homogeneous medium, propagate electromagnetic waves essentially through the curl-curl ($\nabla \times \nabla \times$) operator as seen in the well-known vector wave equation:

$$\nabla \times \nabla \times \mathbf{E} = -\mu \varepsilon \partial_{tt}^2 \mathbf{E} \tag{3.1}$$

In the general case of a divergenceless field, the curl-curl operator can be separated explicitly into a transverse Laplacian and cross terms. For instance, taking the z-component of (3.1) we have:

$$-\mu \varepsilon \partial_{tt}^2 E_z = (\nabla \times \nabla \times \mathbf{E})_z = \partial_z (\partial_x E_x + \partial_y E_y) - \nabla_{xy}^2 E_z \tag{3.2}$$

It can be seen that the right hand side of (3.2) consists of two terms, one of which is a 2-D Laplacian, transverse to the direction of the component under consideration. Therefore, it can be concluded that the 2-D Laplacian is a fundamental element of the 3-D curl-curl operator, or that the 2-D Laplacian is implicit in the two successive curl operations.

Here, we consider a two-dimensional space and a transverse, with respect to z, electric (TE_Z) field polarization. (The same analysis can be carried out for the TM_Z case as well.) For the 2-D TE_Z case, the time-domain Maxwell's equations are given by:

$$\partial_t H_z = \frac{1}{\mu} (\partial_y E_x - \partial_x E_y) \tag{3.3}$$

$$\partial_t E_x = \frac{1}{\varepsilon} \partial_y H_z \tag{3.4}$$

$$\partial_t E_y = -\frac{1}{\varepsilon} \partial_x H_z \tag{3.5}$$

The most popular discrete approximation to this set of equations is the finite-difference time-domain (FDTD) method introduced by Yee [1], and later expanded and refined by various researchers [2,29]. The method assumes a staggered field arrangement both in space and time; it employs second order accurate central finite differences for the approximation of spatial derivatives, and the leap-frog

scheme for time integration. The corresponding equations comprise what is referred to as the "Yee-scheme" or conventional FDTD, and they are given by:

$$\delta_t H_z\Big|_{i+\frac{1}{2},j+\frac{1}{2}}^{n+1} = \frac{1}{\mu}\left(\delta_y E_x\Big|_{i+\frac{1}{2},j+\frac{1}{2}}^{n+1} - \delta_x E_y\Big|_{i+\frac{1}{2},j+\frac{1}{2}}^{n+1}\right) \tag{3.6}$$

$$\delta_t E_x\Big|_{i+\frac{1}{2},j}^{n+\frac{1}{2}} = \frac{1}{\varepsilon}\delta_y H_z\Big|_{i+\frac{1}{2},j}^{n+\frac{1}{2}} \tag{3.7}$$

$$\delta_t E_y\Big|_{i,j+\frac{1}{2}}^{n+\frac{1}{2}} = -\frac{1}{\varepsilon}\delta_x H_z\Big|_{i,j+\frac{1}{2}}^{n+\frac{1}{2}} \tag{3.8}$$

where

$$\delta_x u_i = \frac{u_{i+\frac{1}{2}} - u_{i-\frac{1}{2}}}{\Delta x} \tag{3.9}$$

Due to the two-stage "time-marching" nature of the leap-frog scheme, equations (3.6), (3.7) and (3.8) are referred to as the "FDTD update equations" for conventional FDTD. Notice that in this formulation Maxwell's equations are treated as a first order system of two coupled curl equations. Evidently, the existence of the Laplacian term is masked, meaning that the latter is not directly computed during an FDTD calculation. Conceptually, the indirect generation of the Laplacian approximation means that the Yee-scheme Laplacian results by default and not by purposeful choice. In what follows the accuracy of this approximation is examined.

Hence, let us examine the updating sequence during a time-step that leads to the computation of the H_z component. Notice that for this field mode, $(\nabla \times \nabla\times)_z$ reduces to ∇^2_{xy}, since it has been assumed that there is no variation along the z-direction. In order to get a better insight into the above scenario, consider the graphical representation in Fig. 3.1. The FDTD formalism dictates that the value of $H_z\left(i+\frac{1}{2}, j+\frac{1}{2}\right)$ at the $(n+1)$-th time-step is obtained as a sequence of two curl operations, performed on magnetic and electric fields, respectively. Reffering to Fig. 3.1 and going backwards in time, we see that $H_z\left(i+\frac{1}{2}, j+\frac{1}{2}\right)$ is computed as a weighted sum of four curling electric field components. This is because conventional FDTD approximates the curl operator component $(\nabla \times \mathbf{E})_z$ through a four point discretization. In the same fashion, these electric

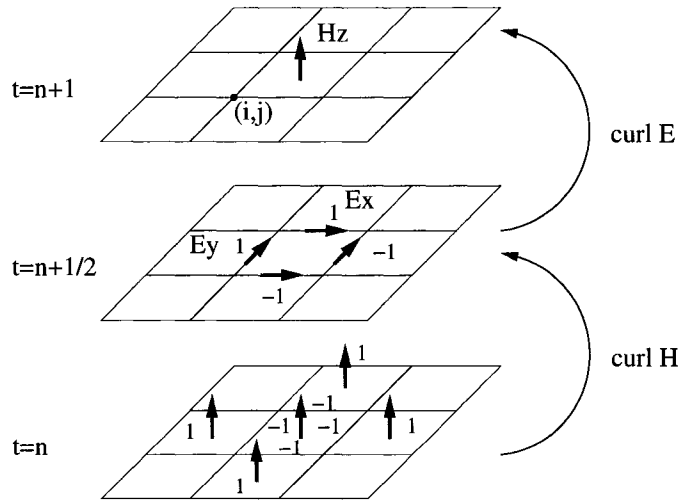

Fig. 3.1: Curl-curl approximation in the Yee scheme.

field components are computed by two curling magnetic field components (not four since it has been assumed no variation along the z-direction) at time-step n, with the one located at the center contributing four times in total. Therefore, we can see that the variation of $H_z\left(i+\frac{1}{2}, j+\frac{1}{2}\right)$ within a time-step is determined by its spatial variation represented by a 2-D Laplacian, transverse to its direction (z), where the Laplacian is approximated as:

$$\nabla^2_{xy} H_z\left(i+\frac{1}{2}, j+\frac{1}{2}\right) \sim -4 H_z\left(i+\frac{1}{2}, j+\frac{1}{2}\right) + H_z\left(i+\frac{3}{2}, j+\frac{1}{2}\right) + \\ + H_z\left(i-\frac{1}{2}, j+\frac{1}{2}\right) + H_z\left(i+\frac{1}{2}, j+\frac{3}{2}\right) + H_z\left(i+\frac{1}{2}, j-\frac{1}{2}\right) \tag{3.10}$$

Accordingly, it can be concluded that the four-point curl discretization performed by the Yee scheme results in the strongly anisotropic five-point Laplacian approximation given by:

$$\nabla^2 u_{i,j} = \frac{1}{h^2}\left[-4u_{i,j} + (u_{i+1,j} + u_{i-1,j} + u_{i,j+1} + u_{i,j-1})\right] - \\ - \frac{h^2}{12}\left(\partial_x^4 + \partial_y^4\right) u_{i,j} + \mathcal{O}\left(h^4\right) \tag{3.11}$$

where h is the spatial increment. The strong anisotropy of (3.11) is due to its leading error term (LET); it exhibits dispersion properties dependent on the propagation angle and consequently introduces anisotropically dispersion error into the computational domain. Given the above, it is

$$\nabla^2 u_{i,j} = \frac{1}{6\,h^2}\Big[-20\,u_{i,j} + \\ + 4\,(u_{i+1,j} + u_{i-1,j} + u_{i,j+1} + u_{i,j-1}) + \\ + (u_{i+1,j+1} + u_{i+1,j-1} + u_{i-1,j-1} + u_{i-1,j+1})\Big] - \\ - \frac{h^2}{12}\nabla^4 u_{i,j} + \mathcal{O}\left(h^4\right) \tag{3.13}$$

intuitively expected that superior FDTD accuracy could be achieved if a more accurate Laplacian representation was employed. In what follows, first a more accurate version of the discrete Laplacian is presented. Afterwards, it is demonstrated how the update equations should be modified, so that the more accurate Laplacian representation is utilized.

3.3. Formulation

The approximation in (3.11) is a member of the family of 9-point Laplacian approximations whose general form is given by [30], [31]:

$$\nabla^2 u_{ij} \approx c_0\,u_{i,j} + \\ + c_1\,(u_{i+1,j} + u_{i-1,j} + u_{i,j+1} + u_{i,j-1}) + \\ + c_2\,(u_{i+1,j+1} + u_{i+1,j-1} + u_{i-1,j-1} + u_{i-1,j+1}) \tag{3.12}$$

where c_0, c_1 and c_2 are arbitrary real numbers. It is easy to verify that the highest accuracy that can be achieved from (3.12) is second order. However by judiciously choosing c_0, c_1 and c_2 one can obtain the Laplacian approximation shown in (3.13). In particular the derivation of the above requires us to first perform a 2-D Taylor expansion on (3.12). Then c_0, c_1 and c_2 are subjected to appropriately chosen conditions so that second order of accuracy is obtained, and the corresponding LET turns out to be the biharmonic operator. The latter is highly desirable since it exhibits isotropic dispersion properties.

For the 9-point Laplacians' family, the combination of c_0, c_1 and c_2 that yields the biharmonic operator is unique. Moreover, the latter is the highest degree of isotropy that can be achieved. If a higher degree of isotropy is required then widened Laplacian stencils must be employed. This will be further elaborated later in this dissertation.

Let us now determine how to modify the update equations so that the 9-point Laplacian of (3.13) is indirectly computed. Recall that the ultimate objective is to modify the update equations so that the value of any H_z component at any time-step is determined by nine appropriately weighted H_z components from the previous time-step. First the update equations' stencil needs to be chosen so that a 9-point Laplacian stencil is retrieved. There are two ways to achieve the above and these are depicted in Figs. 3.2(a) and 3.2(b).

The first approach [Fig. 3.2(a)] is to retain a 4-point discretization, like the Yee-scheme suggests, for the curl operation that results to an H_z component update. However, for the update of E_x and E_y a *flux averaging* strategy is required in order to "reach out" for the diagonally located H_z-s. With respect to Fig. 3.2(a) it can be seen that the E_y component depicted by the thick arrow is updated not only by the immediately neighboring H_z components, but also by the ones defining the flux in the upper and lower cells, with respect to the updated component's vector direction (also shown thick).

The second approach is shown in Fig. 3.2(b). In this case a complementary strategy is adopted: for the updating of both the E_x and E_y components only the immediately neighboring H_z-s are used, similar to what the Yee scheme suggests. However, we modify the curl approximation that lies on the same plane on which the Laplacian is defined (for this problem the $x - y$ plane). This modification suggests that the curl operator that results in an H_z component update be longitudinally extended. Essentially this is a longitudinal extension of the curl related derivatives, with respect to the direction of the derived component, and it will be referred to as the *extended-curl* operator.

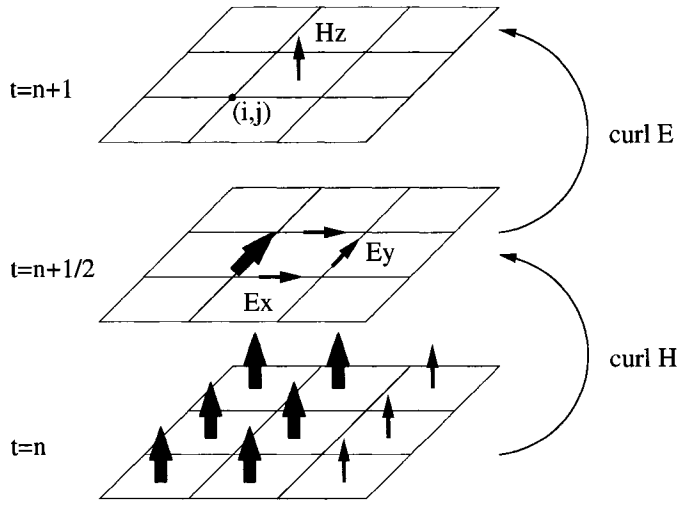

(a) Flux averaging approach.

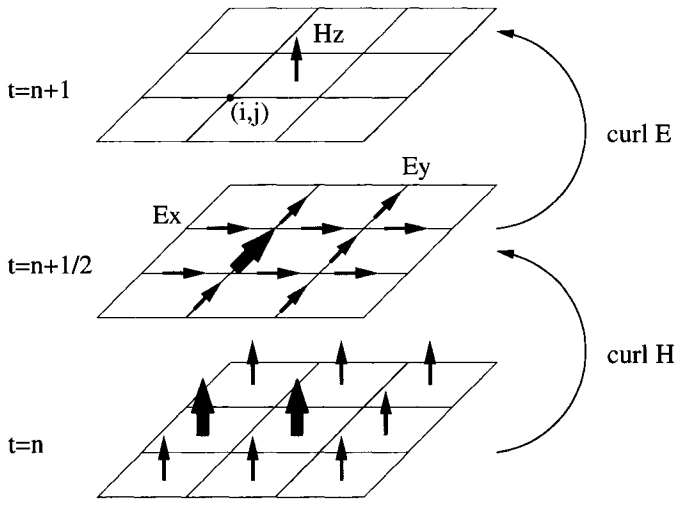

(b) Extended-curl approach.

Fig. 3.2: Update equations' modification for a 9-point Laplacian representation. The thick arrows indicate curl-related components between the first half time-step.

The choice between the two approaches is made based upon their ability to provide physically meaningful results. First of all, one notices that for this TE_Z field configuration the magnetic Gauss' law is exactly satisfied since:

$$\partial_t \nabla \cdot (\mu \mathbf{H}) = \partial_t (\partial_x, \partial_y, 0) \cdot (0, 0, \mu H_z) = 0 \tag{3.14}$$

The above suggests that no matter how the H_z update equation is modified in this 2-D space, magnetic flux conservation is always satisfied. In contrast, the modification of the electric field components update equations is more restricted since it is not always guaranteed that electric flux is preserved. Hence it becomes apparent that retaining the Yee algorithm update equations for E_x and E_y, is a very convenient and accurate "tactic" since the electric flux conservation is automatically satisfied [2], i.e.:

$$\delta_t \left(\delta_x D_x \Big|_{i,j}^{n} + \delta_y D_y \Big|_{i,j}^{n} \right) = 0 \tag{3.15}$$

which is the discretised version of the electric Gauss' Law, i.e.:

$$\partial_t \nabla \cdot (\varepsilon \mathbf{E}) = 0 \tag{3.16}$$

Bearing this in mind, it is obvious that the flux-averaging approach does not comply with the above scenario. In particular, electric flux is not conserved and consequently its implementation will provide solutions infested by spurious solutions. In contrast, the extended-curl approach is in absolute agreement with both of the Gauss' Laws. Accordingly, this approach is followed for the development of our scheme.

To complete the determination of the extended-curl operator its weights need to be specified.

From the previous discussion the updating equation for H_z is given by:

$$\begin{aligned}\delta_t H_z\Big|^{n+1}_{i+\frac{1}{2},j+\frac{1}{2}} = \frac{1}{\mu}\Bigg[&\beta\left(\delta_y E_x\Big|^{n+1}_{i+\frac{3}{2},j+\frac{1}{2}} - \delta_x E_y\Big|^{n+1}_{i+\frac{1}{2},j+\frac{3}{2}}\right)\\ &+\alpha\left(\delta_y E_x\Big|^{n+1}_{i+\frac{1}{2},j+\frac{1}{2}} - \delta_x E_y\Big|^{n+1}_{i+\frac{1}{2},j+\frac{1}{2}}\right)\\ &+\beta\left(\delta_y E_x\Big|^{n+1}_{i-\frac{1}{2},j+\frac{1}{2}} - \delta_x E_y\Big|^{n+1}_{i+\frac{1}{2},j-\frac{1}{2}}\right)\Bigg]\end{aligned} \tag{3.17}$$

where α and β are arbitrary real numbers. Recall that for E_x and E_y, we resort to the standard update equations, that is (3.7) and (3.8). Now, if we apply the sequence of these update equations for a time-step cycle as depicted in Fig. 3.2(b), then the resulting Laplacian approximation of any H_z component is given by:

$$\begin{aligned}\nabla^2 u_{ij} \approx \frac{1}{h^2}\Big[&-4\alpha u_{i,j} +\\ &+(\alpha-2\beta)\left(u_{i+1,j}+u_{i-1,j}+u_{i,j+1}+u_{i,j-1}\right)+\\ &+2\beta\left(u_{i+1,j+1}+u_{i+1,j-1}+u_{i-1,j-1}+u_{i+1,j-1}\right)\Big]\end{aligned} \tag{3.18}$$

where $u_{ij} \equiv H_z(i+\frac{1}{2}, j+\frac{1}{2})$. The values of α and β for any desired Laplacian approximation are given by equating like terms in (3.18) and (3.12). For instance (3.13) corresponds to the following extended-curl weights:

$$\left.\begin{aligned} -4\alpha &= -20/6\\ 2\beta &= 1/6\\ a-2\beta &= 4/6\end{aligned}\right\} \Rightarrow \begin{aligned} \alpha &= 5/6\\ \beta &= 1/12\\ \alpha-2\beta &= 4/6\end{aligned}$$

where obviously the third equation is satisfied by the calculated values for α and β.

To sum up, in this section a methodology was presented which via the utilization of an extended-curl operator, allows us to map any 9-point Laplacian into FDTD update equations. The reason that our analysis is developed based on the approximation shown in (3.13) is that the latter is the most prominent 9-point Laplacian. However the same conclusions would have been drawn

$$\mathbf{G} = \begin{bmatrix} 1 & 0 & -2\,\mathrm{j}\,\xi_y\,S_y \\ 0 & 1 & 2\,\mathrm{j}\,\xi_x\,S_x \\ -2\,\mathrm{j}\,\zeta_y\,S_y & 2\,\mathrm{j}\,\zeta_x\,S_x & 1 - 4\,\xi_y\,\zeta_y\,S_y^2\,C_x - 4\,\xi_x\,\zeta_x\,S_x^2\,C_y \end{bmatrix} \tag{3.21}$$

if the analysis was carried out with respect to any other 9-point representation. In what follows the new family of schemes are further examined by studying their stability as well their dispersion properties.

3.4. Stability and dispersion analysis

Let us consider first the scheme that corresponds to (3.13), that is the extended-curl operator weighted with $\alpha = 5/6$ and $\beta = 1/12$. In order to investigate the proposed scheme's stability, a 2-D unbounded, linear and homogeneous space is assumed. The time-step bound that ensures stability can be obtained by employing a standard von Neumann analysis. This requires that spatial discrete Fourier modes of the form:

$$u_{i,j}^n = \hat{u}^n \left(\tilde{k}_x, \tilde{k}_y\right) \mathrm{e}^{-\mathrm{j}\left(\tilde{k}_x\, i\,\Delta x + \tilde{k}_y\, j\,\Delta y\right)} \tag{3.19}$$

are substituted into the update equations (3.7), (3.8) and (3.17). $\tilde{k}$ denotes the discrete wavenumber which, for an ideal FDTD algorithm, should be equal to the physical wavenumber, $k = \omega/c$. The resulting equations can be cast into the following matrix form:

$$\hat{\mathbf{u}}^{n+1} = \mathbf{G}\,\hat{\mathbf{u}}^n \tag{3.20}$$

where $\hat{\mathbf{u}}^n = \left[\hat{E}_x^n \;\; \hat{E}_y^n \;\; \hat{H}_z^{n+\frac{1}{2}}\right]^T$ is the field component vector, $\mathbf{G}$ is the amplification matrix given in (3.21). Also,

$$\xi_w = \frac{\Delta t}{\varepsilon\,\Delta w}, \qquad \zeta_w = \frac{\Delta t}{\mu\,\Delta w} \tag{3.22}$$

and

$$S_w = \sin\left(\tilde{k}_w \Delta w/2\right), \qquad C_w = \alpha + 2\,\beta\,\cos\left(\tilde{k}_w \Delta w\right) \tag{3.23}$$

with $w \in \{x, y\}$. The eigenvalues of the amplification matrix are the following:

$$\lambda_1 = 1, \quad \lambda_{2,3} = 1 - 2\Psi \pm 2\sqrt{-\Psi + \Psi^2} \tag{3.24}$$

where $\Psi = \xi_x \zeta_x S_x^2 C_y + \xi_y \zeta_y S_y^2 C_x$. The scheme is stable if all eigenvalues lie within the unit circle. This condition is satisfied when the time-step is subjected to the following constraint:

$$\Delta t \leq \left(c \sqrt{\frac{S_x^2 C_y}{\Delta x^2} + \frac{S_y^2 C_x}{\Delta y^2}} \right)^{-1} \tag{3.25}$$

where $c = 1/\sqrt{\varepsilon \mu}$ is the speed of light in the material being modeled. The CFL condition is obtained if in the above inequality we set $\Delta x = \Delta y = h$, and substitute the maximum value of $S_x^2 C_y$ and $S_y^2 C_x$. Thus:

$$\Delta t \leq \frac{1}{\sqrt{2\,(\alpha - 2\beta)}} \frac{h}{c} = \frac{\sqrt{3}}{2} \frac{h}{c} \tag{3.26}$$

where we recall that $\alpha = 5/6$ and $\beta = 1/12$ for our scheme. Notice that if we had chosen $(\alpha, \beta) \equiv (1, 0)$ we would recover the standard FDTD curl, and (3.26) would yield the Courant limit of the conventional 2-D FDTD scheme, i.e. $S = \sqrt{2}/2$.

The dispersion relation can be derived if we assume discrete temporal Fourier modes in (3.19), in addition to the spatial ones, or: $\widehat{u}^n = \widehat{u}^0 \, \mathrm{e}^{\mathrm{j}\omega n \Delta t}$. Hence (3.20) yields the following eigenvalue problem:

$$\begin{bmatrix} S_t & 0 & -\xi_y S_y \\ 0 & S_t & \xi_x S_x \\ -\zeta_y S_y C_x & \zeta_x S_x C_y & S_t \end{bmatrix} \begin{bmatrix} \widehat{E}_x^0 \\ \widehat{E}_y^0 \\ \widehat{H}_z^0 \end{bmatrix} = \mathbf{0} \tag{3.27}$$

where $S_t = \sin(\omega \Delta t/2)$. For non-trivial solutions of (3.27), the determinant of the system matrix must be zero. Hence, after some straightforward manipulations, the dispersion relation for the

scheme is found to be:

$$\left[\frac{1}{c\Delta t}\sin\left(\frac{\omega\Delta t}{2}\right)\right]^2 = \left[\frac{1}{\Delta x}\sin\left(\frac{\tilde{k}_x\Delta x}{2}\right)\right]^2\left[\alpha + 2\beta\cos\left(\tilde{k}_y\Delta y\right)\right] + \left[\frac{1}{\Delta y}\sin\left(\frac{\tilde{k}_y\Delta y}{2}\right)\right]^2\left[\alpha + 2\beta\cos\left(\tilde{k}_x\Delta x\right)\right] \tag{3.28}$$

If we Taylor expand (3.28) with respect to both the temporal and spatial variables, the scheme's accuracy can be obtained. Hence we have:

$$\left(\frac{\omega}{c}\right)^2 + \mathcal{O}\left(\Delta t^2\right) = \tilde{k}_x^2 + \tilde{k}_y^2 - \\ - \frac{1}{12}\left[\Delta x^2\tilde{k}_x^4 + \Delta y^2\tilde{k}_y^4 + \left(\Delta x^2 + \Delta y^2\right)\tilde{k}_x^2\tilde{k}_y^2\right] + \\ + \mathcal{O}\left(\Delta x^4\right) + \mathcal{O}\left(\Delta y^4\right) \tag{3.29}$$

Obviously the scheme is second order accurate both in space and time. However, if we write the wavevector in polar form as $(\tilde{k}_x, \tilde{k}_y) = \tilde{k}(\cos\phi, \sin\phi)$ and further assume a uniform discretization, then the spatial LET in (3.29) yields:

$$\text{LET} = h^2\left(\tilde{k}_x^4 + \tilde{k}_y^4 + 2\tilde{k}_x^2\tilde{k}_y^2\right) = h^2\left(\tilde{k}_x^2 + \tilde{k}_y^2\right)^2 = h^2\tilde{k}^4$$

Evidently, the LET in (3.29) is independent of the propagation angle, meaning that the scheme may be second order accurate but it is fourth order isotropic. For comparison purposes, the approximation to the constraint equation obtained by the Yee-scheme is given by (3.28) if we set $\alpha = 1,\ \beta = 0$ and then Taylor expand. One gets:

$$\left(\frac{\omega}{c}\right)^2 + \mathcal{O}\left(\Delta t^2\right) = \tilde{k}_x^2 + \tilde{k}_y^2 - \\ - \frac{1}{12}\left(\Delta x^2\tilde{k}_x^4 + \Delta y^2\tilde{k}_y^4\right) + \mathcal{O}\left(\Delta x^4\right) + \mathcal{O}\left(\Delta y^4\right) \tag{3.30}$$

where in this case, the spatial LET strongly depends on the direction of propagation as:

$$\text{LET} = h^2\left(\tilde{k}_x^4 + \tilde{k}_y^4\right) = h^2\tilde{k}^4\left(\cos^4\phi + \sin^4\phi\right)$$

Also, in the limit of a very fine discretization ($\Delta x \to 0, \Delta y \to 0$), (3.29) reduces to the constraint equation that governs the propagation of a monochromatic wave in a general 2-D medium. At

this point it should be mentioned that the same order of isotropy as the one demonstrated in (3.29), can be achieved by FDTD implementations on hexagonal grids as has been demonstrated in Liu in [10] and Xiao in [11]. However, the distinct feature of the proposed algorithm is that it retains the simplicity of the Yee-scheme. Thus it is relatively painless to implement existing techniques designed for the Yee-scheme such as absorbing boundary conditions, whereas on a hexagonal grid this is not a trivial task.

3.5. Extended-curl realizations for a higher Courant number

The preceding analysis revealed that the extended-curl scheme corresponding to the isotropic 9-point Laplacian is characterized by a more relaxed Courant limit, approximately 1.2 times higher than that of the Yee scheme. In what follows the highest achievable Courant number is investigated, assuming α and β are arbitrary real numbers. More precisely, we are looking for 9-point Laplacian approximations that result in extended-curl schemes with Courant number higher than $S = \sqrt{3}/2$. For reasons that will become clear later in our discussion, let us first examine if a unity Courant number can be achieved. $S = 1$ implies that:

$$\Delta t \leq \frac{h}{c} \leq \frac{1}{\max\limits_{(\alpha,\beta)} \left\{ \sqrt{S_x^2 C_y + S_y^2 C_x} \right\}} \frac{h}{c} \tag{3.31}$$

which leads to the constraint:

$$\max_{(\alpha,\beta)} \left\{ \sqrt{S_x^2 C_y + S_y^2 C_x} \right\} \leq 1 \tag{3.32}$$

Now, if we Taylor expand (3.28) we get:

$$\left(\frac{\omega}{c}\right)^2 + \mathcal{O}\left(\Delta t^2\right) = (\alpha + 2\beta)\left(\tilde{k}_x^2 + \tilde{k}_y^2\right) + \mathcal{O}\left(\Delta x^2\right) + \mathcal{O}\left(\Delta y^2\right) \tag{3.33}$$

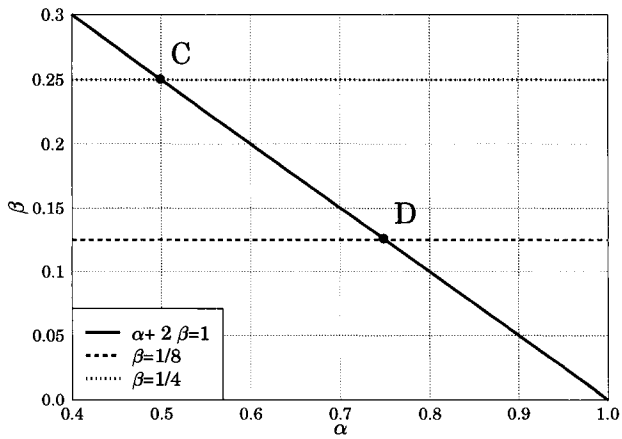

Fig. 3.3: Determination of parameters α and β.

The above relation in the limit of a vanishing cell size, should reduce to the constraint equation of a continuous medium, therefore the following condition should hold:

$$\alpha + 2\beta = 1 \tag{3.34}$$

Given this condition, it is straightforward to show that [Section 3.9]:

$$\max_{(\alpha,\beta)} \left\{ S_x^2 C_y + S_y^2 C_x \right\} = \max_{\beta} \{1, 2 - 8\beta\} \tag{3.35}$$

If we substitute the above into (3.32) and additionally assume that the square rooted quantity must be positive, we get the following constraint:

$$1/8 \leq \beta \leq 1/4 \tag{3.36}$$

The system of (3.34) and (3.36) can be solved graphically as shown in Fig. 3.3. The solution pairs lie along the solid line section CD, bounded by the dotted and dashed lines which means that for this continuum of α and β values, a Courant number $S = 1$ can be achieved. We refer to this group of extended-curl realizations as the "unity Courant number" schemes. As demonstrated later, there exists an optimum (α, β) pair, and determined by the scheme's dispersion properties as well as the scheme's ability to provide realistic results.

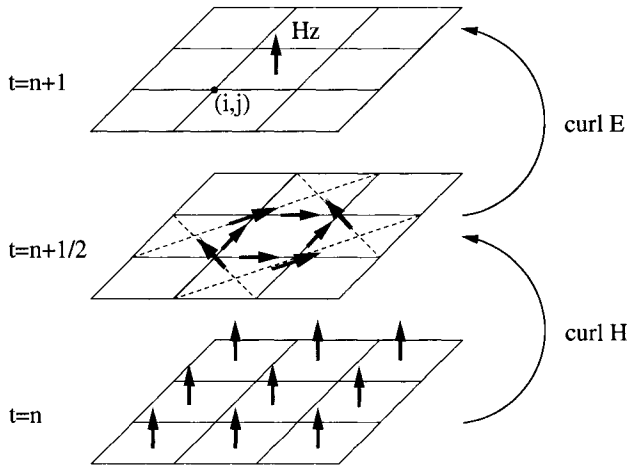

Fig. 3.4: Alternative extended-curl realization.

Before proceeding to the next Section some remarks should be made. First, regarding the generalization of the results presented thus far, we observe that (3.28) is the numerical dispersion relation that characterizes all members of the extended-curl family including the "unity Courant number" schemes. Similarly, the general time-step bound valid for all extended-curl realizations is the following:

$$\Delta t \leq \frac{1}{\sqrt{\max_{\beta}\{1, 2 - 8\beta\}}} \frac{h}{c} \tag{3.37}$$

For instance, if $\beta = 0$ the CFL condition for the Yee-scheme is obtained. The above expression reveals that the extended-curl family of schemes cannot support Courant numbers that exceed unity. Clearly, for a Courant number higher than one, the condition $\max_{\beta}\{1, 2 - 8\beta\} < 1$ should hold, which obviously is impossible.

The last remark can be also justified from the following reasoning. An alternative, although absolutely equivalent, way to interpret the extended curl schemes is as a combination of two Yee schemes. As illustrated in Fig. 3.4 the first one operates on a standard Cartesian grid comprised of square cells with size h. The second one exists on a $\pi/4$-rotated Cartesian grid, that consists of rhombic-cells with size $h\sqrt{2}$. The two grids are positioned so that each square cell of the Cartesian

grid is inscribed into a rhombic cell. A rigorous justification of the above is provided by the fact that an alternative representation of (3.18) is given by [31]:

$$\begin{aligned}
&\nabla^2 u_{i,j} \approx \\
&\approx \frac{\alpha - 2\beta}{h}\left[\left(\frac{u_{i+1,j} - u_{i,j}}{h} - \frac{u_{i,j} - u_{i-1,j}}{h}\right) + \left(\frac{u_{i,j+1} - u_{i,j}}{h} - \frac{u_{i,j} - u_{i,j-1}}{h}\right)\right] + \\
&+ \frac{2\beta}{h\sqrt{2}}\left[\left(\frac{u_{i+1,j+1} - u_{i,j}}{h\sqrt{2}} - \frac{u_{i,j} - u_{i-1,j-1}}{h\sqrt{2}}\right) + \left(\frac{u_{i-1,j+1} - u_{i,j}}{h\sqrt{2}} - \frac{u_{i,j} - u_{i+1,j-1}}{h\sqrt{2}}\right)\right]
\end{aligned} \tag{3.38}$$

If we correspond $u_{i,j}$ to $H_z(i+\frac{1}{2}, j+\frac{1}{2})$ then the terms in the first pair of square-brackets represent four discrete curl-operations which result in four electric field components that lie on the $x-y$ plane, in a closed-loop, circulating formation. These curl operations are performed on a Cartesian grid with cell size h, as indicated by the denominators of the corresponding terms. Regarding to the terms in the second pair of square brackets we can conclude that they are a $\pi/4$-rotated version of the first ones from their corresponding finite difference stencil. In addition their denominators reveal that the cell size is $h\sqrt{2}$. Consequently, given that the maximum time-step for the Yee-scheme, on a uniform grid is $\Delta t = \frac{h}{c\sqrt{2}}$, then the same time-step for a cell size of $h\sqrt{2}$ becomes $\Delta t = \frac{h}{c}$, which for a uniform Cartesian grid corresponds to a unity Courant number.

3.6. Anisotropy and dispersion error

In this section the phase velocity isotropy as well the dispersion error of the most representative extended-curl schemes are examined. These are the Yee-scheme, the most isotropic Laplacian scheme, and two of the unity-Courant-number schemes, corresponding to points D and C of Fig. 3.3. Their properties are summarized in Table 3.1. In order to examine the numerical phase velocity behavior versus propagation angle, it is required to substitute $\left(\tilde{k}_x, \tilde{k}_y\right) = \tilde{k}\,(\cos\phi, \sin\phi)$ in (3.28),

Table 3.1: Comparison of the most representative extended-curl realizations.

Case	(α, β)	S	(c_0, c_1, c_2)	LET
1 (Yee scheme)	$(1, 0)$	$\frac{\sqrt{2}}{2}$	$(-4, 1, 0)$	$\nabla^4 - 2\,\partial_{xy}^4$
2 (The most isotropic Laplacian)	$(\frac{5}{6}, \frac{1}{12})$	$\frac{\sqrt{3}}{2}$	$(-\frac{10}{3}, \frac{2}{3}, \frac{1}{6})$	∇^4
3 (Point D in Fig. 3.3)	$(\frac{3}{4}, \frac{1}{8})$	1	$(-3, \frac{1}{2}, \frac{1}{4})$	$\nabla^4 + \partial_{xy}^4$
4 (Point C in Fig. 3.3)	$(\frac{1}{2}, \frac{1}{4})$	1	$(-2, 0, \frac{1}{2})$	$\nabla^4 + 4\,\partial_{xy}^4$

and then to solve iteratively the resulting transcendental equation with respect to the numerical wavenumber $\tilde{k}$. Finally, the numerical phase velocity can be computed as: $\tilde{v}_p = \omega/\tilde{k}$.

The corresponding results for a discretization of $\lambda/10$, and using the Courant stability limit are depicted in Fig. 3.5. There is a one-to-one correspondence between the form of the LET shown in the last column of Table 3.1 and the schemes' isotropy performance. More precisely the bigger the number of cross-terms ∂_{xy}^4 by which the LET deviates from the biharmonic operator, the worse the isotropy becomes. The dashed line (Case 2) exhibits highly isotropic phase velocity characteristics corresponding to the most isotropic Laplacian approximation. In the inset figure, there is a more detailed illustration of the phase velocity behavior for this case. It does fluctuate as a function of the propagation angle, however the amplitude of this ripple is of the order of 10^{-4}. Furthermore, the dash-dotted-square-marker line (Case 3) is more isotropic compared to the conventional FDTD scheme of Case 1, but less isotropic than Case 2. Nevertheless, this scheme has the distinguishing characteristic that for propagation along the principal axes ($\phi = 0°, 90°$) the "magic time-step" condition [2, 32] is satisfied, meaning that $\Delta t = h/c$ and the dispersion error is totally eliminated for all frequencies. It is interesting to note that the schemes that correspond to Cases 1 and 3 exhibit complementary anisotropy characteristics, with Case 3 being overall more isotropic. Finally, Case 4 exhibits the most anisotropic phase velocity, and in particular, the value of the phase velocity minimum at $\phi = 45°$ has been significantly decreased, compare to Case 3. Not only does this

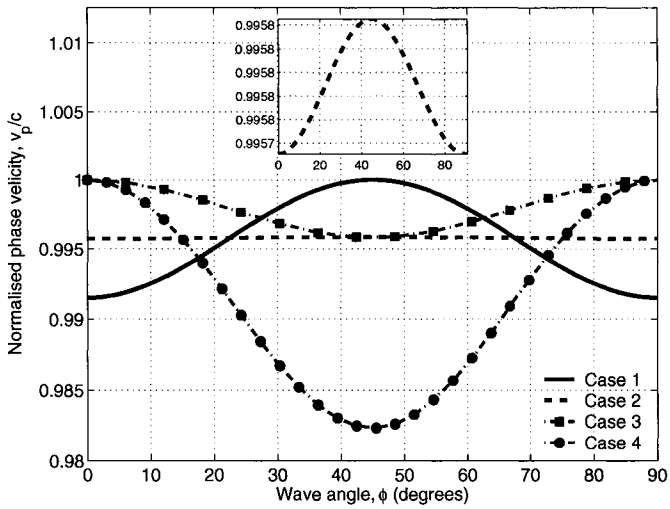

Fig. 3.5: Normalized phase velocity.

severely deteriorate the scheme's isotropy but it also has a detrimental effect on the dispersion error as shown next.

A practical measure of the scheme's performance with respect to the dispersion error reduction is the maximum absolute phase error per wavelength, defined as:

$$\psi = 360^\circ \max_{\phi} \left\{ \left| 1 - \frac{\tilde{v}_p}{c} \right| \right\} \tag{3.39}$$

In Fig. 3.6 the dispersion error for the four cases is illustrated as a function of the number of cells per wavelength ($N_\lambda = h/\lambda$). Clearly all schemes are second order accurate since the slope of each one is -2. Moreover, Cases 2 and 3 suffer less from dispersion errors than conventional FDTD. In contrast Case 4 as expected from the previous analysis exhibits the worst dispersion characteristics. At this point it can be asserted that Cases 3 and 4 correspond to the best and worst "unity Courant number" schemes, respectively. All other combinations of (α, β) pairs exhibit isotropy and dispersion characteristics within the performance bounds defined by Cases 3 and 4.

In Fig. 3.7 the anisotropy error for each case is plotted as a function of resolution N_λ. We have chosen to define the anisotropy error as the difference between the maximum and minimum

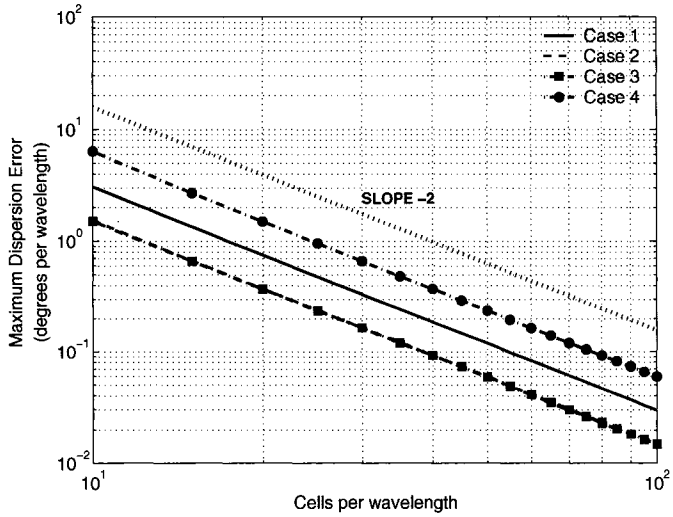

Fig. 3.6: Maximum dispersion error.

value of $\tilde{v}_p$, relative to the speed of light c. It can be seen that as (3.29) predicts, the Case 2 scheme exhibits fourth order anisotropy error, in contrast to the other three schemes, which are second order isotropic.

Now, let us further examine the behavior of the "unity Courant number" schemes for different values of the (α, β) pair, that lie on the CD section of Fig. 3.3. The analysis in the last paragraph of the previous section revealed that an equivalent expression for the update equation of $H_z(i+\frac{1}{2}, j+\frac{1}{2})$ is given in the following form:

$$\delta_t H_z\Big|_{i+\frac{1}{2},j+\frac{1}{2}}^{n+1} = \frac{1}{\mu}\Big[(\alpha - 2\beta)(\nabla \times \mathbf{E})_z^{Yee} + 4\beta(\nabla \times \mathbf{E})_z^{rot-Yee}\Big]_{i+\frac{1}{2},j+\frac{1}{2}}^{n+1} \tag{3.40}$$

Apparently, this is a linear combination of two flux terms: one defined on a regular FDTD grid, and a second one defined on a $\pi/4$-rotated version. These are denoted as $(\nabla \times \mathbf{E})_z^{Yee}$ and $(\nabla \times \mathbf{E})_z^{rot-Yee}$ respectively. Hence, at point D we have: $\alpha - 2\beta = 4\beta = \frac{1}{2}$. This condition indicates that the two flux terms in (3.40) contribute equally. However, as we move from D to C, or equivalently as $\alpha \rightarrow 2\beta$, the Yee flux term gradually vanishes, while the other term increases. In the limit, at point C, the flux is due entirely to the rhombic-cell grid arrangement. This scheme, based

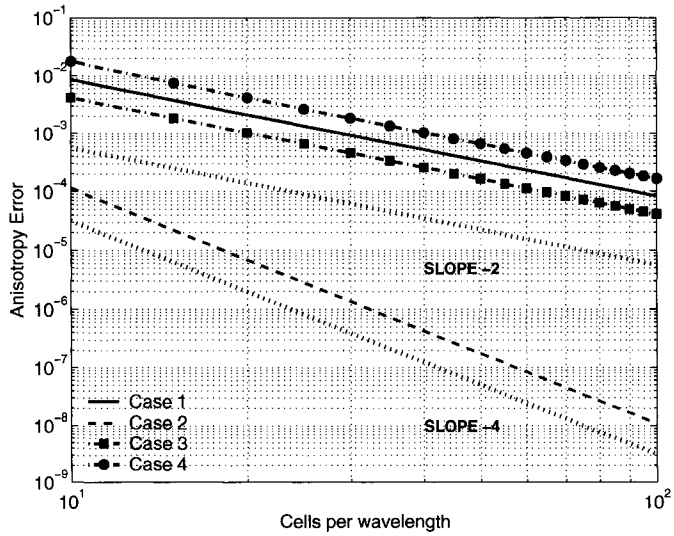

Fig. 3.7: Anisotropy error.

solely on a $\pi/4$-rotated square cell, has been shown to be equivalent to a finite-difference scheme developed on a staggered collocated grid [33,34]. The detrimental characteristic of the latter is that when excited by localized sources, it suffers from grid-decoupling [10,33]. Consequently, from the "unity Courant number" schemes, the choice of $(\alpha, \beta) \equiv (3/4, 1/8)$ is optimal, not only because it renders the most isotropic and the least dispersive scheme, but in addition because it prevents the development of the non-physical grid-decoupling effect.

3.7. Some remarks on the conservation properties of the extended curl scheme

Some interesting conclusions, regarding the scheme's charge conservation properties, can be drawn from the numerical dispersion matrix shown in (3.27). The following approach was initially implemented by Marcysiak and Gwarek in [35]. Hence, from the first two equations we have:

$$\left.\begin{aligned} S_t\,\widehat{E}_x^0 - \xi_y\,S_y\,\widehat{H}_z^0 &= 0 \\ S_t\,\widehat{E}_y^0 + \xi_x\,S_x\,\widehat{H}_z^0 &= 0 \end{aligned}\right\} \Rightarrow \begin{aligned} S_t\,\xi_x\,S_x\,\widehat{E}_x^0 - \xi_x\,\xi_y\,S_x\,S_y\,\widehat{H}_z^0 &= 0 \\ S_t\,\xi_y\,S_y\,\widehat{E}_y^0 + \xi_x\,\xi_x\,S_x\,S_y\,\widehat{H}_z^0 &= 0 \end{aligned} \tag{3.41}$$

Then if we add the above two equations, we get:

$$S_t \left(\xi_x \, S_x \, \widehat{E}_x^0 + \xi_y \, S_y \, \widehat{E}_y^0 \right) = 0 \tag{3.42}$$

or

$$\frac{1}{\Delta t} \sin\left(\frac{\omega \, \Delta t}{2}\right) \left[\frac{1}{\Delta x} \sin\left(\frac{\tilde{k}_x \Delta x}{2}\right) \varepsilon \, \widehat{E}_x^0 + \frac{1}{\Delta y} \sin\left(\frac{\tilde{k}_y \Delta y}{2}\right) \varepsilon \, \widehat{E}_y^0 \right] = 0 \tag{3.43}$$

Now, given the following Fourier pairs

$$\mathcal{F}\{\delta_x\} \rightarrow -\frac{2\,\mathrm{j}}{\Delta x} \sin\left(\frac{\tilde{k}_x \Delta x}{2}\right) \tag{3.44}$$

and

$$\mathcal{F}\{\delta_t\} \rightarrow \frac{2\,\mathrm{j}}{\Delta t} \sin\left(\frac{\omega \Delta t}{2}\right) \tag{3.45}$$

we can conclude that (3.43) is the spatio-temporal Fourier transform of (3.15). Consequently with the aid of the numerical dispersion matrix, we have verified the conservative nature of the scheme.

Let us now examine the conservation properties of the flux-averaging scheme using the previous approach. The numerical dispersion relation in matrix form for this scheme is given by:

$$\begin{bmatrix} S_t & 0 & -\xi_y \, S_y \, C_x \\ 0 & S_t & \xi_x \, S_x \, C_y \\ -\zeta_y \, S_y & \zeta_x \, S_x & S_t \end{bmatrix} \begin{bmatrix} \widehat{E}_x^0 \\ \widehat{E}_y^0 \\ \widehat{H}_z^0 \end{bmatrix} = \mathbf{0} \tag{3.46}$$

Again, by combining the first two equations we obtain:

$$\begin{aligned} &\frac{1}{\Delta t} \sin\left(\frac{\omega \, \Delta t}{2}\right) \left[\frac{1}{\Delta x} \sin\left(\frac{\tilde{k}_x \Delta x}{2}\right) \varepsilon \, \widehat{E}_x^0 + \frac{1}{\Delta y} \sin\left(\frac{\tilde{k}_y \Delta y}{2}\right) \varepsilon \, \widehat{E}_y^0 \right] = \\ &= \frac{2\,\beta}{\Delta x \, \Delta y} \sin\left(\frac{\tilde{k}_x \Delta x}{2}\right) \sin\left(\frac{\tilde{k}_y \Delta y}{2}\right) \left[\cos\left(\tilde{k}_x \Delta x\right) - \cos\left(\tilde{k}_y \Delta y\right) \right] \widehat{H}_z^0 \end{aligned} \tag{3.47}$$

Obviously, the flux averaging scheme is not conservative. From the right hand side of the above equation, we can see that the unbalanced charge is a function of both the frequency of operation as

well as the propagation angle. The behavior of the residual term is better revealed by examining its Taylor expansion when $\Delta x = \Delta y = h \rightarrow 0$. It is

$$\text{RHS} = \frac{\beta}{4} \tilde{k}_x \tilde{k}_y \left(-\tilde{k}_x^2 + \tilde{k}_y^2\right) h^2 + \mathcal{O}\left(h^4\right) \tag{3.48}$$

It can be seen that the excess charge is by no means negligible, and as a matter of fact it is on the order of the numerical error. This last result is an accurate quantitative measure of the artificial charge that the scheme generates, and it can be used as a criterion to determine whether the algorithm is appropriate for a given application.

3.8. Numerical Examples

3.8.1. Free space propagation

In this section preliminary numerical results are presented to support the previously discussed analysis. A 2-D domain 2 m $\times$ 2 m, that lies on the $x - y$ plane, is considered. The domain is uniformly discretized using a cell size of $\Delta x = 1$ cm. The computational domain consists of 200 $\times$ 200 cells, and a twelve-cell-thick uniaxial PML is placed around it. A TE_Z field configuration is excited by injecting a z-directed magnetic field at the center of the domain with a differentiated Gaussian pulse time dependence. We let the cylindrical waves propagate and probe the time history of H_z at two equidistant points, with respect to the excitation point, one along the principal axis ($\phi = 0°$) and one along the domain's diagonal ($\phi = 45°$). Simulations are performed for Cases 1 and 2 and the corresponding results are shown in Figs. 3.8(a)-3.8(b). As expected, Case 2 is significantly more isotropic and so the pulse distortion due to dispersion errors is less severe. Also in Figs. 3.9(a) and 3.9(b) there are contour plots of the propagating pulse for the two Cases.

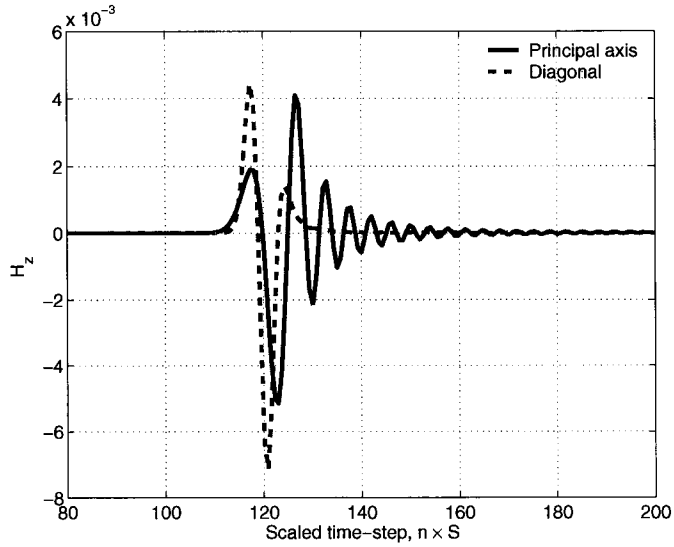

(a)

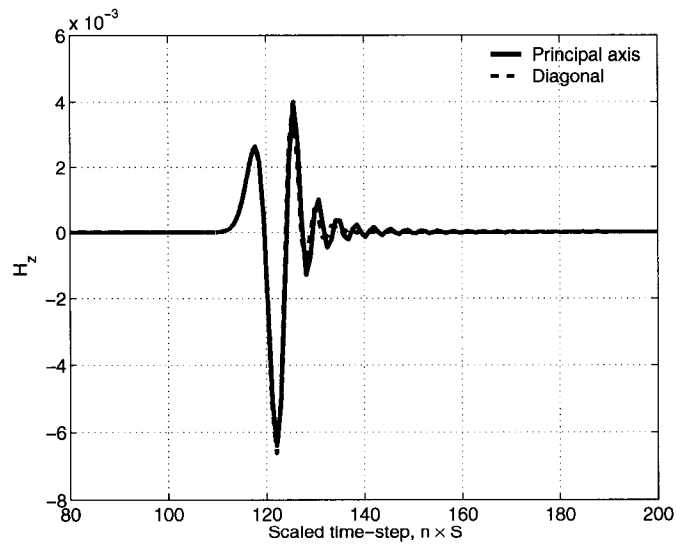

(b)

Fig. 3.8: Pulse propagation in a 2-D domain with TE_Z fields. (a) Case 1. (b) Case 2.

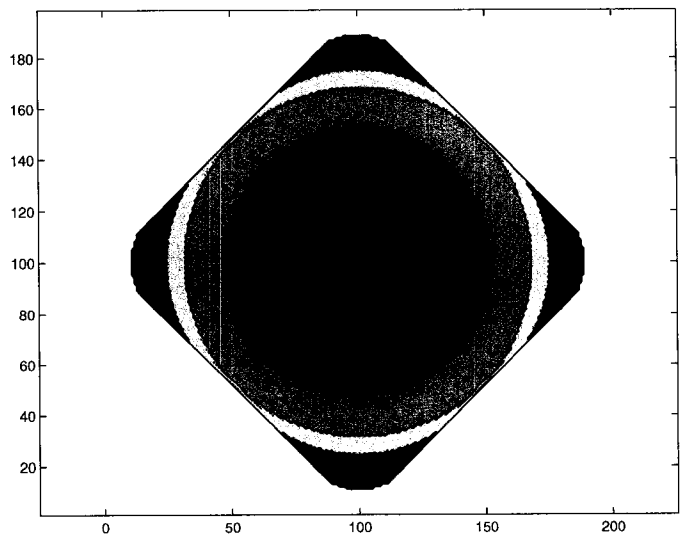

(a)

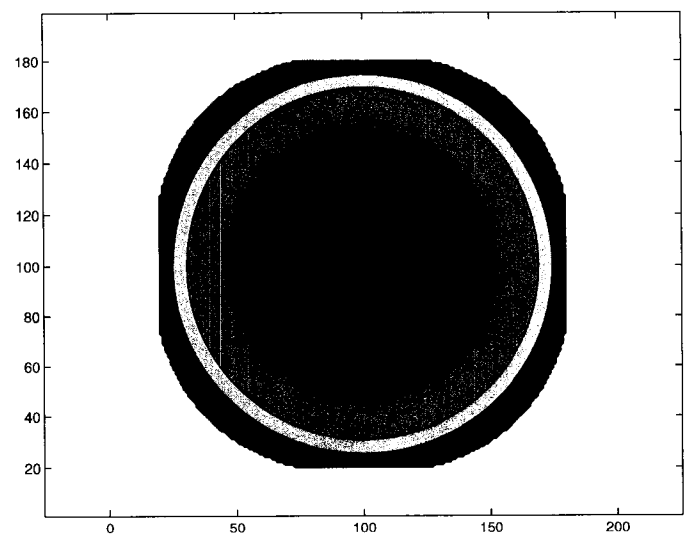

(b)

Fig. 3.9: Contour plots of pulse propagation in a 2-D domain with TE_Z fields. (a) Case 1. (b) Case 2.

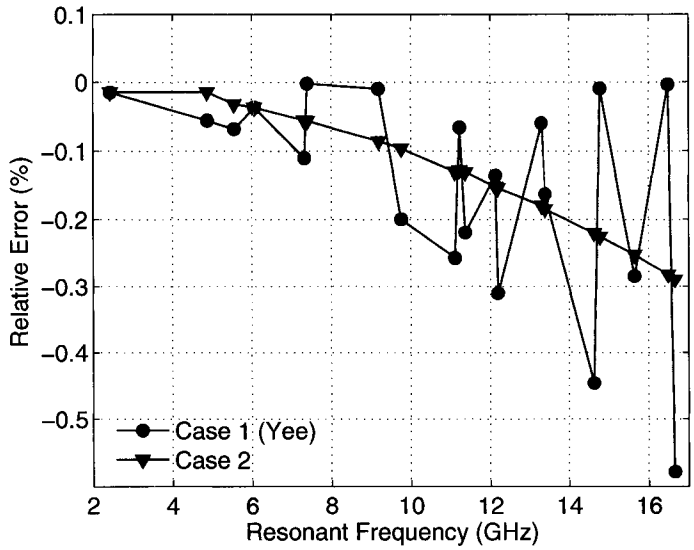

Fig. 3.10: Resonant frequency prediction error.

3.8.2. Cavity resonances

In this numerical experiment, we calculate the resonances of a rectangular cavity whose boundaries correspond to perfect electric conductors ($\hat{\mathbf{n}} \times \mathbf{E} = \mathbf{0}$). The dimensions of the cavity are 0.0615 m $\times$ 0.027 m, and it is uniformly discretized with a 41 $\times$ 18 grid. Simulations were performed using the Yee and the Case 2 schemes. In all simulations the maximum allowable time-step was used. The $\mathrm{TE_Z}$ mode is excited in the cavity by injecting a z-directed magnetic field at its center with a very sharp differentiated Gaussian pulse time dependence.

A sufficient amount of time-steps are executed so that a 1 MHz frequency resolution is achieved. Where applicable, image theory is applied for the boundary treatment. In Fig. 3.10 the algebraic relative error is illustrated for the first 20 resonant frequencies as computed by the two schemes against the corresponding analytic values. It is observed that both schemes underestimate the resonances' values, with the Case 2 scheme being less dispersive as expected. Also, the detrimental effects of anisotropy can be observed in the Yee scheme predictions, where accuracy depends

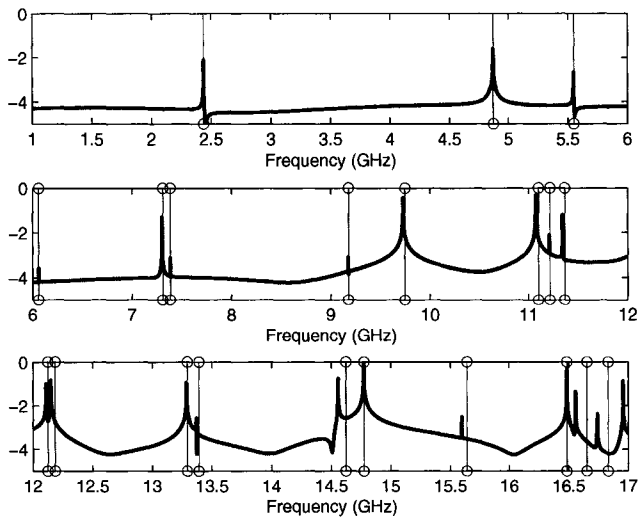

(a)

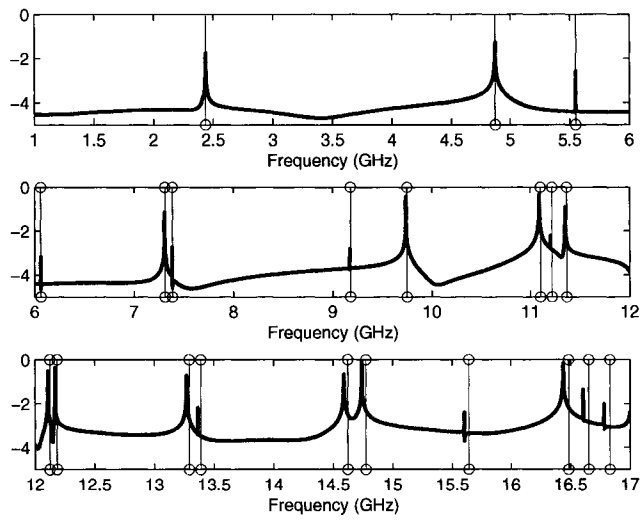

(b)

Fig. 3.11: 2-D cavity resonances. (a) Case 1 (Yee). (b) Case 2.

Table 3.2: L_2 error comparisons for radiation pattern predictions.

	Yee	Case 2
$d = 2.5\,\lambda$	0.1011	0.0528
$d = 5.5\,\lambda$	0.1513	0.0873

on propagation directions, and thus is bounded according to the highest and lowest achievable phase velocity in the grid.

3.8.3. Radiation pattern

In this subsection we calculate the radiation pattern of two infinite line sources. The sources extend to infinity along the z-axis, they are located symmetrically with respect to the origin along the y-axis, and they are uniformly excited. Given that the distance between the two sources is d then the total magnetic field at a distance ρ in the far-field is given by:

$$\mathbf{H} = -\widehat{a}_z \frac{I_m}{\eta} \sqrt{\frac{\mathrm{j}\beta}{8\pi}} \frac{\mathrm{e}^{-\mathrm{j}\,\beta\rho}}{\sqrt{\rho}} \left[2\cos\left(\frac{\beta d}{2}\sin\phi\right)\right] \tag{3.49}$$

Notice that if we choose $\beta d/2$ to be odd multiples of $\pi/2$, then at $\phi = \pi/2$ and $\phi = 3\pi/2$ the radiation pattern of this structure exhibits nulls. Now, when trying to model this configuration in FDTD, the destructive interference between the two sources along the direction of the nulls, is not exactly predicted due to dispersion. This implies that the radiation pattern for these angles does not vanish but exhibits some finite value. Moreover, if the distance between the sources is electrically large, in the direction of the nulls the radiation pattern exhibits minor lobes whose maximum values can be comparable to that of the actual pattern.

The above scenario was modeled using both the Yee algorithm as well as the Case 2 scheme. A relatively coarse discretization of $\lambda/6$ was chosen, and two different distances from the source were examined, namely 2.5 λ and 5.5 λ. The excitation of the domain is realized by imposing a soft

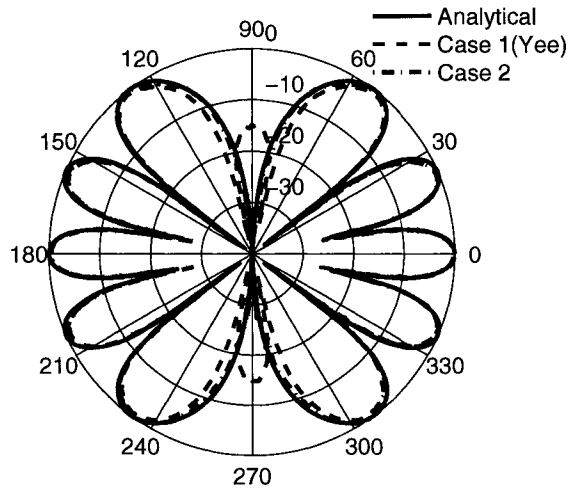

(a) Relative distance $d = 2.5\,\lambda$.

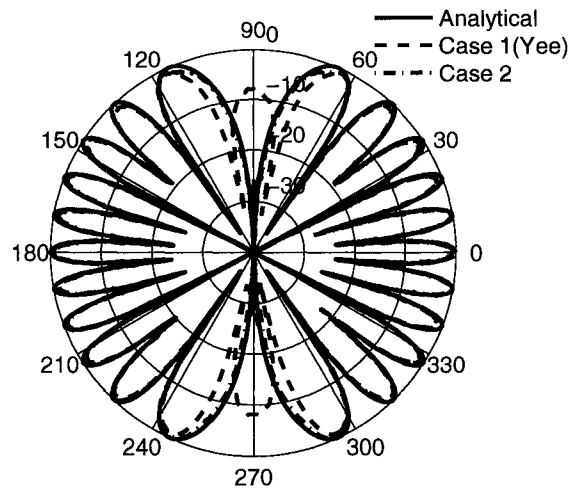

(b) Relative distance $d = 5.5\,\lambda$.

Fig. 3.12: Radiation pattern predictions of two infinite current sources uniformly excited. Discretization $h = \lambda/6$.

source condition on the appropriate H_z components. Since this is a single frequency problem we can take advantage of the isotropic properties of the Case 2 numerical velocity, and so we optimized it with respect to the dispersion error at the particular frequency of interest. This was achieved by setting the numerical wave vector equal to its exact value along some direction. This can be realized by appropriately scaling the free space material properties. The corresponding radiation patterns are shown in Figs. 3.12(a) and 3.12(b). It can be seen that along $\phi = \pi/2$ and $\phi = 3\pi/2$ the Yee scheme exhibits a spurious minor lobe while the Case 2 scheme does not. Also in the L_2 error sense, the Case 2 scheme outperform the Yee scheme as indicated in Table 3.2.

3.8.4. Waveguide propagation constant

In this example a parallel plate waveguide is modeled. The TE_z mode is excited by injecting a z-directed magnetic field, with a very sharp differentiated Gaussian pulse time dependence. The dimensions of the waveguide are 13 cm by 50 cm, and the cell size is set equal to 1 cm. The propagation constant information is extracted using the following procedure. The time-history of the electric field component E_x is observed along two transverse planes separated by a distance d. Then, the above quantities are Fourier-transformed, and the information for each excited mode is obtained by utilizing the orthogonality properties of the field eigenfunctions, that is:

$$E_x = -\frac{\mathrm{j}\beta}{k_c} A_n \cos\left(\frac{n\pi x}{d}\right) \mathrm{e}^{-\mathrm{j}\beta y} \Rightarrow \int_0^d E_x \cos\left(\frac{m\pi x}{d}\right) \mathrm{d}x = -\frac{\mathrm{j}\beta}{k_c} A_n \pi \delta_{mn} \mathrm{e}^{-\mathrm{j}\beta y} \quad (3.50)$$

Then, we divide the integrated quantities for the two observation planes and the ratio is equal to $\mathrm{e}^{-\mathrm{j}\beta d}$, and hence the values of β can be easily extracted. The propagation constant of the first seven modes are computed using the Yee, the Case 2, and the Case 3 scheme. The corresponding results are shown in Figs. 3.13(a)-3.13(b) and Fig. 3.14. It can be seen that the results corresponding to the Case 2 and especially the Case 3 scheme, are in better agreement to the theoretical expected ones than are the results obtained by the Yee scheme.

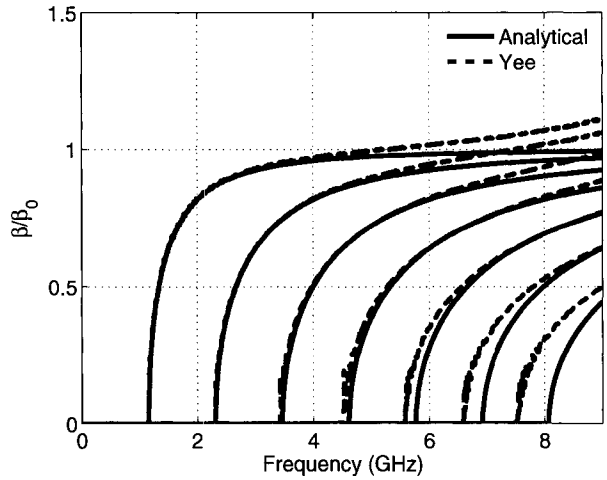

(a) Yee.

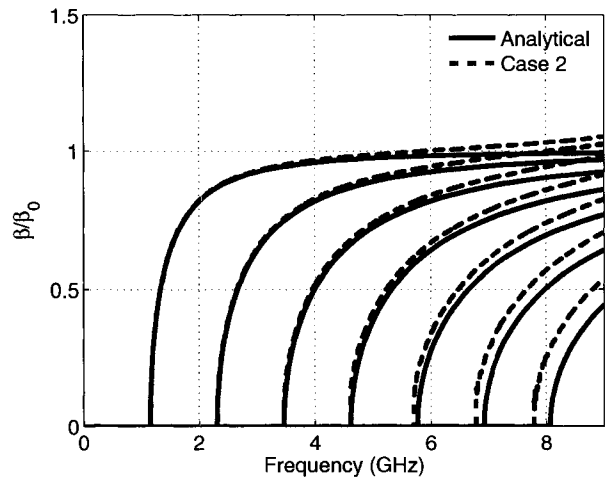

(b) Case 2.

Fig. 3.13: Normalized propagation constant β/β_0 versus frequency.

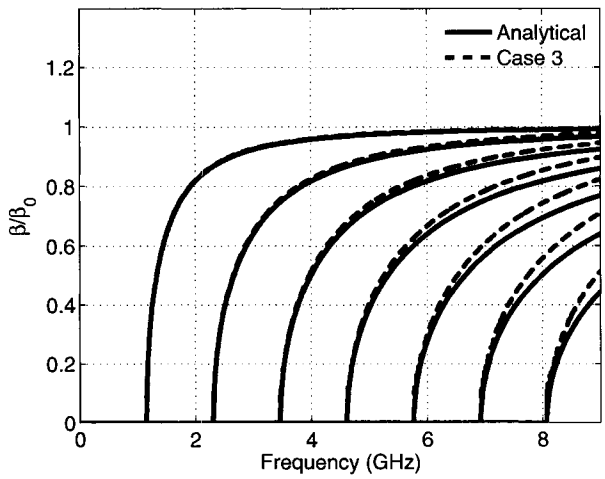

Fig. 3.14: Normalized propagation constant β/β_0 versus frequency. Case 3

3.8.5. Scattering width

In the last example we compute the scattering width of an infinite (along the z-direction) dielectric cylinder of circular cross-section. This scattering scenario is modeled using the Yee and the Case 2 scheme. Four different cylinders are examined under a TE_z uniform plane wave illumination, and the results are compared against the analytical solution given by:

$$\mathrm{SW} = \frac{\sigma_{2D}}{\lambda} = 2\pi \left| \sum_n \frac{J_n(\beta_1 a)\, J_n'(\beta_0 a) - \frac{1}{\sqrt{\varepsilon_r}} J_n'(\beta_1 a)\, J_n(\beta_0 a)}{\frac{1}{\sqrt{\varepsilon_r}} J_n'(\beta_1 a)\, H_n^{(2)}(\beta_0 a) - J_n(\beta_1 a)\, H_n^{(2)'}(\beta_0 a)} \mathrm{e}^{\mathrm{j}n\phi} \right|^2 \tag{3.51}$$

Comparative plots are shown in Figs. 3.15-3.16 where it can be seen that both schemes are in good agreement with the analytical solution. Comparisons with respect to the L_2 error are summarized in Table 3.3, and it can be concluded that the Case 2 scheme is somewhat more accurate. As before, since this is a single frequency problem, the Case 2 numerical velocity was optimized with respect to the dispersion error.

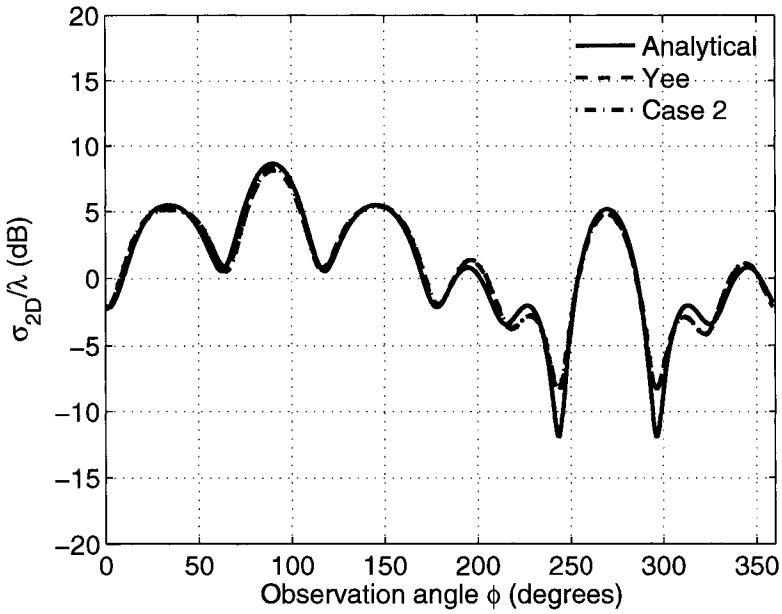

(a) $\varepsilon_r = 3$, $h = \lambda/30$, $a = 20\,h$.

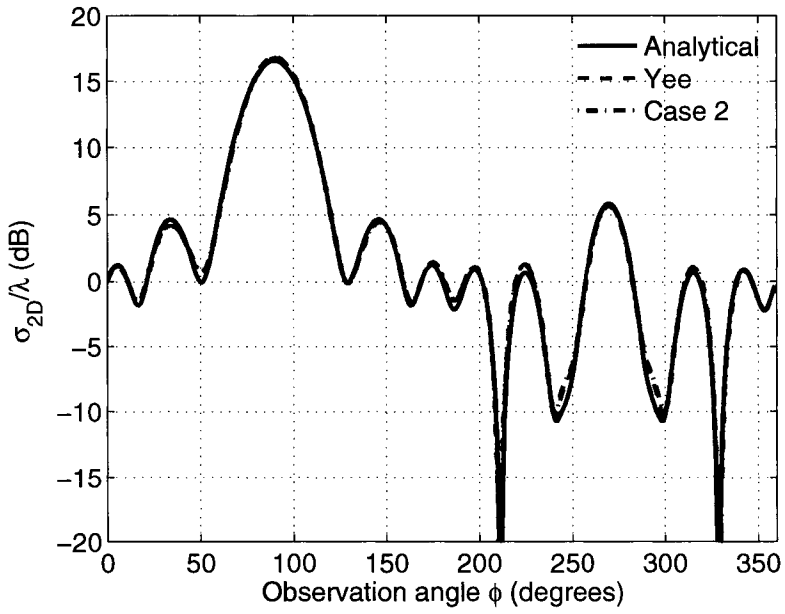

(b) $\varepsilon_r = 3$, $h = \lambda/30$, $a = 30\,h$.

Fig. 3.15: Scattering width predictions of an infinite circular dielectric cylinder.

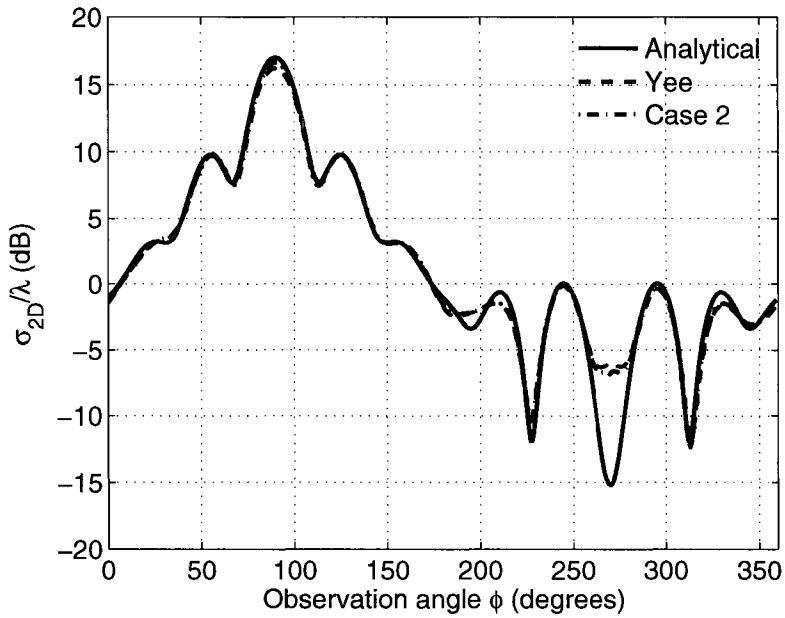

(a) $\varepsilon_r = 2, h = \lambda/20, a = 20\,h.$

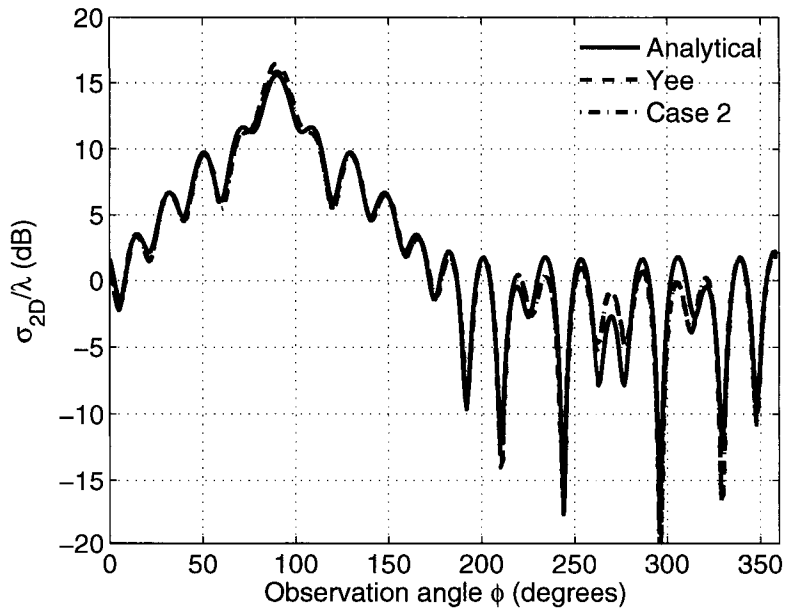

(b) $\varepsilon_r = 2, h = \lambda/20, a = 30\,h.$

Fig. 3.16: Scattering width predictions of an infinite circular dielectric cylinder.

Table 3.3: L_2 error comparisons for scattering width predictions of a dielectric cylinder.

Permittivity	Discretization	Cylinder radius	Yee	Case 2
$\varepsilon_r = 2$	$h = \lambda/20$	$20\,h$	1.6019	0.9311
		$30\,h$	1.7069	0.7756
$\varepsilon_r = 3$	$h = \lambda/30$	$20\,h$	0.2680	0.2151
		$30\,h$	0.6713	0.4564

3.9. Maximization of $S_x^2 C_y + S_y^2 C_x$

In this section we derive the maximum value of the following quantity:

$$J = \sin^2\left(\frac{x}{2}\right)\left[\alpha + 2\beta\cos(y)\right] + \sin^2\left(\frac{y}{2}\right)\left[\alpha + 2\beta\cos(x)\right] \tag{3.52}$$

given that $\alpha + 2\beta = 1$. For simplicity we set:

$$\sin^2\left(\frac{x}{2}\right) \equiv x \quad \text{and} \quad \sin^2\left(\frac{y}{2}\right) \equiv y$$

therefore

$$J = x\,(1 - 4\beta y) + y\,(1 - 4\beta x) \tag{3.53}$$

with $x, y \in [0, 1]$. It is

$$J = (A - 4\,\beta\,B)\,x + B \tag{3.54}$$

where

$$A \equiv 1 - 4\beta y \quad \text{and} \quad B \equiv y$$

We examine the following cases:

1. $A - 4\,\beta\,B > 0$

   Then J is monotonically increasing, therefore

   $$J_{max} = J(x = 1) = A + (1 - 4\beta)B = 1 + (1 - 8\beta)y$$

   and

(a) if $1 - 8\beta > 0$ then $J_{max} = J(x = 1; y = 1) = 2 - 8\beta$

(b) if $1 - 8\beta \leq 0$ then $J_{max} = J(x = 1; y = 0) = 1$

2. $A - 4\beta B \leq 0$

Then J is monotonically decreasing, therefore

$$J_{max} = J(x = 0) = B = y$$

and obviously

$$J_{max} = J(x = 0; y = 1) = 1$$

We can conclude that

$$J_{max} = \max_{\beta} \{1, 2 - 8\beta\}, \ \forall \beta \in \mathbb{R} \tag{3.55}$$

CHAPTER 4

THREE DIMENSIONAL EXTENDED-CURL SCHEMES

4.1. Introduction

In this chapter a three-dimensional finite-difference time-domain scheme is presented with improved isotropy characteristics and possessing higher Courant number than the standard Yee scheme. The basic idea is to transversely extend the curl operator in order to improve the transverse Laplacian representation of the curl-curl operator. A stability analysis is performed, and the dispersion characteristics of the proposed scheme are investigated. It is shown that the proposed scheme is significantly more isotropic than the standard finite-difference time-domain scheme. Additionally, it is proved that under certain conditions a unity Courant number can be achieved, and the resulting scheme is characterized by dispersion characteristics complementary to those of the regular finite-difference time-domain scheme. Numerical simulations are performed that validate the theoretically derived results.

This chapter is structured as follows: in Section 4.2 the formulation of the proposed scheme, is discussed and the corresponding update equations are presented. In Sections 4.3 and 4.4 stability and dispersion analyses are performed. Also, in Section 4.5 the scheme's performance is studied from a different perspective and its relation to the non-physical grid decoupling effect is detailed. Finally, in Section 4.6 simple numerical experiments are performed that validate the proposed scheme.

4.2. Formulation

In Chapter 3 it was demonstrated that the inherent phase velocity anisotropy of a 2-D FDTD grid, can be attributed to the representation of the transverse Laplacian associated with the curl-curl operator. More precisely it was shown that during an FDTD time-step the Laplacian term in the

following equation

$$-\mu\,\varepsilon\,\partial_{tt}\,E_z = \partial_z\left(\partial_x\,E_x + \partial_y\,E_y\right) - \nabla^2_{x,y}\,E_z \tag{4.1}$$

is implicitly approximated via a strongly anisotropic 5-point representation. Starting from this observation it was claimed and proven that if a more isotropic representation is utilized, the grid anisotropy can be drastically reduced. In what follows, this idea is extended and implemented for the 3-D FDTD formalism. Before proceeding with further details of the formulation it is beneficial, for the support and theoretical justification of the proposed scheme, to address the issue of a Laplacian's isotropy, through the definition of its quantitative measure.

Due to its even symmetry and direction invariance property, the most general, second order accurate, Laplacian representation is [30, 31]:

$$\begin{aligned}\nabla^2\,u_{ij} = {} & c_0\,u_{i,j} + \\ & + c_1\left(u_{i+1,j} + u_{i-1,j} + u_{i,j+1} + u_{i,j-1}\right) + \\ & + c_2\left(u_{i+1,j+1} + u_{i+1,j-1} + u_{i-1,j-1} + u_{i-1,j+1}\right)\end{aligned} \tag{4.2}$$

From the Laplacians' family defined above, the member that exhibits the best isotropy can be determined by inspecting the dispersion properties of its truncation error term, and more precisely, the dispersion variations with respect to direction. For this reason, first we need to take the 2-D Taylor expansion of (4.2) and then calculate the combination of c_0, c_1 and c_2 that yields the most isotropic truncation error term [31, pp. 39]. Following this procedure it is revealed that the only approximation that meets this requirement is the one shown in (4.3). Notice that the leading error term is the biharmonic operator, whose perfect isotropy can be easily verified by computing its Fourier transform, i.e. $\mathcal{F}\left\{\nabla^4\right\} = |\mathbf{k}|^4$. Obviously the operator's dispersion properties are independent of the propagation angle. For comparison purposes let us examine the error introduced by the 5-point Laplacian related to the regular FDTD scheme. In this case the corresponding approximation is given by (4.2) if we set $(c_0, c_1, c_2) \equiv (-4, 1, 0)$, and yields the following leading error term: $-\frac{h^2}{12}\left(\partial_x^4 + \partial_y^4\right) u_{i,j}$.

$$\begin{aligned}\nabla^2 u_{i,j} &= \frac{1}{6h^2}\Big[-20\,u_{i,j} + \\ \nabla^2 u_{i,j} &\doteq 4\,(u_{i+1,j} + u_{i-1,j} + u_{i,j+1} + u_{i,j-1}) + \\ &\quad + (u_{i+1,j+1} + u_{i+1,j-1} + u_{i-1,j-1} + u_{i-1,j+1})\Big] - \\ &\quad - \frac{h^2}{12}\nabla^4 u_{i,j} + \mathcal{O}\left(h^4\right)\end{aligned} \tag{4.3}$$

The Fourier transform of this differential operator is: $\mathcal{F}\left\{\partial_x^4 + \partial_y^4\right\} = |\mathbf{k}|^4\left(\cos^4\phi + \sin^4\phi\right)$, and evidently its dispersion characteristics are dependent on the direction of propagation. It follows that, in contrast to the previous case, this truncation error term introduces dispersion discrepancies anisotropically into the grid. It has to be mentioned that in terms of isotropy, and second order accuracy, approximation (4.3) is the best we can get. For any desired improvement, such as higher order isotropic leading error terms, Laplacian approximations with more degrees of freedom are necessary which can be realized by widened finite difference stencils.

For the development of the proposed scheme in 3-D, the framework of the Yee scheme is adopted, that is, the update equations retain their curl form and the electric and magnetic field components are staggered both in space and time. Similar to the 2-D case the transverse Laplacian term is not explicitly computed, but rather implicitly. The implicit Laplacian calculation can be intuitively thought of as a two stage procedure where the intermediate one determines its accuracy. This scenario is illustrated in the following diagram, and essentially it is the FDTD realization of (4.1).

$$\begin{array}{ccccc} E_z^n & \xrightarrow{\nabla\times} & H & \xrightarrow{\nabla\times} & E_z^{n+1} \\ & \underbrace{\qquad\qquad\qquad\qquad\qquad\qquad} & & & \\ & \nabla^2_{x,y}\text{+cross terms} & & & \end{array} \tag{4.4}$$

It can be seen that the H values determine how many E_z values from the n-th time-step, and in what combination, contribute to the calculation of E_z at the next time-step. Put differently, the H

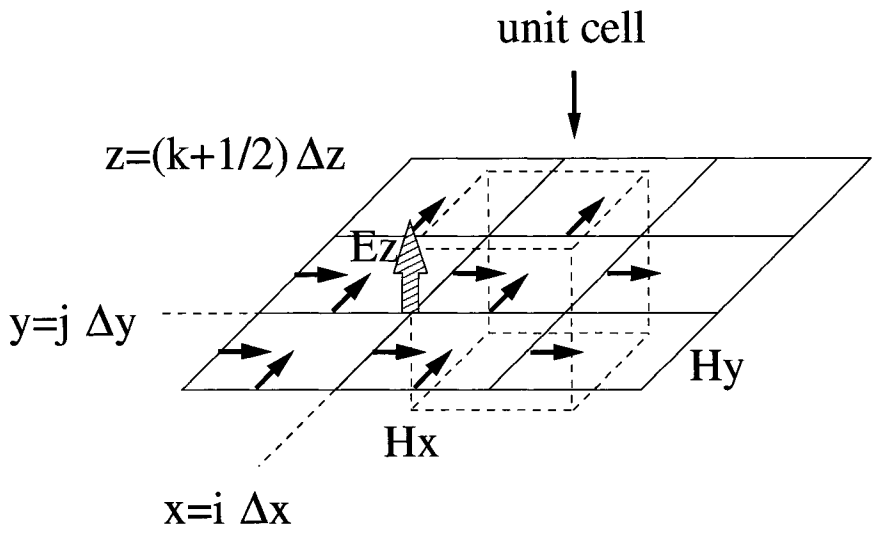

(a)

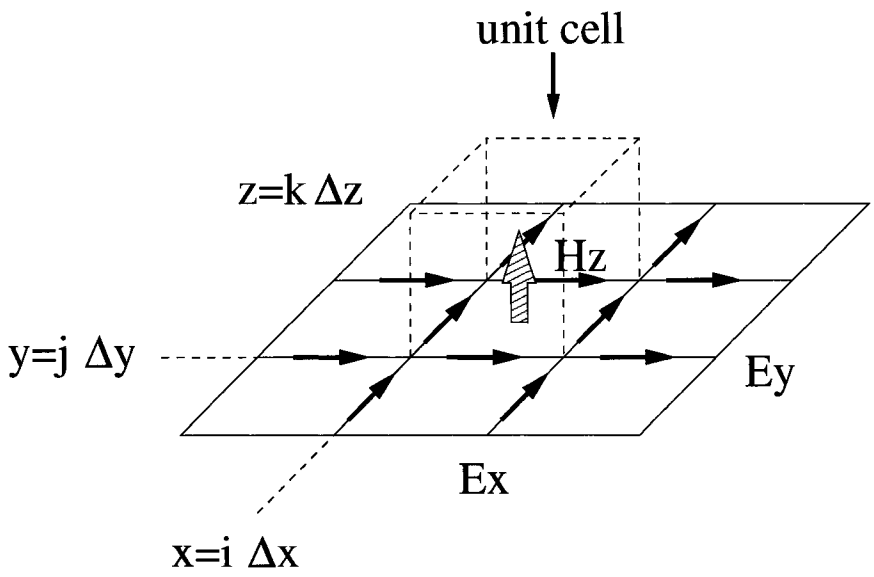

(b)

Fig. 4.1: Extended-curl stencil for E_z and H_z.

$$
\begin{aligned}
E_z\Big|_{i,j,k+1/2}^{n+1} &= E_z\Big|_{i,j,k+1/2}^{n} \\
&+\frac{\Delta t}{\mu}\Bigg[\ \beta\Big(\delta_x H_y\Big|_{i,j+1,k+1/2}^{n+1/2} - \delta_y H_x\Big|_{i+1,j,k+1/2}^{n+1/2}\Big)+ \\
&\quad +\alpha\Big(\delta_x H_y\Big|_{i,j,k+1/2}^{n+1/2} - \delta_y H_x\Big|_{i,j,k+1/2}^{n+1/2}\Big)+ \\
&\quad +\beta\Big(\delta_x H_y\Big|_{i,j-1,k+1/2}^{n+1/2} - \delta_y H_x\Big|_{i-1,j,k+1/2}^{n+1/2}\Big)\Bigg]
\end{aligned}
\tag{4.5}
$$

$$
\begin{aligned}
H_z\Big|_{i+1/2,j+1/2,k}^{n+3/2} &= H_z\Big|_{i+1/2,j+1/2,k}^{n+1/2} \\
&+\frac{\Delta t}{\mu}\Bigg[\ \beta\Big(\delta_y E_x\Big|_{i+3/2,j+1/2,k}^{n+1} - \delta_x E_y\Big|_{i+1/2,j+3/2,k}^{n+1}\Big)+ \\
&\quad +\alpha\Big(\delta_y E_x\Big|_{i+1/2,j+1/2,k}^{n+1} - \delta_x E_y\Big|_{i+1/2,j+1/2,k}^{n+1}\Big)+ \\
&\quad +\beta\Big(\delta_y E_x\Big|_{i-1/2,j+1/2,k}^{n+1} - \delta_x E_y\Big|_{i+1/2,j-1/2,k}^{n+1}\Big)\Bigg]
\end{aligned}
\tag{4.6}
$$

components link E_z components from consecutive time-steps and regulate the Laplacian's form. In our case a Laplacian with 9 non-zero elements, instead of 5, is desired to be recovered. In order to increase the number of contributing E_z components, it is required that an extended-curl stencil be utilized as shown in Fig. 4.1(a). The extended-curl operator can be viewed as a longitudinal extension of the involved derivatives approximation, with respect to the direction of the derived component. Furthermore, notice that unlike the 2-D case, in a 3-D space, transverse Laplacians can be defined in all three major planes, i.e. $x-y$, $x-z$ and $y-z$. Therefore, since for all six field components a transverse plane can be defined, each component can be associated to a 2-D Laplacian, through equations like (4.1). Consequently, for all six update equations an extended-curl stencil is applicable. For instance in Fig. 4.1(b) there is the extended-curl stencil for H_z. According to this convention the update equations for E_z and H_z for a linear, isotropic and uniform medium are the ones shown in (4.5) and (4.6), respectively, where $\alpha = \frac{5}{6}$ and $\beta = \frac{1}{12}$. For compactness we utilized

the central difference operator defined as: $\delta_x u_i = \left(u_{i+1/2} - u_{i-1/2}\right)/\Delta x$. The great advantage of this curl modification is that superior isotropy can be achieved without having to resort to different grid topologies and without having to introduce additional field components. Additionally, notice that although we are working in a 3-D space, we aim for the improvement of the fundamental 2-D transverse Laplacian operator. Under this consideration we have determined how to tailor the curl operators; and apparently their transverse planar extension is sufficient for substantial isotropy improvement. An alternative interpretation of this scheme, which further justifies the proposed modification of the update equations, is given in Section 4.5.

Now, in order to permit accurate and physically meaningful results the proposed scheme should implicitly be flux conservative. More precisely, if a problem's initial conditions are divergence free, this condition must be satisfied at any time instant. For the extended-curl scheme it can be proved that for any cell in the grid the following condition holds:

$$\delta_t \left(\delta_x D_x\Big|_{i,j,k}^{n+1/2} + \delta_y D_y\Big|_{i,j,k}^{n+1/2} + \delta_z D_z\Big|_{i,j,k}^{n+1/2} \right) = 0 \tag{4.7}$$

which is the discretized version of $\partial_t \nabla \cdot \mathbf{D} = 0$. In the same manner we can derive the discrete version of the magnetic charge conservation formula.

4.3. Stability analysis

The stability analysis of the proposed scheme is performed by employing a standard von Neumann analysis. If we assume a 3-D unbounded, linear space then the time-step bound that ensures numerical stable simulations is obtained if spatial discrete Fourier modes of the form:

$$u_{i,j,k}^{n} = \hat{u}^{n}\left(\mathbf{k}\right) \mathrm{e}^{-\mathrm{j}(k_x\, i\, \Delta x + k_y\, j\, \Delta y + k_z\, k\, \Delta z)} \tag{4.8}$$

are substituted in the update equations. The resulting homogeneous system of finite difference equations can be cast in the following matrix form:

$$\widehat{\mathbf{u}}^{n+1} = \mathbf{G}\,\widehat{\mathbf{u}}^{n} \tag{4.9}$$

where $\widehat{\mathbf{u}}^{n} = \left[\hat{E}_x^{\,n}\ \hat{E}_y^{\,n}\ \hat{E}_z^{\,n}\ \hat{H}_x^{\,n+1/2}\ \hat{H}_y^{\,n+1/2}\ \hat{H}_z^{\,n+1/2}\right]^T$ is the state space vector, and $\mathbf{G}$ is the amplification matrix given by:

$$\mathbf{G} = \mathbf{I}_{6\times 6} + \begin{bmatrix} \mathbf{0}_{3\times 3} & \zeta\,\mathbf{A} \\ -\eta\,\mathbf{A} & \zeta\eta\mathbf{B} \end{bmatrix} \tag{4.10}$$

where

$$\mathbf{A} = \begin{bmatrix} 0 & S_z C_y & -S_y C_z \\ -S_z C_x & 0 & S_x C_z \\ S_y C_x & -S_x C_y & 0 \end{bmatrix} \tag{4.11}$$

and $\mathbf{B}$ is given in (4.12).

$$\mathbf{B} = \begin{bmatrix} S_z^2 C_x C_y + S_y^2 C_x C_y & -S_x S_y C_y C_z & -S_x S_z C_y C_z \\ -S_x S_y C_x C_y & S_x^2 C_y C_z + S_z^2 C_x C_y & -S_y S_z C_x C_z \\ -S_x S_z C_x C_y & -S_y S_z C_x C_y & S_y^2 C_x C_z + S_x^2 C_y C_z \end{bmatrix} \tag{4.12}$$

Also, $\zeta \equiv 2\,\mathrm{j}\,\Delta t/\varepsilon$, $\eta \equiv 2\,\mathrm{j}\,\Delta t/\mu$, $S_w \equiv \sin\left(k_w \Delta w/2\right)/\Delta w$, and $C_w \equiv \alpha + 2\,\beta\cos\left(k_w \Delta w\right)$ with $w \in \{x, y, z\}$. The eigenvalues of the amplification matrix are the following:

$$\lambda_{1,2} = 1, \quad \lambda_{3,4,5,6} = 1 - 2\,\Psi \pm 2\sqrt{-\Psi + \Psi^2} \tag{4.13}$$

where $\Psi \equiv -\zeta\,\eta\left(S_x^2\,C_y\,C_z + S_y^2\,C_x\,C_z + S_z^2\,C_x\,C_y\right)$. The scheme is stable if the absolute value of all eigenvalues is less or equal to one, which leads to the following time-step constraint:

$$\Delta t \leq \frac{1}{c\sqrt{J}} \tag{4.14}$$

where for brevity we set $J \equiv S_x^2 C_y C_z + S_y^2 C_x C_z + S_z^2 C_x C_y$, and $c = 1/\sqrt{\varepsilon \mu}$ is the speed of light in the material being modeled. The minimum upper bound of Δt determines the Courant-Friedrichs-Lewy (CFL) condition. The latter is obtained if we allow $\Delta x \equiv \Delta y \equiv \Delta z \equiv h$, and substitute the maximum value of the square rooted quantity. Thus:

$$\Delta t \leq \frac{1}{\sqrt{3}\,|a - 2\beta|}\frac{h}{c} = \frac{\sqrt{3}}{2}\frac{h}{c} \tag{4.15}$$

Notice that when $(\alpha, \beta) \equiv (1, 0)$ (4.15) reduces to the CFL condition of the conventional 3-D FDTD scheme, i.e. $S = \sqrt{3}/3$. The choice $\alpha = \frac{5}{6}$ and $\beta = \frac{1}{12}$ gives a CFL condition of $S = \sqrt{3}/2$.

Thus as in the 2-D case we notice that the time-step bound can be considered a function of two arbitrary real numbers, α and β. Hence, it becomes really intriguing to study its behavior and identify whether it is possible to relax more the already restrictive CFL condition. We begin our investigation by examining the dependency between α and β. One way [1] to realize this, is by checking the consistency of the proposed finite difference formula. Using Taylor series expansions it is straightforward to show that:

$$\begin{aligned}&(\alpha + 2\beta)\,\partial_x u_{i,j+1/2,k} = \\ &\beta\,\delta_x u_{i,j+3/2,k} + \alpha\,\delta_x u_{i,j+1/2,k} + \beta\,\delta_x u_{i,j-1/2,k} + \mathcal{O}\left(\Delta x^2\right)\end{aligned} \tag{4.16}$$

Obviously, the above relation represents a derivative approximation if

$$\alpha + 2\beta = 1 \tag{4.17}$$

For reasons that will become apparent later in our discussion, let us first examine whether it is possible, and under what conditions, to achieve $S = 1$. This implies that:

$$\Delta t \leq \frac{h}{c} \leq \frac{1}{\max\limits_{(\alpha,\beta)}\left\{\sqrt{J}\right\}}\frac{h}{c} \Rightarrow \max_{(\alpha,\beta)}\left\{\sqrt{J}\right\} \leq 1 \tag{4.18}$$

[1] An alternative way would be to determine the α and β values that minimize the error of the numerical dispersion relation.

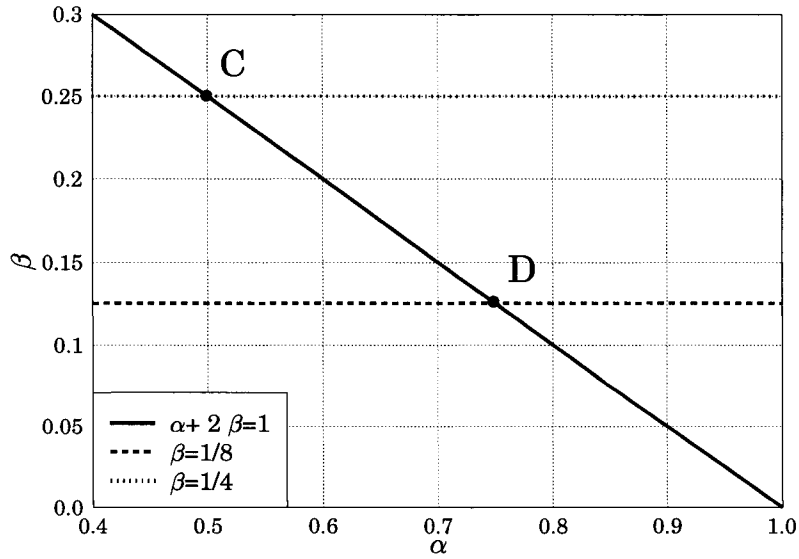

Fig. 4.2: Determination of parameters α and β.

Given the previously derived consistency condition, it can be shown that [Section 4.7]:

$$\max_{(\alpha,\beta)}\{J\} = \max_{\beta}\left\{1, 2-8\beta, 3(1-4\beta)^2\right\} \tag{4.19}$$

If we substitute the above in (4.18) and additionally take into account that the square rooted quantity must be positive, we get the following constraint for β:

$$1/8 \leq \beta \leq 1/4 \tag{4.20}$$

The system of (4.17) and (4.20) can be solved graphically as shown in Fig. 4.2. Similarly to the 2-D case, the solution pairs lie along the solid line section CD, defined by the dotted and dashed lines which means that for this continuum of α and β values, a Courant number $S = 1$ can be achieved. A discussion about the scheme's performance for different (α, β) pairs is given in Sections 4.4 and 4.5.

Now, according to the preceding analysis it could be claimed that were a similar procedure to be followed, the necessary and sufficient conditions, if any, could be derived so that a Courant

$$\begin{bmatrix} S_t & 0 & 0 & 0 & -\xi_z S_z C_y & \xi_y S_y C_z \\ 0 & S_t & 0 & \xi_z S_z C_x & 0 & -\xi_x S_x C_z \\ 0 & 0 & S_t & -\xi_y S_y C_x & \xi_x S_x C_y & 0 \\ 0 & \zeta_z S_z C_y & -\zeta_y S_y C_z & S_t & 0 & 0 \\ -\zeta_y S_y C_x & 0 & \zeta_x S_x C_z & 0 & S_t & 0 \\ \zeta_y S_y C_x & -\zeta_x S_x C_y & 0 & 0 & 0 & S_t \end{bmatrix} \begin{bmatrix} \widehat{E}_x^0 \\ \widehat{E}_y^0 \\ \widehat{E}_z^0 \\ \widehat{H}_x^0 \\ \widehat{H}_y^0 \\ \widehat{H}_z^0 \end{bmatrix} = \mathbf{0} \tag{4.21}$$

number higher than one could be achieved. This statement is false as we prove hereafter. If $S > 1$ then from (4.18) we have $\max\limits_{(\alpha,\beta)} \{J\} = \max\limits_{\beta} \left\{1, 2 - 8\beta, 3(1 - 4\beta)^2\right\} < 1$, which based on ordering arguments is impossible. On that ground, the highest Courant number that can be achieved by the scheme under study is equal to one. It is important to mention that this Courant number comes at the cost of isotropy deterioration as it is demonstrated in the next Section.

4.4. Dispersion analysis

The dispersion relation can be derived if we assume discrete temporal Fourier modes in (4.8), in addition to the spatial ones, or: $\widehat{u}^n = \widehat{u}^0 \, \mathrm{e}^{\mathrm{j}\,\omega\, n\, \Delta t}$. Hence (4.9) yields the eigenvalue problem shown in (4.21). Note that following a procedure similar to the one described in Section 3.7 the conservative nature of this 3D scheme can be verified.

Now, requiring non-trivial solutions for the system in (4.21), leads to the following dispersion relation:

$$\begin{aligned} \left[\frac{1}{c\Delta t} \sin\left(\frac{\omega \Delta t}{2}\right)\right]^2 = {} & \left[\frac{1}{\Delta x} \sin\left(\frac{k_x \Delta x}{2}\right)\right]^2 [\alpha + 2\beta \cos(k_y \Delta y)] [\alpha + 2\beta \cos(k_z \Delta z)] \\ & + \left[\frac{1}{\Delta y} \sin\left(\frac{k_y \Delta y}{2}\right)\right]^2 [\alpha + 2\beta \cos(k_x \Delta x)] [\alpha + 2\beta \cos(k_z \Delta z)] \\ & + \left[\frac{1}{\Delta z} \sin\left(\frac{k_z \Delta z}{2}\right)\right]^2 [\alpha + 2\beta \cos(k_x \Delta x)] [\alpha + 2\beta \cos(k_y \Delta y)] \end{aligned} \tag{4.22}$$

Table 4.1: The most representative three dimensional extended-curl schemes.

Case	Extended curl (α, β)	Courant number S	Laplacian elements (c_0, c_1, c_2)	Leading error term differential operator
1	$(1, 0)$	$\frac{\sqrt{3}}{3}$	$(-4, 1, 0)$	$\partial_x^4 + \partial_y^4$
2	$(\frac{5}{6}, \frac{1}{12})$	$\frac{\sqrt{3}}{2}$	$(-\frac{10}{3}, \frac{2}{3}, \frac{1}{6})$	∇^4
3	$(\frac{3}{4}, \frac{1}{8})$	1	$(-3, \frac{1}{2}, \frac{1}{4})$	$\partial_x^4 + \partial_y^4 + 3\,\partial_{xy}^4$

where $c = 1/\sqrt{\mu\varepsilon}$ is the velocity of light in the medium. Notice that when the discretization vanishes $(\Delta x, \Delta y, \Delta z \rightarrow 0)$, (4.22) yields the constraint equation that governs the propagation of a monochromatic wave, in a general 3-D medium. After substituting $\mathbf{k} = k\,(\sin\theta\cos\phi, \sin\theta\sin\phi, \cos\theta)$, the dispersion relation can be solved iteratively to determine the numerical phase velocity versus propagation angles θ and ϕ.

The dispersion properties of the three most representative implementations of the extended-curl scheme are examined, namely the Yee scheme, the most isotropic and the "Courant number equal to one" scheme, denoted as Case 1, Case 2 and Case 3, respectively. Their characteristics are summarized in Table 4.1.

Figs. 4.3(a)-4.3(b) depict comparative plots of the normalized numerical phase velocity for each case as a function of the elevation angle θ, along two different azimuthal planes: $\phi = 0°$ and $\phi = 45°$. The calculations were performed for a discretization of $\lambda/10$. As expected, the dashed line (Case 2) that corresponds to the most isotropic Laplacian approximation, exhibits highly isotropic phase velocity characteristics in both planes. Moreover, the solid and dotted lines, Case 1 and Case 3 respectively, are characterized by complementary trends, with the latter being overall more isotropic. This is in accordance with the last column of Table 4.1 where we can see that this scheme's Laplacian truncation error term is "closer" to complete a biharmonic operator than the one in Case 1. However, regardless of this scheme's poorer isotropy, compared to Case 2, its

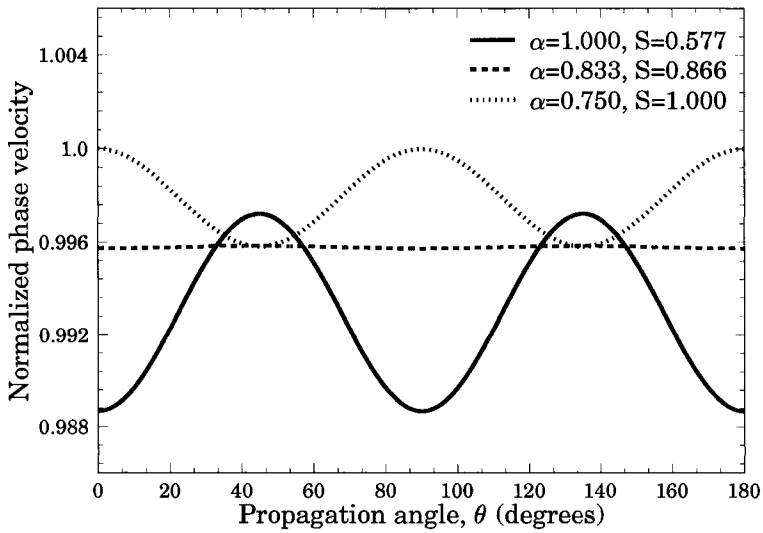

(a) $\phi = 0°$.

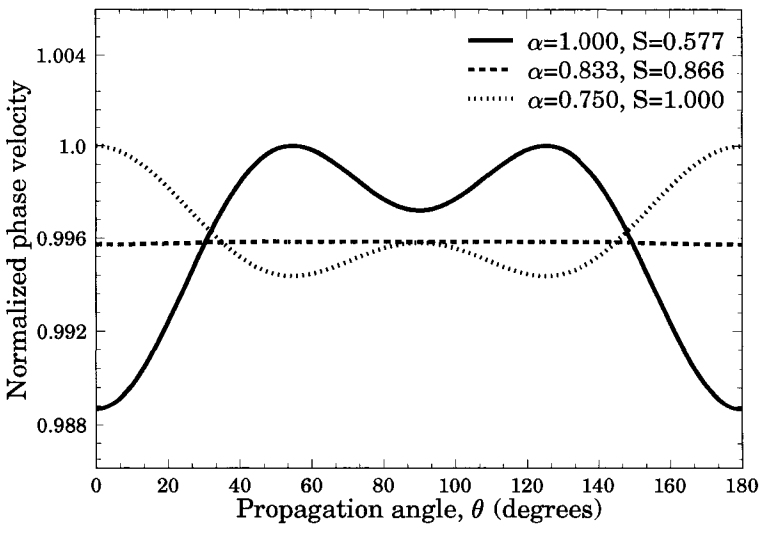

(b) $\phi = 45°$.

Fig. 4.3: Normalized phase velocity.

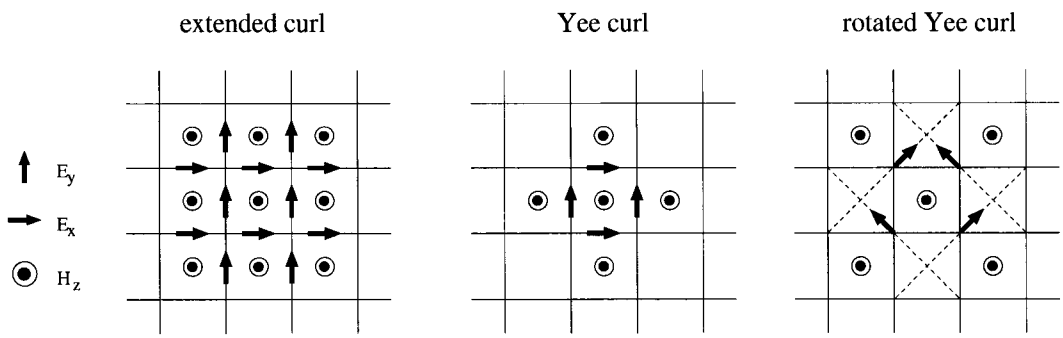

Fig. 4.4: Reformulated extended-curl discretization.

most attractive feature is that for propagation along the principal axis the magic time-step condition ($\Delta t = \Delta x/c$) is satisfied, meaning that the dispersion error is totally eliminated for all frequencies along this axis. This can be very beneficial for the modeling of problems where propagation is primarily concentrated along the principal axis of a Cartesian grid, such as waveguide-like problems.

Similarly to the 2-D case, the choice of (α, β) for Case 3 is the optimal $S = 1$ case. Experimentation with the numerical phase velocity curves revealed that for all other pairs although the magic time-step condition along the principal axis is preserved, the scheme's isotropy characteristics worsen. As a matter of fact the smaller the value of α [moving from D to C in Fig. 4.2], the worse the isotropy becomes.

4.5. Extended-curl and grid decoupling

In this Section we revisit the extended-curl scheme and we try to investigate from a different perspective its behavior as a function of α and β. For simplicity, our analysis assumes a 2-D TE_z field configuration, however it is straightforward to extend these arguments in the case of a 3-D space. The development of the extended-curl scheme was based on a Cartesian grid and a field arrangement as the Yee algorithm suggests. This trait is highly desirable because FDTD over a Cartesian grid is well established, and easier to implement. In what follows, we re-examine the extended-curl

$$\nabla^2 u_{i,j} \approx \frac{2}{3\,h}\left[\left(\frac{u_{i+1,j}-u_{i,j}}{h}-\frac{u_{i,j}-u_{i-1,j}}{h}\right)+\left(\frac{u_{i,j+1}-u_{i,j}}{h}-\frac{u_{i,j}-u_{i,j-1}}{h}\right)\right]+ \\ +\frac{1}{3\,h\sqrt{2}}\left[\left(\frac{u_{i+1,j+1}-u_{i,j}}{h\sqrt{2}}-\frac{u_{i,j}-u_{i-1,j-1}}{h\sqrt{2}}\right)+\left(\frac{u_{i-1,j+1}-u_{i,j}}{h\sqrt{2}}-\frac{u_{i,j}-u_{i+1,j-1}}{h\sqrt{2}}\right)\right] \tag{4.23}$$

concept through a different prism that allows a non-Cartesian field arrangement.

An alternative representation of (4.3) is the one shown in (4.23) [31]. If we correspond $u_{i,j}$ to $H_z(i+1/2, j+1/2)$ then the first square-bracketed term of (4.3) can be considered as a curl operation, which in FDTD naturally results in a perpendicular, to the curl plane, electric field component. The second term is a $\pi/4$-rotated version of the first one and based on the previous argument it also represents a curl operation however the associated electric field components are oriented in accordance to the aforementioned rotation. This is better depicted in Fig. 4.4. It can be seen that there are two fluxes contributing towards the update of $H_z(i+1/2, j+1/2)$: a regular FDTD flux, and a flux generated by the new rotated electric field components. Consequently, as also indicated in the figure, a different path to generate 9-point Laplacians in FDTD is by considering an additional interlaced rhombic grid where along the edges of its unit cell additional field components are defined. Notice that for this case, the latter are collocated with the nodes of the regular FDTD cell. In addition, it can be readily shown (by appropriately manipulating the update equations) that this alternative scheme is mathematically equivalent to the initially proposed extended-curl, in the sense that both of them achieve, through different paths, the recovery of the desired 9-point Laplacian. Their only, yet major, difference is that the extended-curl schemes realize Laplacians by incorporating information from diagonal cells directly in the update equations, using existing field components. In contrast,

the reformulated scheme using a rhombic grid analogy incorporates the same information through the additional, "auxiliary", components.

Now, based on the reformulated extended-curl scheme, the update equation for $H_z(i+1/2, j+1/2)$ can be re-written in the following form, where the Yee grid flux as well as the rotated-Yee grid flux are explicitly used.

$$H_z\Big|_{i+1/2,j+1/2}^{n+3/2} = H_z\Big|_{i+1/2,j+1/2}^{n+1/2} + \frac{\Delta t}{\mu} \times \times \left[(\alpha - 2\beta)\,(\nabla \times \mathbf{E})_z^{Yee} + 4\beta\,(\nabla \times \mathbf{E})_z^{r-Yee} \right]_{i+1/2,j+1/2}^{n+1} \tag{4.24}$$

This expression is valid not only for the isotropic scheme (Case 2) but for every member of the extended-curl family, that is for every (α, β) pair. Hence, we have all the necessary information to explain the following: the authors during their experimentation with the Case 3 scheme noticed that when the grid is excited by localized sources as $\alpha \rightarrow 2\beta$ (or α gets smaller than 3/4) the computational domain exhibited a rather deconstructed field configuration. Recall that, in Section 4.4 it was noted that the choice of $(\alpha, \beta) \equiv (3/4, 1/8)$, for Case 3, is optimal because for any other pair, the scheme's isotropy gets worse. This is an absolutely valid statement albeit theoretical, in the sense that it only explains a function's behavior (the numerical dispersion relation) but lacks physical insight, and of course fails to explain the behavior itself. As $\alpha \rightarrow 2\beta$ severely distorted field configuration ensue because as equation (4.24) shows, the Yee flux term vanishes and the primary flux contribution is due to the rotated-Yee grid components. This creates grid decoupling meaning that only part of the field components are excited resulting in a "sawtooth field pattern". This artifact was first reported in [33] in the context of finite elements Consequently, for the Case 3 scheme the choice of $(\alpha, \beta) \equiv (3/4, 1/8)$ is optimal not only because it is the least anisotropic, but also because it prevents the development of the detrimental, non-physical grid decoupling effect.

A point of interest is that since the extended-curl scheme and its reformulated version are

mathematically equivalent they yield computationally identical results. Moreover, the reformulated version is more compact because all of the field components are contained within a unit cell. This characteristic makes it more flexible to handle material boundaries. Therefore, given a computational domain, this can be partitioned into regions with and without material discontinuities. Then the two schemes could be judiciously interfaced so that the reformulated version handles the regions involving material discontinuities and the initial version the rest of the domain. Of course this comes at the cost of an increase in the computational burden since additional components have to be computed. For this hybridized scheme, caution is required when dealing with perfect electric conductor (PEC) edges. This is because the reformulated scheme essentially assigns finite values to electric field components located on the nodes of the Yee cell. Hence it cannot accurately model the well known field singularity occurring at PEC edges.

4.6. Numerical experiments

In this section numerical experiments are performed to examine the accuracy of the 3-D extended-curl scheme. First, a 3-D domain ($1\ \text{m} \times 1\ \text{m} \times 1\ \text{m}$), is considered and it is uniformly discretized using a cell size of $h = 1$ cm. The computational domain consists of 100^3 cells, and a twelve-cell-thick uniaxial PML is placed around it. The domain is excited by injecting a z-directed electric field, at one of the domain's bottom corners. The source has a differentiated Gaussian pulse time dependence whose frequency spectrum is shown in Fig. 4.5(a). We let the spherical waves propagate and record the time history of E_θ at three equidistant points, with respect to the excitation point, one along the principal axis $\widehat{\mathbf{k}} = (1, 0, 0)$, one along the domain's short diagonal $\widehat{\mathbf{k}} = (1, 1, 0)$, and one along the long diagonal $\widehat{\mathbf{k}} = (1, 1, 1)$.

Simulations are performed for the three Cases of Table 4.1, and the corresponding results are shown in Figs. 4.6(a)-4.6(b). As expected, Case 2 is highly isotropic however the pulse has been

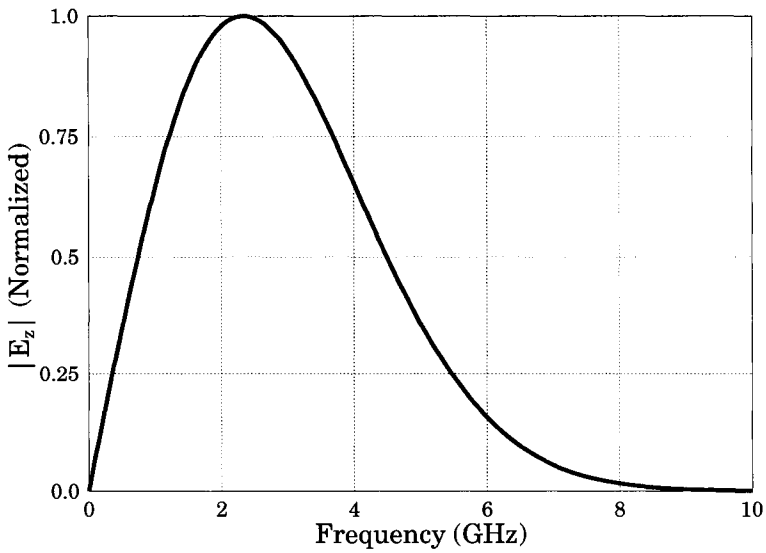

(a)

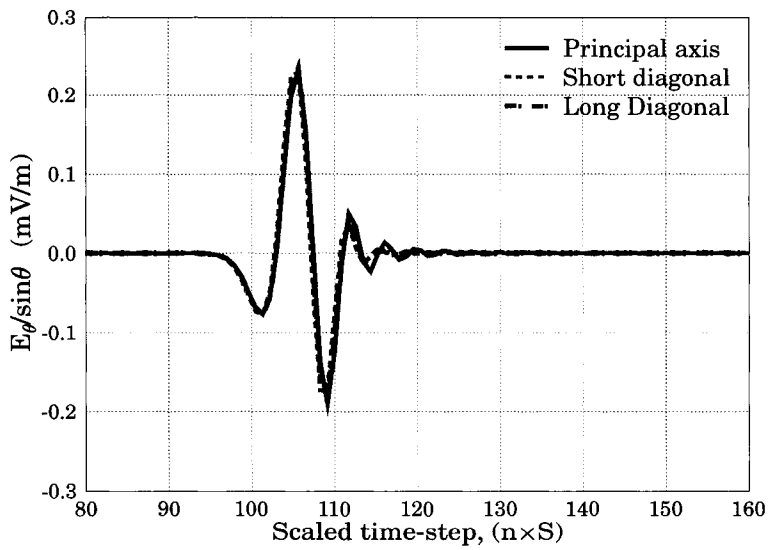

(b) $\alpha = 5/6, S = \sqrt{3}/2$.

Fig. 4.5: Numerical experiments. Cell-size $h = 1$ cm and $h/c = 0.03$ ns. (a) Excitation pulse frequency content. (b) Case 2. Notice that E_θ has been scaled to the elevation angle sine.

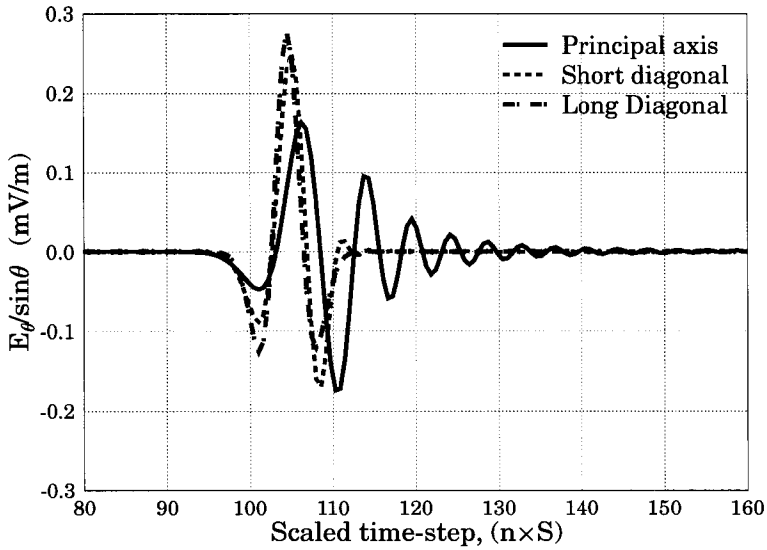

(a) $\alpha = 1, S = \sqrt{3}/3$. Conventional FDTD.

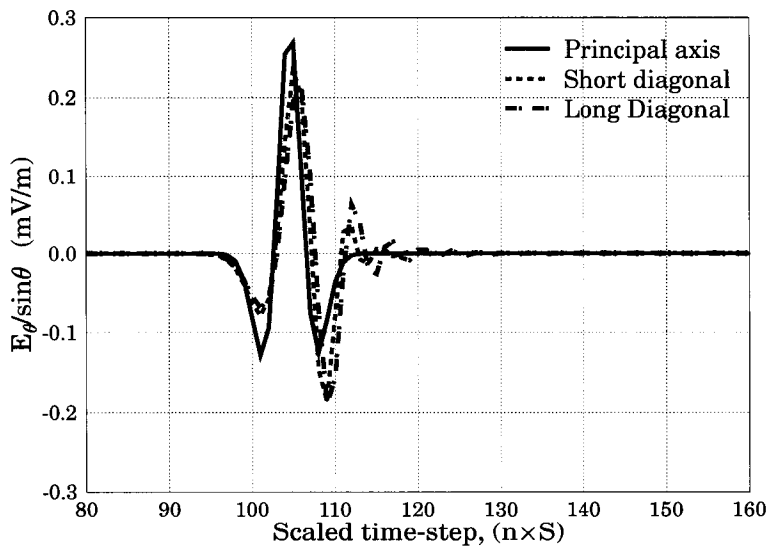

(b) $\alpha = 3/4, S = 1$.

Fig. 4.6: Numerical experiments. Cell-size $h = 1$ cm and $h/c = 0.03$ ns. (a) Case 1. (b) Case 3. Notice that E_θ has been scaled to the elevation angle sine.

distorted due to dispersion errors. Case 3 is essentially the opposite of Case 1 since the best pulse propagation can be achieved along the principal axis and the worst along the direction of the long diagonal. Additionally, due to its mitigated dispersion error characteristics, pulse distortion is not as severe as in the Case 1, and the phase lag is not noticeable.

The second problem we examine is that of a pulse propagation inside an air filled parallel plate TEM waveguide. Propagation is assumed along the y-direction and the TEM (H_x, E_z) mode is excited by appropriately injecting the necessary surface currents. The dimensions of the waveguide are 0.15 m $\times$ 2 m $\times$ 0.15 m and the domain is uniformly discretized using a cell size of $h = 1$ cm. Along the direction of propagation the waveguide is terminated by a 10-cell thick uniaxial PML. Since this is a 3-D problem the sideways infinite extent of the waveguide is modeled using perfect magnetic conductor (PMC) walls. The geometry has been chosen rather elongated so that any dispersion discrepancies of the propagating pulse will be pronounced. Additionally, in order to ensure an undisrupted propagation of the excited mode special treatment is required for the spatial discontinuities created by the PEC and PMC boundaries. The details of this modification are shown in Fig. 4.7(a). For simplicity we have assumed that the PEC wall consists of PEC cubes i.e. the electric field components along all twelve edges surrounding a grid point are set equal to zero. Additionally, all the magnetic field components perpendicular to the cube faces have to be set to zero, in oder to prevent them from coupling with the surrounding space, and exhibit non-zero values. Hence an H_x component parallel and adjacent to the PEC wall requires for its updating two E_z components from the PEC cell, which are naturally set to zero. By employing image theory [36] the value of these perpendicular components are restored and the wave propagation is accurately modeled preventing artificial scattering from the PEC wall. The same recipe has to be used for electric field components parallel to PMC walls. The excitation pulse has a Gaussian profile with significant frequency content up to 3 GHz. Cases 1 and 3 were simulated and in Fig. 4.7(b) there

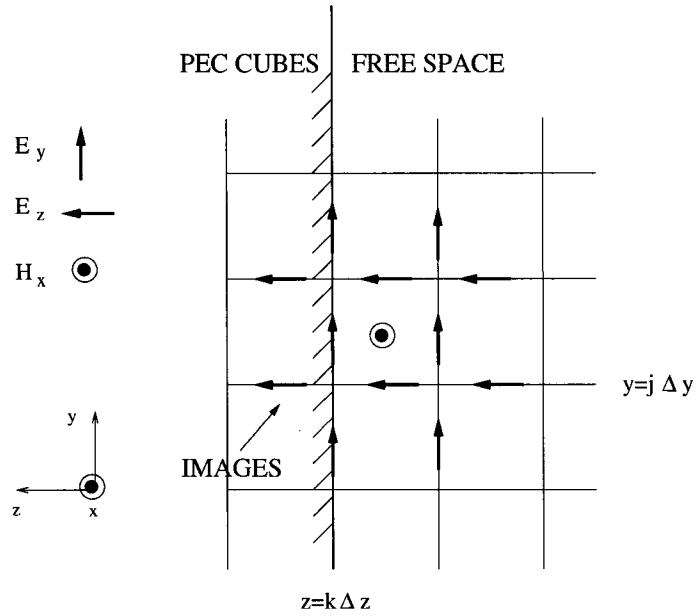

(a)

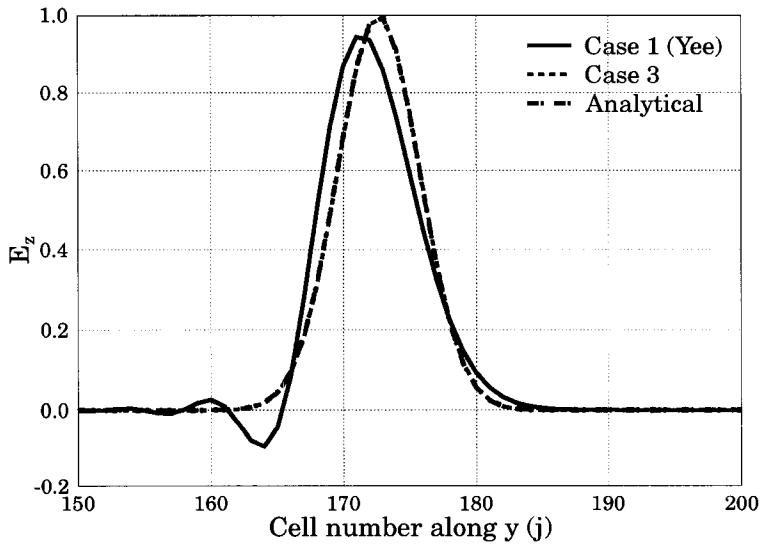

(b)

Fig. 4.7: (a) PEC boundary treatment. (b) Pulse propagation in parallel plate waveguide.

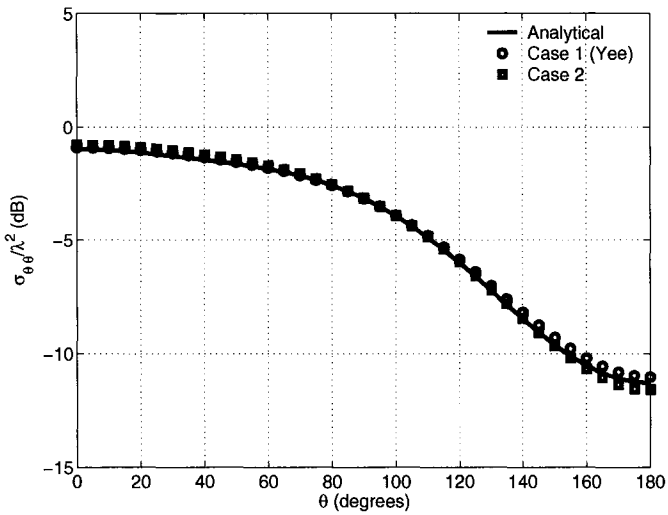

Fig. 4.8: Bistatic radar cross-section (RCS) of a PEC sphere on the $y-z$ plane. ($a = 10h$, $h = \lambda/40$)

are comparative plots of the pulse's spatial variation at a specific time instant. As expected the Yee formulation suffers from dispersion [2], while the Case 3 extended-curl scheme, being dispersion free, is in excellent agreement with the analytical solution. Hence, with this simple test, the accuracy of the method for this specific type of problems is validated, making it a very reliable and precise, wideband modeling tool.

Finally we note that in the parallel plate case due to the geometry's simplicity the image principle is easy to apply, convenient and accurate. This is not usually the case with more complex structures and an attempt for its systematic implementation throughout an arbitrary PEC boundary can be a very laborious programming exercise. Nevertheless simply encoding a PEC sphere with the PEC cube algorithm and without including any image algorithm corrections yields very good results for the backscattered field as shown in Fig. 4.8.

4.7. Maximization of $S_x^2 C_y C_z + S_y^2 C_x C_z + S_z^2 C_x C_y$

In this section we derive the maximum value of the following quantity:

$$\begin{aligned} J &= \sin^2\left(\frac{x}{2}\right)[\alpha + 2\beta\cos(y)][\alpha + 2\beta\cos(z)] + \\ &+ \sin^2\left(\frac{y}{2}\right)[\alpha + 2\beta\cos(x)][\alpha + 2\beta\cos(z)] + \\ &+ \sin^2\left(\frac{z}{2}\right)[\alpha + 2\beta\cos(x)][\alpha + 2\beta\cos(y)] \end{aligned} \tag{4.25}$$

given that $\alpha + 2\beta = 1$. For simplicity we set:

$$\sin^2\left(\frac{x}{2}\right) \equiv x, \quad \sin^2\left(\frac{y}{2}\right) \equiv y \quad \text{and} \quad \sin^2\left(\frac{z}{2}\right) \equiv z$$

therefore

$$\begin{aligned} J =& x\,(1-4\beta y)(1-4\beta z) + y\,(1-4\beta x)(1-4\beta z) + \\ &+ z\,(1-4\beta x)(1-4\beta y) \end{aligned} \tag{4.26}$$

with $x, y, z \in [0, 1]$. It is:

$$J = A\,(1 - 4\,\beta\,z\,) + B\,z \tag{4.27}$$

where

$$\begin{aligned} A &\equiv x\,(1-4\beta y) + y\,(1-4\beta x) \\ B &\equiv (1-4\beta x)(1-4\beta y) \end{aligned}$$

Let us first calculate the maximum value of quantity B. The latter can be expressed as a monomial with respect to x, as:

$$B = -4\,\beta\,(1-4\beta y)x + (1-4\beta y) \tag{4.28}$$

We examine the following cases:

1. $-4\beta(1-4\beta y) > 0$

$$B_{max} = B(x=1) = -4\beta(1-4\beta y) + (1-4\beta y) =$$

$$-4\beta(1-4\beta)y + 1 - 4\beta$$

Since $-4\beta(1-4\beta) > 0$

$$B_{max} = B(x=1; y=1) = (1-4\beta)^2$$

2. $-4\beta(1-4\beta y) \leq 0$

$$B_{max} = B(x=0) = 1 - 4\beta y$$

(a) if $\beta > 0 \Rightarrow 1 - 4\beta y > 0$, then

$$B_{max} = B(x=0; y=0) = 1$$

(b) if $\beta < 0$ then

$$1 - 4\beta y < 0 \Rightarrow \beta > \frac{1}{4y} > 0$$

which is impossible.

(c) if $\beta = 0$ then

$$B_{max} = 1$$

(d) if $1 - 4\beta y = 0$ then

$$B_{max} = 0$$

Therefore we can conclude that:

$$B_{max} = \max_{\beta} \left\{1, (1-4\beta)^2\right\}, \ \forall \beta \in \mathbb{R} \tag{4.29}$$

Now, since (4.27) is a monomial of z, the maximum value of J is given by:

$$J_{max} = \max_{\beta} \{A, B + (1-4\beta)A\}$$

and

$$\max_{\beta}\{A\} = \max_{\beta}\{1, 2-8\beta\} \tag{4.30}$$

We notice that A and B are maximised for different values of x and y, meaning that they cannot always be maximized simultaneously Consequently:

1. if $(x, y) = (0, 0)$ then

$$\max_{\beta}\{B + (1-4\beta)\, A\} = \max_{\beta}\{B\} = 1$$

2. if $(x, y) = (1, 0)$ then

$$\begin{aligned}\max_{\beta}\{B + (1-4\beta)\, A\} &= 1 - 4\beta + (1-4\beta) \max_{\beta}\{A\} \\ &= 2\,(1-4\beta)\end{aligned}$$

3. if $(x, y) = (1, 1)$ then

$$\begin{aligned}\max_{\beta}\{B + (1-4\beta)\, A\} &= \max_{\beta}\{B\} + (1-4\beta) \max_{\beta}\{A\} \\ &= 3(1-4\beta)^2\end{aligned}$$

It can be concluded that:

$$J_{max} = \max_{\beta}\left\{1, 2-8\beta, 3(1-4\beta)^2\right\},\ \forall\beta \in \mathbb{R} \tag{4.31}$$

CHAPTER 5

HIGHER ORDER EXTENDED-CURL SCHEMES

5.1. Introduction

In this Chapter we examine higher order schemes based on the extended-curl operator. Two different scenarios are studied and both result in "hyper-isotropic" schemes. In the first section the extended-curl formalism is further utilized for the implementation of a higher order Laplacian (HOL) approximation. An excellent description on general HOL representations can be found in [37]. Here, we focus on Laplacian representations that utilize a 25-point stencil which are the next possible incremental improvement over the 9-point ones. Their favorable trait is that they can be fourth order accurate, which implies that isotropic properties of sixth order should be expected. Indeed, 25-point Laplacians can exhibit isotropic phase velocity characteristics up to sixth order, and in contrast to the 9-point ones, there are more than one realizations that manifest this property [21, 30]. We concentrate therefore only on isotropic 25-point Laplacians.

In the next section a higher order isotropic FDTD scheme is presented. The enhanced isotropy characteristics are achieved by appropriately combining an extended-curl discretization [38] along with artificial dispersion terms, realized through weighted third order temporal derivatives. For this reason this scheme is denoted as *extended-curl (4,2)*. These dispersion terms are computed using the modified equation approach which replaces them with their spatial equivalent. Their regulatory role in the scheme's performance is revealed by examining the numerical dispersion relation. Hence, it is shown that by judiciously choosing their weighting factor, sixth order isotropy can be achieved. Furthermore, it is shown that the scheme exhibits a higher and rather relaxed Courant number compared to the Yee algorithm. The following analyses are developed for a two dimensional space occupied by a homogeneous, isotropic and non-dissipative medium. A TE_z field

configuration is assumed.

5.2. A higher order Laplacian realization

5.2.1. Formulation

Given that there are multiple isotropic 25-point Laplacian stencils the main issue is the best suited one for our purposes, that is for use in the FDTD update equations. Here we assume a TE_Z mode and investigate the following updating scenario:

$$H_z^n \xrightarrow[\text{curl}]{2\text{–point}} \begin{Bmatrix} E_x \\ E_y \end{Bmatrix} \xrightarrow[\text{ext.-curl}]{N\text{–point}} H_z^{n+1} \sim \nabla_{xy}^2 H_z^n \tag{5.1}$$

The primary factor that motivates which updating scenario we consider is that the extended-curl formalism dictates that the E_x and E_y update equations remain the same as those of the Yee-scheme. For the current field mode this is realized through 2-point curl approximations, which creates the following correspondences: the update of an E_x component requires the pair of the vertically placed, upper and lower H_z components. Similarly, the update of an E_y component, requires the horizontally placed, left and right H_z components. On that account, regardless of the extended-curl operator stencil, the information from the E_x and E_y components is eventually translated into vertical and horizontal H_z pairs. Consequently, one concludes that a 25-point Laplacian can be mapped into FDTD update equations, via an extended-curl operator, if its stencil can be constructed, topologically, as a combination of horizontal and vertical, possibly overlapping, H_z pairs.

After experimentation with all possible isotropic Laplacian stencils, it was concluded that the following rendition is the most straightforward to employ:

$$\nabla^2 u_{i,j} = \frac{1}{60\,h^2}\Big(-252\,u_{i,j} + 52\,\Sigma_1 + 16\,\Sigma_2 - \Sigma_3 - 2\,\Sigma_4 \Big) + \frac{h^4}{90}\nabla^6 u_{i,j} + \mathcal{O}\left(h^6\right) \tag{5.2}$$

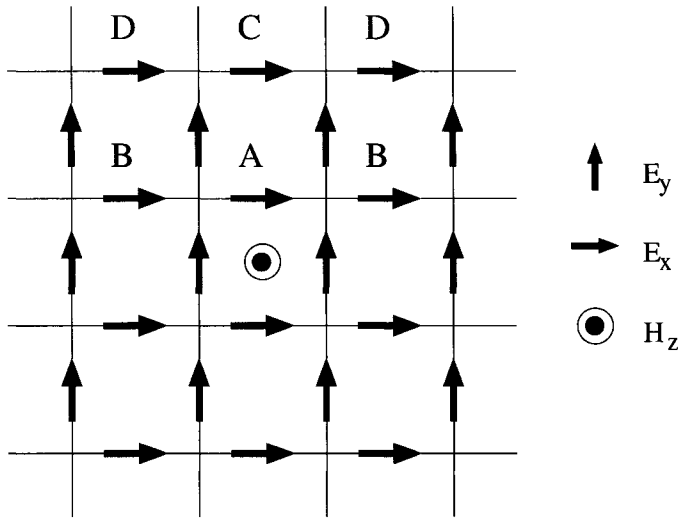

Fig. 5.1: Higher order extended-curl discretization. The weights correspond to E_x components. Due to symmetry only half of them are denoted. The same weighting applies to E_y.

where the Σ terms are:

$$\Sigma_1 \equiv u_{i+1,j} + u_{i-1,j} + u_{i,j+1} + u_{i,j-1} \tag{5.3}$$

$$\Sigma_2 \equiv u_{i+1,j+1} + u_{i+1,j-1} + u_{i-1,j-1} + u_{i+1,j-1} \tag{5.4}$$

$$\Sigma_3 \equiv u_{i+2,j} + u_{i-2,j} + u_{i,j+2} + u_{i,j-2} \tag{5.5}$$

$$\Sigma_4 \equiv u_{i+2,j+1} + u_{i+1,j+2} + u_{i-2,j+1} + u_{i-1,j+2} + \tag{5.6}$$

$$+ u_{i-2,j-1} + u_{i-1,j-2} + u_{i+2,j-1} + u_{i+1,j-2} \tag{5.7}$$

and they correspond to groups of points that exhibit the same $\pi/2$ rotation symmetry. One notices that the above approximation exhibits fourth order accuracy in space, and its LET is the triharmonic operator. This essentially signifies isotropic phase velocity up to sixth order.

Finally, what needs to be determined is the stencil of the extended-curl operator. The latter needs to be compatible with both the stencil of the Laplacian under study, and the Yee algorithm updating of E_x and E_y. Bearing this in mind, it can be easily verified that the spatial operator shown in Fig. 5.1 complies with both conditions. It is noticed that this is both a longitudinal and a

transverse curl extension, as opposed to the transversely extended only one, presented in Section 3.3. The corresponding equation can be written as shown in (5.8)

$$\begin{aligned}\delta_t H_z\Big|^{n+1}_{i+\frac{1}{2},j+\frac{1}{2}} = \frac{1}{\mu}\Bigg[& B\left(\delta_y E_x\Big|^{n+1}_{i+\frac{3}{2},j+\frac{1}{2}} - \delta_x E_y\Big|^{n+1}_{i+\frac{1}{2},j+\frac{3}{2}}\right) \\ & + A\left(\delta_y E_x\Big|^{n+1}_{i+\frac{1}{2},j+\frac{1}{2}} - \delta_x E_y\Big|^{n+1}_{i+\frac{1}{2},j+\frac{1}{2}}\right) \\ & + B\left(\delta_y E_x\Big|^{n+1}_{i-\frac{1}{2},j+\frac{1}{2}} - \delta_x E_y\Big|^{n+1}_{i+\frac{1}{2},j-\frac{1}{2}}\right)\Bigg] - \\ -\frac{1}{\mu}\Bigg[& D\left(\tilde{\delta}_y E_x\Big|^{n+1}_{i+\frac{3}{2},j+\frac{1}{2}} - \tilde{\delta}_x E_y\Big|^{n+1}_{i+\frac{1}{2},j+\frac{3}{2}}\right) \\ & + C\left(\tilde{\delta}_y E_x\Big|^{n+1}_{i+\frac{1}{2},j+\frac{1}{2}} - \tilde{\delta}_x E_y\Big|^{n+1}_{i+\frac{1}{2},j+\frac{1}{2}}\right) \\ & + D\left(\tilde{\delta}_y E_x\Big|^{n+1}_{i-\frac{1}{2},j+\frac{1}{2}} - \tilde{\delta}_x E_y\Big|^{n+1}_{i+\frac{1}{2},j-\frac{1}{2}}\right)\Bigg]\end{aligned} \tag{5.8}$$

where:

$$\tilde{\delta}_x u_i = \frac{u_{i+\frac{3}{2}} - u_{i-\frac{3}{2}}}{\Delta x} \tag{5.9}$$

The weights A, B, C and D are determined following a procedure analogous to that presented in Section 3.3. Hence, by applying equations (3.7), (3.8) and (5.8) during a time-step cycle, one can confirm that the resulting Laplacian approximation is given by:

$$\nabla^2 u_{i,j} \approx \frac{1}{h^2}\Big[-4A\,u_{i,j} + (A - 2B + C)\,\Sigma_1 + (2B + 2D)\,\Sigma_2 - C\,\Sigma_3 - D\,\Sigma_4\Big] \tag{5.10}$$

Then by equating like terms between the above equation and (5.10), we get a system of equations which solution yields:

$$A = \frac{63}{60}, \quad B = \frac{6}{60}, \quad C = \frac{1}{60}, \quad \text{and} \quad D = \frac{2}{60}$$

Equations (3.7), (3.8) and (5.8) constitute what we refer to as the HOL-based scheme. A general remark should be made here that for the reasons described in Section 3.3 we have ensured that this HOL-based scheme is consistent with both of Gauss' Laws. Moreover, the HOL-based scheme

cannot be realized in 3-D. However since 2-D analysis is a useful tool in electromagnetics for many important problems, it is still of great interest to examine the possibility of obtaining hyper-isotropic FDTD formulations in 2-D.

5.2.2. Dispersion and stability analysis of the HOL-based scheme

If we assume a plane wave solution then the numerical dispersion relation for the HOL-based scheme is found to be:

$$\left[\frac{1}{c\Delta t}\sin\left(\frac{\omega\Delta t}{2}\right)\right]^2 = \left(\frac{S_x}{\Delta x}\right)^2\left[C_y^{AB} - \left(3-4S_y^2\right)C_x^{CD}\right] + \\ + \left(\frac{S_y}{\Delta y}\right)^2\left[C_x^{AB} - \left(3-4S_x^2\right)C_y^{CD}\right] \tag{5.11}$$

where

$$C_w^{AB} = A + 2B\cos\left(\tilde{k}_w\Delta w\right) \quad \text{and} \quad C_w^{CD} = C + 2D\cos\left(\tilde{k}_w\Delta w\right)$$

The features of the scheme are better revealed after Taylor-expanding the above, where we obtain:

$$\left(\frac{\omega}{c}\right)^2 + \mathcal{O}\left(\Delta t^2\right) = \tilde{k}_x^2 + \tilde{k}_y^2 - \\ - \frac{1}{90}\left[\Delta x^4\tilde{k}_x^6 + \Delta y^4\tilde{k}_y^6 + 3\Delta x^2\Delta y^2\left(\tilde{k}_x^4\tilde{k}_y^2 + \tilde{k}_x^2\tilde{k}_y^4\right)\right] + \\ + \mathcal{O}\left(\Delta x^6\right) + \mathcal{O}\left(\Delta y^6\right) \tag{5.12}$$

Evidently, the scheme is second order accurate in time and fourth order in space. Notice however that for a uniform discretization, the LET is the triharmonic operator which ensures numerical phase velocity isotropy up to 6-th order. For comparison purposes, the corresponding Taylor-expanded numerical dispersion relation for the most popular higher order FDTD scheme, namely the Fang (2,4) scheme [3], is given by:

$$\left(\frac{\omega}{c}\right)^2 + \mathcal{O}\left(\Delta t^2\right) = \tilde{k}_x^2 + \tilde{k}_y^2 - \frac{3}{320}\left(\Delta x^4\tilde{k}_x^6 + \Delta y^4\tilde{k}_y^6\right) + \\ + \mathcal{O}\left(\Delta x^6\right) + \mathcal{O}\left(\Delta y^6\right) \tag{5.13}$$

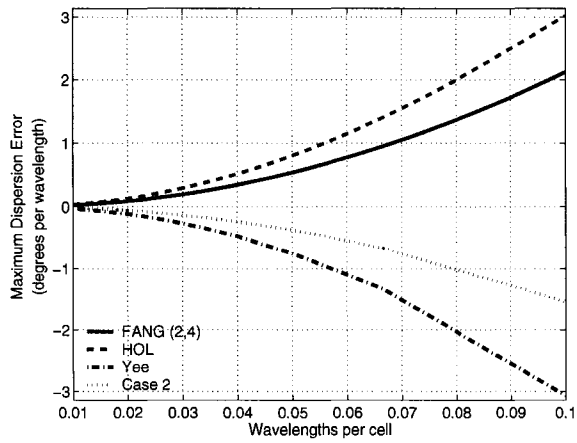

Fig. 5.2: Maximum algebraic dispersion error.

This scheme is second order accurate in time and fourth order in space; however, in contrast to (5.12) the LET is dependent on the propagation angle. Moreover, it is important to note that the coefficients of the two LETs, of equations (5.12) and (5.13), are of the same order. This is critical because, if the coefficient of the LET in (5.13) was substantially less than one, the introduced anisotropy error would be insignificant, and hence the two schemes would not be comparable in absolute terms.

Furthermore, the stability limit of the HOL-based scheme can be obtained if we solve (5.12) with respect to the angular frequency ω and require the latter being real for all values of $\tilde{k}_x$ and $\tilde{k}_y$. Accordingly, the time-step bound that ensures stability is given by:

$$\Delta t \leq \sqrt{\frac{10}{9}} \frac{h}{c\sqrt{2}} \tag{5.14}$$

Notice that for the derivation of the above condition a square cell of size h has been assumed, since for this type of grids the proposed scheme exhibits its superior characteristics. Additionally, (5.14) is less restrictive than the corresponding conditions, for the Yee and the Fang (2,4) scheme (the time-step bound for the former is given by $\Delta t \leq \frac{h}{c\sqrt{2}}$ and for the latter by $\Delta t \leq \frac{6h}{7c\sqrt{2}}$).

Unfortunately the HOL-based scheme for time-steps close to the Courant limit propagates waves at superluminar speeds. This is a deficiency of all FDTD schemes that approximate spatial

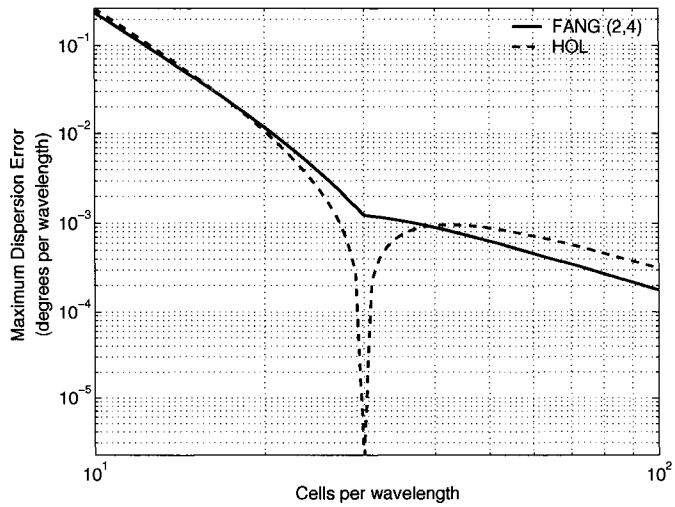

(a)

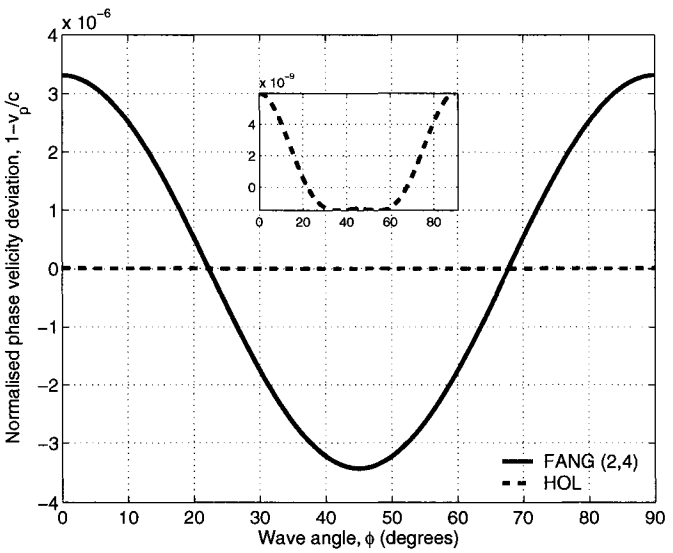

(b)

Fig. 5.3: (a) Maximum dispersion error. (b) Phase velocity velocity deviation. Optimization at $N_\lambda = 30$.

derivatives in higher orders than the temporal ones [2]. This is in contrast to the Yee or any other scheme that exhibits identical spatial and temporal discretization errors. The above are illustrated in Fig. 5.2, where the algebraic[1] value of the maximum dispersion error is plotted as a function of the inverse resolution N_λ^{-1}. For all schemes the maximum stable time-step is used. It can be seen that the HOL-based scheme, as well as the Fang (2,4) deviate positively from the zero dispersion error curve, which is a direct consequence of superluminarity.

These curves are juxtaposed with the ones that correspond to the Yee and the Case 2 scheme, which both deviate negatively. Moreover, it should be mentioned that the latter two schemes exhibit their optimum behaviour at the Courant stability limit, and in particular their dispersion error is upper bounded by the zero dispersion error curve. Nevertheless, this is not the case when it comes to the HOL-based, as well as the Fang (2,4) scheme. More precisely by reducing the time-step or equivalently by reducing the Courant number, the temporal error can become comparable to the spatial one and even cancel each other out. At this point the dispersion error curve exhibits a zero-crossing which means that for the discretization that this occurs, superior accuracy can be achieved. As a matter of fact, there can be an optimal Courant number which minimizes the dispersion error over all propagation angles, for a fixed resolution [18]. Its derivation requires the minimization of some appropriately chosen quantity. For example if we define as an optimization constraint the minimization of the following quantity:

$$J = \int_0^{\pi/2} \left| 1 - \frac{\tilde{v}_p}{c} \right| \mathrm{d}\phi \tag{5.15}$$

Then by using a simple searching algorithm the Courant number can be determined that guarantees superior accuracy for a given N_λ.

[1]We define the algebraic maximum dispersion error ζ as:

$$|\zeta| = 360^\circ \max_{\phi} \left\{ \left| 1 - \frac{\tilde{v}_p}{c} \right| \right\}$$

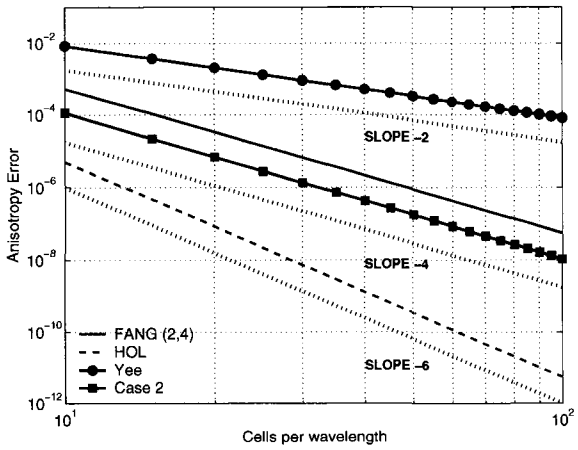

Fig. 5.4: Anisotropy error.

The above optimization procedure was applied to both the HOL-based and the Fang (2,4) scheme, for a discretization of $N_\lambda = 30$. The corresponding results are shown in Figs. 5.3(a) and 5.3(b). As regards to the maximum dispersion error it can be seen that although both schemes exhibit the same rate of descent, the HOL-based for the optimized resolution exhibits a deep null which, apparently, indicates almost total elimination of the dispersion error. Note here that the corresponding Courant numbers are $S = 0.0763$ and $S = 0.0557$ for the HOL-based and the Fang (2,4) scheme, respectively.

Additionally in Fig. 5.3(b) the phase velocity deviation $1 - \frac{\tilde{v}_p}{c}$, is depicted at $N_\lambda = 30$, as a function of the propagation angle. The HOL-based scheme is substantially more isotropic and from the inset figure we can see that the magnitude of its phase velocity deviation, is 10^3 times less than that of the Fang (2,4).

Finally, the scheme's performance with respect to the anisotropy error is also depicted in Fig. 5.4. As expected the performance of the HOL-based scheme is outstanding. From the same figure we also observe that although the Case 2 and the Fang (2,4) are both fourth order isotropic, the former introduces less anisotropy error.

In conclusion the following points should be emphasized. First of all in Fig. 5.2 it can be

seen that the Fang (2,4) is less dispersive than the HOL-based scheme. This is attributed to the fact that the LET coefficients may be of the same order, however the Fang (2,4) one is slightly smaller, hence it is less dispersive. This is true provided that the same time integration scheme is applied, meaning that the same amount of temporal discretization error is introduced. Furthermore it should be mentioned that comparing the HOL-based scheme to the Fang (2,4) is not absolutely "fair". In particular, in terms of accuracy the schemes are comparable since both exhibit the same temporal as well as spatial accuracy. However, in terms of Laplacian realization, the Fang (2,4) essentially recovers the stencil of a 49-point Laplacian. Therefore a "fair" comparison would be against a HOL-based scheme that utilises an isotropic 49-point Laplacian stencil. Nonetheless, it was demonstrated that just a 25-point Laplacian realization is sufficient to create an FDTD scheme with performance comparable to that of the Fang (2,4), which clearly indicates that the extended-curl scheme achieves a more efficient stencil utilization.

5.3. A higher order isotropic FDTD scheme using artificial dispersion via controllable higher order time derivatives

5.3.1. Motivation

In our previous publications [38] and [39] it was demonstrated that the inherent anisotropy of the Yee algorithm can be attributed to the anisotropic approximation of the 2-D transverse Laplacian associated to the curl-curl operator. Furthermore, it was demonstrated that with the aid of a transversely extended curl operator (Fig. 5.5) any 9-point Laplacian approximation can be mapped onto FDTD update equations. Hence by mapping an isotropic 9-point Laplacian approximation, a fourth order isotropic FDTD scheme can be realized. This is better revealed if we Taylor-expand the right-

hand side of the corresponding numerical dispersion relation. It is

$$\text{RHS} = \left(\frac{\alpha}{2} + \frac{\beta}{4}\right)\tilde{k}^2 + \left[-\frac{h^2}{32}\left(\frac{\alpha}{2} + 3\beta\right) - \frac{h^2}{96}\left(\frac{\alpha}{2} - 5\beta\right)\cos(4\phi)\right]\tilde{k}^4 + \mathcal{O}\left(h^4\right) \quad (5.16)$$

where a uniform cell size h has been assumed and the wavevector has been written in polar form as $(\tilde{k}_x, \tilde{k}_y) = \tilde{k}(\cos\phi, \sin\phi)$. Notice that if we set $\alpha = 5/6$ and $\beta = 1/12$, (5.16) yields

$$\text{RHS} = \frac{1}{4}\tilde{k}^2 - \frac{h^2}{48}\tilde{k}^2 + \mathcal{O}\left(h^4\right) \quad (5.17)$$

which clearly indicates that fourth order isotropy has been achieved. Essentially the extended curl approach introduces two parameters α and β which values are chosen so that the angle dependent term is eliminated. However these two degrees of freedom are not enough in order to achieve an even higher degree of isotropy. In particular, the next term of the expansion in (5.16) is given by

$$\left[\frac{h^4}{1152}\left(\frac{\alpha}{2} + 7\beta\right) + \frac{h^4}{640}\left(\frac{\alpha}{6} - 3\beta\right)\cos(4\phi)\right]\tilde{k}^6$$

where it is obvious that the trigonometric term cannot be eliminated, given the previous choice for α and β. It has to be mentioned here that, strictly speaking, a scheme can be characterized as isotropic if the Taylor expanded right hand side of its numerical dispersion relation, can be written as

$$\text{RHS} = \sum_{m=1}^{M} c_m \tilde{k}^{2m}, \quad \text{with at least } c_1 \neq 0 \quad (5.18)$$

5.3.2. Formulation

From the above analysis it becomes apparent that the key idea is to introduce an additional degree of freedom in the scheme which should allow the coefficient in (5.3.1) to be independent of the propagation angle. Note that the extra degree of freedom should not disrupt the already isotropic $\tilde{k}^4$ term.

For this purpose we consider the fourth order temporal derivative approximation, or

$$\frac{\partial u^n}{\partial t} = \delta_t u^n - \frac{\Delta t^2}{24}\frac{\partial^3 u^n}{\partial t^3} + \mathcal{O}\left(\Delta t^4\right) \quad (5.19)$$

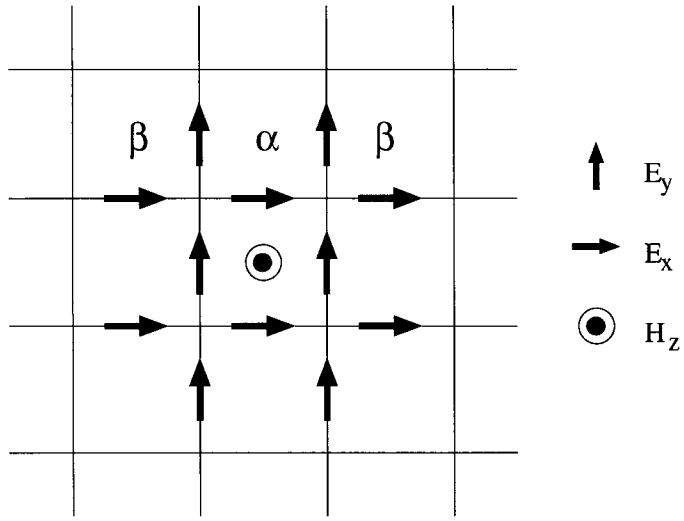

Fig. 5.5: Extended-curl stencil for H_z update. The E_x and E_y components are updated according to the Yee algorithm.

where

$$\delta_t u^n = \frac{u^{n+1/2} - u^{n-1/2}}{\Delta t} \tag{5.20}$$

However, we let the contribution of the third order time derivative term, be controlled by a real constant γ, which essentially gives the desired extra degree of freedom. Given the above, the update equation for H_z is modified as follows

$$\delta_t H_z\Big|_{i+1/2,j+1/2}^{n+1} - \gamma \frac{\Delta t^2}{24} \frac{\partial^3 H_z}{\partial t^3}\Big|_{i+1/2,j+1/2}^{n+1} = -\frac{1}{\mu} (\nabla \times \mathbf{E})_z \Big|_{i+1/2,j+1/2}^{n+1} \tag{5.21}$$

Similarly, the update equations for E_x and E_y are given by:

$$\delta_t E_x\Big|_{i+1/2,j}^{n+1/2} - \gamma \frac{\Delta t^2}{24} \frac{\partial^3 E_x}{\partial t^3}\Big|_{i+1/2,j}^{n+1/2} = \frac{1}{\varepsilon} (\nabla \times \mathbf{H})_x \Big|_{i+1/2,j}^{n+1/2} \tag{5.22}$$

and

$$\delta_t E_y\Big|_{i,j+1/2}^{n+1/2} - \gamma \frac{\Delta t^2}{24} \frac{\partial^3 E_y}{\partial t^3}\Big|_{i,j+1/2}^{n+1/2} = \frac{1}{\varepsilon} (\nabla \times \mathbf{H})_y \Big|_{i,j+1/2}^{n+1/2} \tag{5.23}$$

It is interesting to note that $\partial^3/\partial t^3$ terms play essentially the role of a regulatory artificial dispersion, where we recall that for the wave equation even order time derivatives introduce dispersion (while

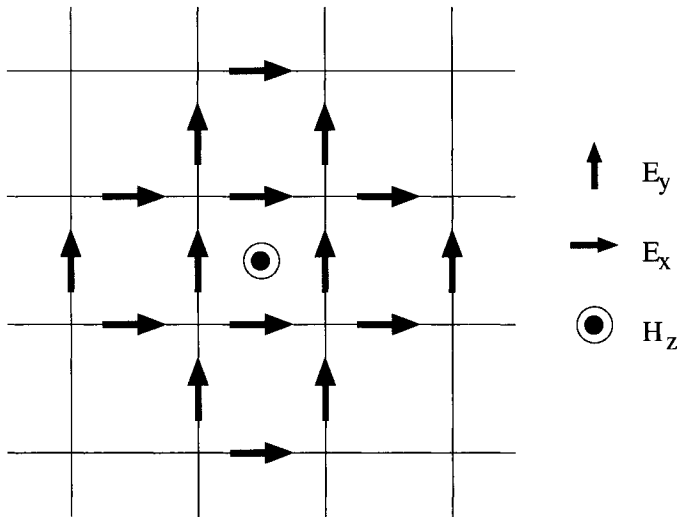

Fig. 5.6: Additional components required for the approximation of $\partial_t^3 H_z$.

odd order ones introduce dissipation). For the calculation of these terms, and in order to obtain explicit FDTD update equations, the modified equation approach is employed [31]. Hence through successive differentiations of the Maxwell's equations we obtain

$$\partial_t^3 \begin{bmatrix} \mathbf{E} \\ \mathbf{H} \end{bmatrix} = \begin{bmatrix} 0 & \frac{1}{\varepsilon^2 \mu} \\ -\frac{1}{\varepsilon \mu^2} & 0 \end{bmatrix} \nabla \times \nabla^2 \begin{bmatrix} \mathbf{E} \\ \mathbf{H} \end{bmatrix} \tag{5.24}$$

For the TE_z field configuration the above yields

$$\partial_t^3 \begin{bmatrix} E_x \\ E_y \\ H_z \end{bmatrix} = \begin{bmatrix} 0 & 0 & \frac{1}{\varepsilon^2 \mu} \nabla_{xy}^2 \partial_y \\ 0 & 0 & -\frac{1}{\varepsilon^2 \mu} \nabla_{xy}^2 \partial_x \\ \frac{1}{\varepsilon \mu^2} \nabla_{xy}^2 \partial_y & -\frac{1}{\varepsilon \mu^2} \nabla_{xy}^2 \partial_x & 0 \end{bmatrix} \begin{bmatrix} E_x \\ E_y \\ H_z \end{bmatrix} \tag{5.25}$$

Since the third order spatial derivative terms are multiplied by Δt^2, it suffices to approximate them through second order accurate expressions. Hence we have

$$\begin{aligned} \frac{\partial^3 E_y}{\partial x^3}\Big|_{i+1/2,j+1/2}^{n+1} = \frac{1}{\Delta y^2 \, \Delta x} \Big(& E_y\Big|_{i+2,j+1/2}^{n+1} - 3\, E_y\Big|_{i+1,j+1/2}^{n+1} \\ & + 3\, E_y\Big|_{i,j+1/2}^{n+1} - E_y\Big|_{i-1/2,j+1/2}^{n+1} \Big) \end{aligned} \tag{5.26}$$

and

$$\frac{\partial^3 E_y}{\partial y^2 \partial x}\Big|^{n+1}_{i+1/2,j+1/2} = \frac{1}{\Delta x^3}\Big(E_y\Big|^{n+1}_{i+1,j+3/2} - 2\,E_y\Big|^{n+1}_{i+1,j+1/2} + E_y\Big|^{n+1}_{i+1,j-1/2} - E_y\Big|^{n+1}_{i,j+3/2} + 2\,E_y\Big|^{n+1}_{i,j+1/2} - E_y\Big|^{n+1}_{i,j-1/2}\Big) \tag{5.27}$$

The additional components required for the above approximations are shown in Fig. 5.6. In the case of the H_z update, by comparison to the stencil in Fig. 5.5, it can be seen that only four extra points are needed. For the third order time derivative approximation of E_x and E_y, a combination of H_z components is required, corresponding to the blue and red group of components respectively, shown in Fig. 5.6. Given that the original 2D extended curl scheme requires only two H_z components for the update of E_x and E_y, it can be concluded that the modification under discussion requires six more components for each one of them.

5.3.3. Dispersion and stability analysis

Now that we have determined the form of the update equations, it is straightforward to derive the corresponding numerical dispersion relation. Hence by assuming a discrete spatio-temporal Fourier mode as the solution, the following relation can be readily derived

$$\left[\frac{1}{c\Delta t}\sin\left(\frac{\omega\Delta t}{2}\right)\right]^2 = \left[\frac{1}{\Delta x}\sin\left(\frac{\tilde{k}_x\Delta x}{2}\right)\right]^2\left[\alpha + 2\beta\cos\left(\tilde{k}_y\Delta y\right) - \gamma\frac{u}{6}\right]\left(1 - \gamma\frac{u}{6}\right) + \left[\frac{1}{\Delta y}\sin\left(\frac{\tilde{k}_y\Delta y}{2}\right)\right]^2\left[\alpha + 2\beta\cos\left(\tilde{k}_x\Delta x\right) - \gamma\frac{u}{6}\right]\left(1 - \gamma\frac{u}{6}\right) \tag{5.28}$$

with

$$u \equiv (c\,\Delta t)^2\left\{\left[\frac{1}{\Delta x}\sin\left(\frac{\tilde{k}_x\Delta x}{2}\right)\right]^2 + \left[\frac{1}{\Delta y}\sin\left(\frac{\tilde{k}_y\Delta y}{2}\right)\right]^2\right\} \tag{5.29}$$

In order to determine the values of the parameters α, β and γ we examine the behavior of the Taylor expansion coefficients. It is

$$\begin{aligned}
&\left(\frac{\omega}{c}\right)^2 + \mathcal{O}\left(\Delta t^2\right) = \\
&= \left(\alpha + 2\beta\right)\tilde{k}^2 - \\
&- \left[\frac{\alpha - 5\beta}{48}\cos(4\phi) - + \frac{\gamma S^2}{24}\left(1 + \alpha + 2\beta\right) + \frac{\alpha + 6\beta}{16}\right] h^2\tilde{k}^4 + \\
&+ \left\{\left[\frac{\gamma S^2}{576}\left(1 + \alpha - 4\beta\right) + \frac{\alpha - 18\beta}{960}\right]\cos(4\phi) + \right. \\
&\qquad \left. + \frac{\gamma^2 S^4}{576} + \frac{\gamma S^2}{192}\left(1 + \alpha + 4\beta\right) + \frac{\alpha + 14\beta}{576}\right\} h^4\tilde{k}^6 + \mathcal{O}\left(h^6\right)
\end{aligned} \tag{5.30}$$

We notice that for second order accuracy the coefficient of the first term should be equal to one, or

$$\alpha + 2\beta = 1 \tag{5.31}$$

For fourth order isotropy the coefficient of the trigonometric term in the second expansion term should vanish, or:

$$\alpha - 5\beta = 0 \tag{5.32}$$

Finally, for sixth order isotropy the coefficient of the trigonometric term in the third expansion term should vanish, or:

$$\frac{\gamma S^2}{576}\left(1 + \alpha - 4\beta\right) + \frac{\alpha - 18\beta}{960} = 0 \tag{5.33}$$

The three previous relations constitute a system of equations which solution yields

$$\alpha = \frac{5}{6}, \quad \beta = \frac{1}{12}, \quad \text{and} \quad \gamma S^2 = \frac{4}{15}, \quad \text{where} \quad S = \frac{c\Delta t}{h}$$

The above combination of values results in the following Taylor-expanded right-hand side of (5.28)

$$\text{RHS} = \frac{1}{4}\tilde{k}^2 - \frac{19}{720}h^2\tilde{k}^4 + \frac{107}{64800}h^4\tilde{k}^6 + \mathcal{O}\left(h^6\right) \tag{5.34}$$

where obviously a sixth order isotropy is indicated. Additionally, by employing a standard von-Neumann analysis it can be shown that the time-step bound that ensures a stable scheme is the

following:

$$\Delta t \leq 0.9745 \frac{h}{c} \tag{5.35}$$

The scheme's performance is demonstrated in Figs. 5.7(a) and 5.7(b). In Fig. 5.7(a) the normalized phase velocity deviation, defined as

$$e_{\text{disp}} = \frac{v_p}{c} - \text{mean}\left\{\frac{v_p}{c}\right\} \tag{5.36}$$

is depicted as a function of the propagation angle for a fixed resolution $N_\lambda = 10$. Obviously the proposed scheme outperforms the others. Furthermore in Fig. 5.7(b) the scheme's sixth order isotropy is demonstrated where the isotropy error versus resolution is shown, defined as

$$e_{\text{anis}} = \max_{\phi}\left\{\frac{v_p}{c}\right\} - \min_{\phi}\left\{\frac{v_p}{c}\right\} \tag{5.37}$$

In addition the scheme's performance with respect to the maximum algebraic dispersion error is shown in Fig. 5.8. Notice that the proposed scheme does not support superluminal phase velocities and its dispersion characteristics are similar to the Case 2 scheme.

5.4. Numerical examples

In this numerical experiment we calculate the resonances of a rectangular cavity whose boundaries correspond to perfect electric conductors ($\widehat{\mathbf{n}} \times \mathbf{E} = \mathbf{0}$). The dimensions of the cavity are 0.0615 m $\times$ 0.027 m, and it is uniformly discretised with a 41 $\times$ 18 grid. Simulations were performed using the Fang (2,4), the HOL-based and the extended-curl (4,2) scheme. In all simulations the maximum allowable time-step was used. The TE_Z mode is excited in the cavity by injecting a z-directed magnetic field at its center with a very sharp differentiated Gaussian pulse time dependence. A sufficient amount of time-steps was executed so that a 1 MHz frequency resolution is achieved. In the cases necessary, image theory is facilitated for the boundary treatment. In

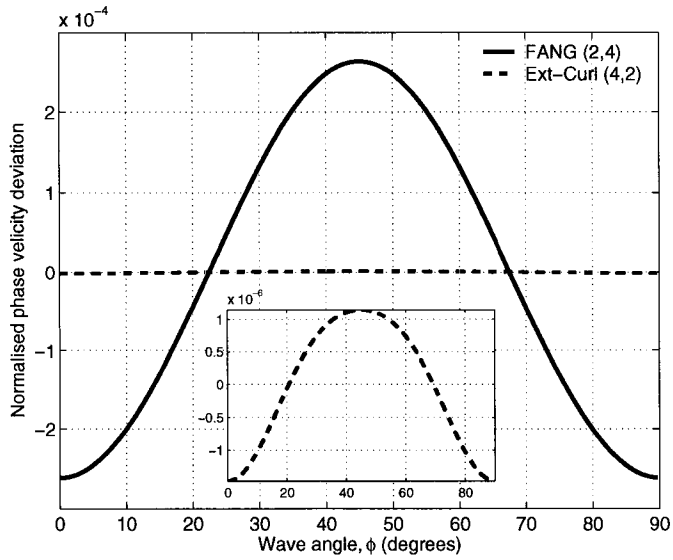

(a)

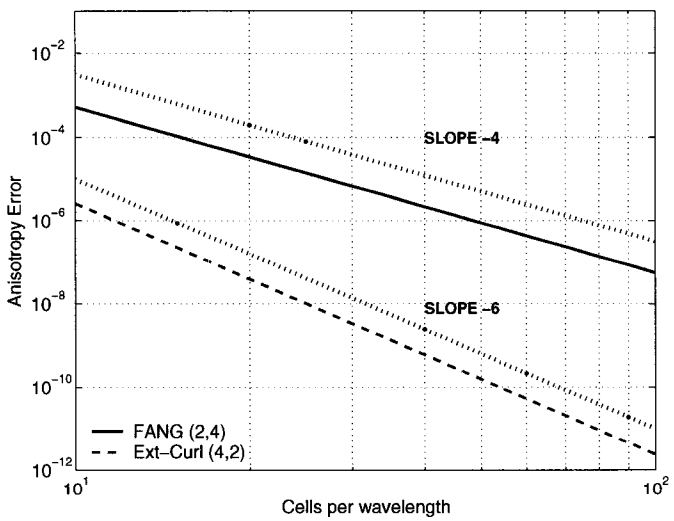

(b)

Fig. 5.7: (a) Normalized phase velocity deviation versus propagation angle at $N_\lambda = 10$. (b) Anisotropy error versus cells per wavelength.

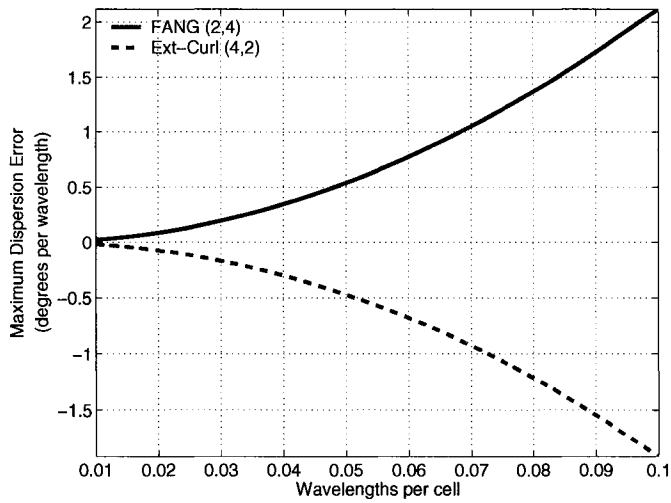

Fig. 5.8: Maximum algebraic dispersion error.

Fig. 5.9(a) the algebraic relative error is illustrated for the first 20 resonant frequencies as computed by the four schemes, against the corresponding analytic values. It is observed that the HOL-based as well as the Fang (2,4) scheme overestimate the resonances' values while the extended-curl (4,2) scheme underestimates them. This, as well as the overall performance of the schemes, are in perfect agreement with the theoretically expected behaviour demonstrated in Figs. 5.2 and 5.8. Finally, in Figs. 5.9(b),5.10(a) and (5.10(b)) there are the actual values of the predicted resonances for each of the schemes under study.

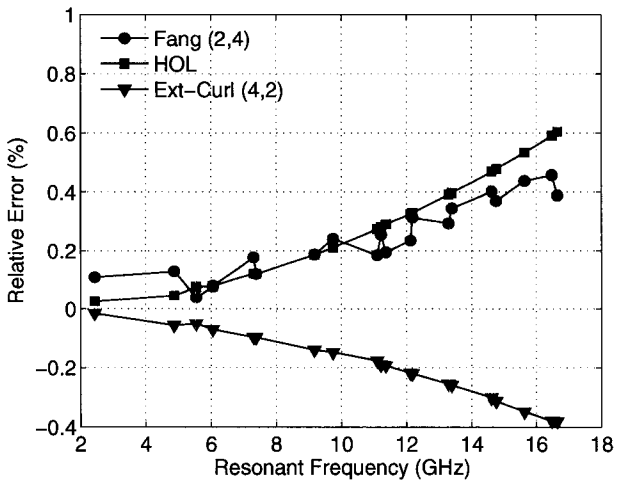

(a)

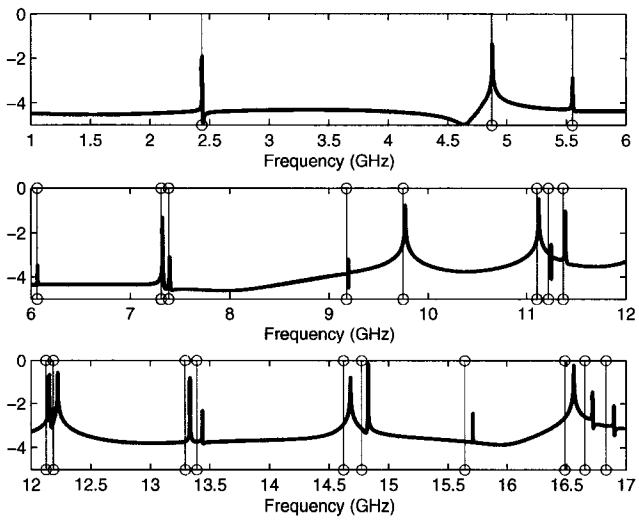

(b)

Fig. 5.9: (a) Resonant frequency prediction error. (b) 2-D cavity resonances computed by Fang (2,4).

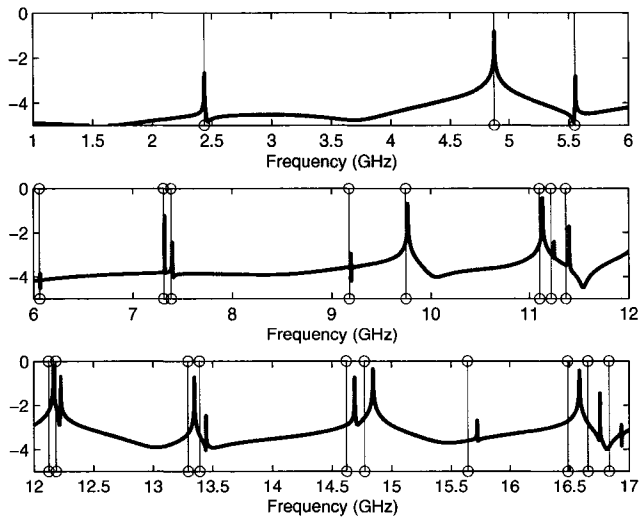

(a)

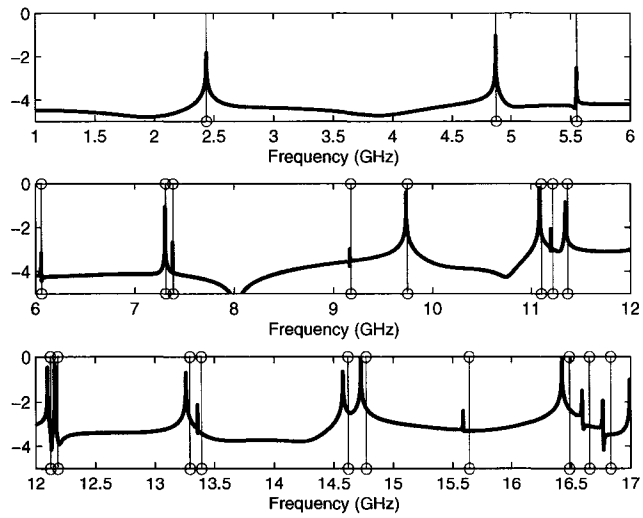

(b)

Fig. 5.10: (a) 2-D cavity resonances computed by HOL. (b) 2-D cavity resonances computed by extended-curl (4,2).

CHAPTER 6

PERFORMANCE OF EXTENDED CURL SCHEMES FOR A FIXED GRID RESOLUTION

6.1. Introduction

In this Chapter we examine the possibility of developing a high fidelity algorithm which allows the injection of arbitrary time-domain data into an FDTD grid. One well-known version of this problem is the implementation of a plane-wave source in an FDTD domain. This is achieved by utilizing what is usually referred to, in the FDTD literature, as the "total-scattered field formulation". According to this formulation, plane wave sources are created in FDTD by choosing a rectangular Huygens' box, where along its periphery the necessary Schelkunoff currents are imposed. Ideally, in the area surrounding the Huygen's box the field should be equal to zero, resulting in a perfect separation between the domain that the plane wave exists in, and the outside world. However, if one attempts to implement the above scenario using the Yee scheme, the ideally surrounding "quiet" area is contaminated by spurious reflections and non-physical field distribution, usually referred to as "leakage". This is primarily due to the mismatch between the numerical dispersion relation of FDTD, and the dispersion relation of the continuous free space that governs the analytically derived current sources. Obviously, it is expected that if a more accurate method is employed the leaking field will be minimized.

One approach to tackle this problem is to utilize a diakoptics-based technique a brief discussion of which is given in the following section. Its development is based on the derivation of a discrete Green's function that describes the response of an FDTD grid. An alternative approach which is the one pursued here is to design a dispersion-less FDTD scheme which essentially behaves like free space and hence any analytical time-domain data could be perfectly matched to it. Our quest for a dispersion-less FDTD scheme begins in Section 6.4.1 where a simple, rigorous and very accurate

methodology is described in order to achieve super-isotropy using a 2-D extended-curl scheme. Once this is done, elimination of dispersion can be trivially achieved by appropriately scaling the speed of light. Afterwards the above methodology is applied in a 3-D space. For both cases the appropriate dispersion analysis is performed which demonstrates the potential improvement in the extended curl schemes' performance.

6.2. A brief introduction to the diakoptics technique

The word "diakoptics" [1] stems from the Greek word "kopto" ($\kappa o \pi \tau \omega$) which means "to tear" and the preposition "dia" ($\delta \iota \alpha$) that reinforces the word to follow; in our case the following word may be interpreted as "system". Consequently, diakoptics is about system-tearing. The concept of diakoptics was first introduced by Kron as an alternative and more efficient method for the solution of differential equations arising in the study of large scale systems [40]. As a matter of fact Kron suggested that the partial differential equations that occur from the modeling of various physical phenomena may be solved numerically by employing a discretization technique different from the conventional finite-difference approximation of the unknown variables; his approach suggests that the solution domain can be represented by a discrete electric circuit model where its equivalent impedances and admittances are properly chosen. The great advantage of such representation is that the resulting equivalent circuit can be teared into smaller circuits (sub-sections) which allow a distributed solution of the corresponding differential equation and hence a reduction of the computational load. A schematic representation of this scenario is shown in Fig. 6.1. Such an approach can be implemented for any system (mechanical, electrical etc.) that can be represented with an equivalent network of distributed elements and it is usually refereed to as the tearing-and-interconnecting method. It has to be mentioned that the connectivity of the solutions of each sub-section is ensured

[1] A Greek translation could be "$\delta \iota \alpha \kappa o \pi \tau \iota \kappa \acute{\eta}$", from the noun "$\delta \iota \alpha \kappa \acute{o} \pi \tau \eta \varsigma$" which means "switch".

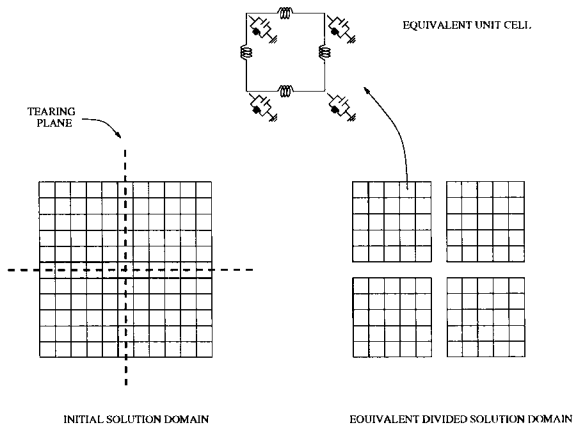

Fig. 6.1: Electric circuit equivalent of a solution domain.

by constructing additional sets of equations, which substitute the network branches that cross a tearing plane, based on the Lagrange multipliers theory. The tearing-and-interconnecting technique has been implemented in the context of Finite Elements [28] and has been shown to require less computational effort for the solution of the resulting system of equations.

6.3. Diakoptics implementation in the finite-difference time-domain method

As mentioned before the basic operational principle of diakoptics is to partition an electrically large circuit into several electrically smaller and simpler sub-sections whose characteristics can be obtained independently. These subsections are then connected together by using special interconnection methods. Typically there are two types of methods: *mode-to-mode* and *node-to-node* interconnection. The first one employs the mode-matching technique [41] therefore it has been solely used for the modeling of closed structures such as transmission lines and waveguides which are characterized by a discrete spectrum and furthermore the corresponding mode functions are usually known (for example trigonometric functions in the case of a rectangular waveguide). The second interconnection method requires the knowledge of the time response of certain discrete points-nodes along the connection interfaces. Although this method seems more advantageous, since it is independent

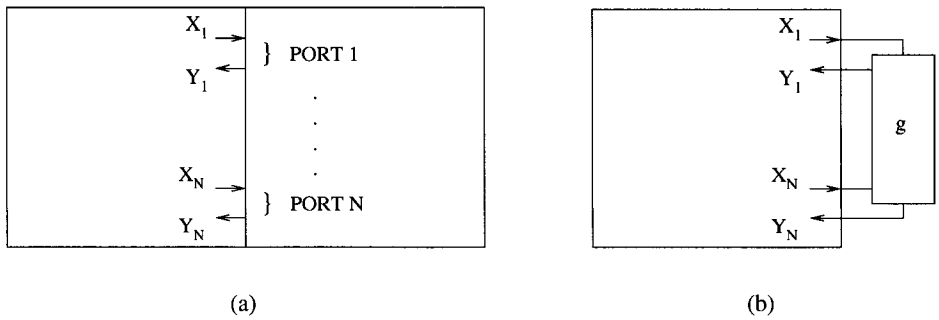

Fig. 6.2: Multiport networks. (a) Initial network configuration. (b) The second multiport network has been replaced by its equivalent impulse response.

of the mode function expression, it has been documented [42] that it is extremely memory consuming when it is applied to 2-D and 3-D problems. However this is not the case for 1-D problems where almost always FDTD modeling is very simple.

The time-domain diakoptics idea originates from linear system theory. The output $y[n]$ of an one-port linear system can be determined from the convolution between its impulse response $h[n]$ and its input $x[n]$. This means that the whole one-port linear system can be replaced by its impulse response. Similarly, a whole multi-port region of a system can be replaced by its corresponding impulse response matrix $\{g_{nm}[k]\}$ which in a sense can be considered as a discrete time-domain Green's function. With respect to Figs. 6.2(a) and 6.2(b) the multiport convolution is defined as:

$$y_m[k] = \sum_{n=1}^{N} \sum_{k'=1}^{k} g_{mn}\left[k - k'\right] x_n\left[k'\right] \tag{6.1}$$

where $g_{mn}\left[k\right]$ is the impulse response at port m, at time instant $t = k$ due to the unit excitation at port n at time instant $t = 0$.

6.3.1. A simple example

In this section we demonstrate how FDTD diakoptics can be implemented for the propagation of a TEM wave. Therefore, we consider a TEM plane wave, propagating along the z-axis consisting of

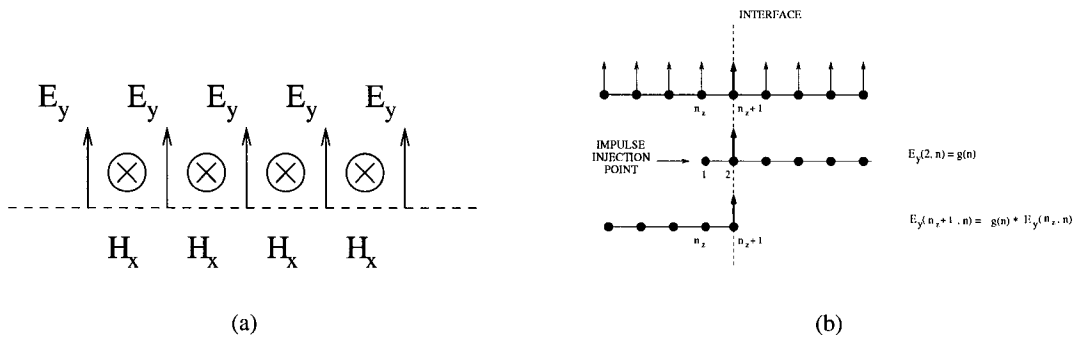

(a) (b)

Fig. 6.3: (a) Field components arrangement in the FDTD grid. (b) Implementation of FDTD diakoptics.

the field components E_y and H_x. The discretized electromagnetic field components arrangement, according to the Yee scheme, is shown in Fig. 6.3(a). Now, if we model the same phenomenon using FDTD diakoptics the following steps have to be followed:

1. Terminate the FDTD grid at node $n_z + 1$ so that the corresponding electric field component lies on the interface.

2. Calculate the impulse response of the right region.

3. Use the above impulse response to compute the E_y field component at $n_z + 1$ of the left part.

The above steps are shown schematically in Fig. 6.3(b). For the actual implementation of the above method some remarks have to be made:

- For the impulse response calculation of the right part an auxiliary cell is utilized on the left of the interface, where the impulse is injected. More precisely for the E_y component of this cell we have:

$$E_y = \begin{cases} 1, & n = 0 \\ 0, & n \neq 0 \end{cases} \tag{6.2}$$

- The time response of the electric field that lies on the interface is considered as the impulse response of the right part.

- The left part is updated using the standard FDTD update equations and the electric field component on the interface is computed using the convolution formula:

$$E_y\left[n_z+1,k\right]=\sum_{k'=1}^{n} g\left[k-k'\right]E_y\left[n_z,k'\right] \tag{6.3}$$

For validation purposes the propagation of a TEM wave was modeled using both the conventional and the diakoptics FDTD schemes and the results are shown in Figs. 6.4(a)-6.4(f). As can be seen the computational domain is 6 m long and it was excited by a Gaussian pulse originating at $z = 2$ m. The left boundary was terminated using an absorbing boundary condition while the right one was short-circuited. Notice that the diakoptics interface is located at $z = 3$ m. Six different snapshots are shown each one corresponding to time-step number 70, 90, 120, 250, 290 and 320 respectively. In each figure the upper subplot corresponds to the entire domain solution while the lower on to the diakoptics domain solution. It is apparent that both solutions are in excellent agreement.

6.4. Single frequency optimization of 2-D extended curl schemes

6.4.1. Formulation

For the purposes of this analysis we need to rewrite the spatial part of the numerical dispersion relation for the 2-D extended-curl scheme in a more appropriate form as follows. It is

$$\begin{aligned} R = &\left[\frac{1}{\Delta x}\sin\left(\frac{\tilde{k}_x\Delta x}{2}\right)\right]^2\left[\alpha+2\beta\cos\left(\tilde{k}_y\Delta y\right)\right]+\\ &+\left[\frac{1}{\Delta y}\sin\left(\frac{\tilde{k}_y\Delta y}{2}\right)\right]^2\left[\alpha+2\beta\cos\left(\tilde{k}_x\Delta x\right)\right] \end{aligned} \tag{6.4}$$

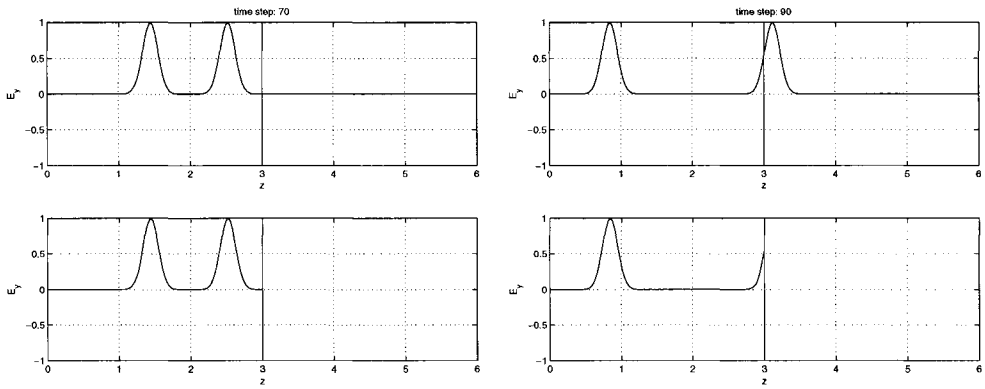

(a) time step 70 (b) time step 90

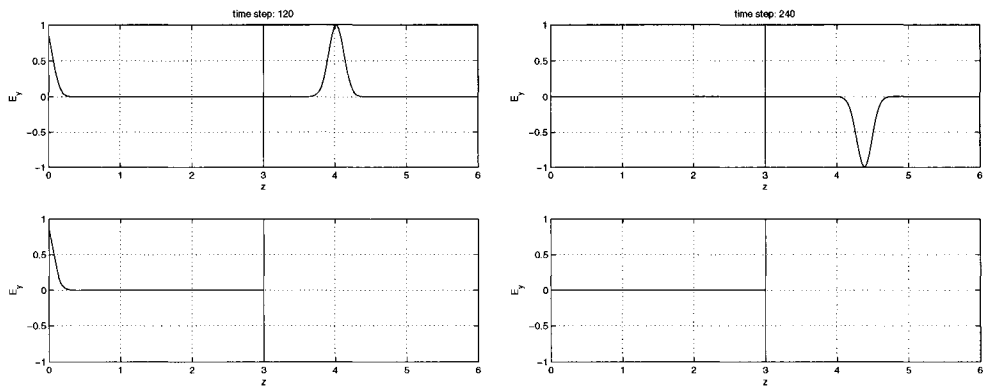

(c) time step 120 (d) time step 250

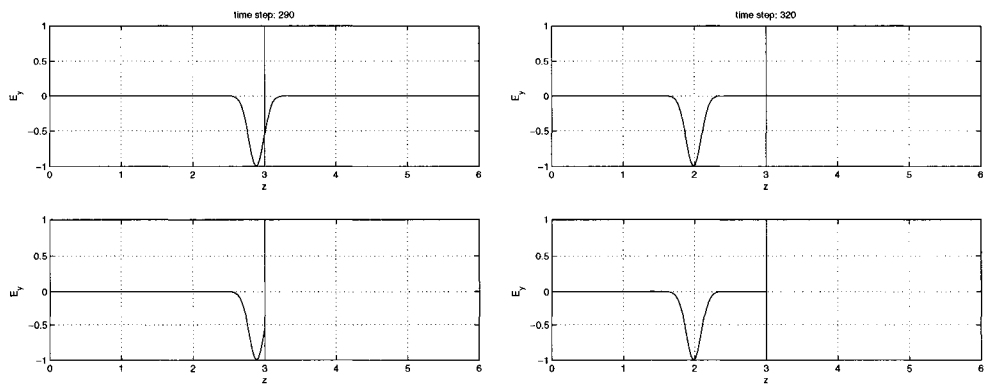

(e) time step 290 (f) time step 320

Fig. 6.4: FDTD solution vs. diakoptics FDTD solution.

We perform the polar coordinate transform $\left(\tilde{k}_x, \tilde{k}_y\right) = \tilde{k}\,(\cos\phi, \sin\phi)$, and assume a uniform discretization of a cell size h. After some straightforward algebra we obtain

$$R = \frac{1}{2h^2}\Big\{2\,(1-2\beta) + (4\beta-1)\left[\cos\left(\tilde{k}\,h\,\cos\phi\right) + \cos\left(\tilde{k}\,h\,\sin\phi\right)\right] - \\ - 4\beta\cos\left(\tilde{k}\,h\,\cos\phi\right)\cos\left(\tilde{k}\,h\,\sin\phi\right)\Big\} \tag{6.5}$$

Notice that we made use of the condition

$$\alpha + 2\beta = 1 \tag{6.6}$$

It is important to note that this condition is still valid throughout the following analysis, for the derivative approximation consistency reason that we described in Chapter 4. Also this condition is the backbone of the stability analysis for general 2-D extended-curl schemes presented in Chapter 3. Consequently, the corresponding results are directly applicable here.

Now, since R is a well-behaved function, it can be expanded in Fourier series with respect to the angle of propagation ϕ. Bearing this in mind we recall that the system

$$f_m(\phi) = \cos(m\,\phi), \quad m = 0, 1, \ldots \tag{6.7}$$

is orthogonal on the interval $[0, \pi]$ [43]. Although R is defined on the interval $[0, 2\,\pi]$ it can still be expanded with the respect to the above basis since $R(\phi) = R(\phi + \pi)$. Hence, R can be written as

$$R = \sum_{m=0}^{+\infty} a_m\, f_m(\phi) = a_0 + a_1\cos(\phi) + a_2\cos(2\,\phi) + \ldots \tag{6.8}$$

where the expansion coefficients are a function of $\tilde{k}\,h$ and β, or

$$a_m = a_m\left(\tilde{k}h, \beta\right) \tag{6.9}$$

The importance of the expansion in (6.8) is that if one sets the coefficients of the angle dependent terms equal to zero then the values of R can be made independent of the propagation angle, that is

perfectly isotropic. However this is an ideal scenario which is not realizable as will be demonstrated later. But what can be realized, which is very beneficial for practical applications, is to tune the expansion coefficients so that R varies slowly with respect to ϕ. In our case we are interested in single frequency problems, meaning that $\tilde{k}\,h$ is a constant, and hence the only available tuning degree of freedom is β.

So, let us first calculate the expansion coefficients. For their determination we make use of the following identities

$$\int_0^{\pi} \cos\left(x \sin\phi\right) \cos\left(m\phi\right) \mathrm{d}\phi = \left[1 + (-1)^m\right] \frac{\pi}{2} J_m(x) \tag{6.10}$$

$$\int_0^{\pi} \cos\left(x \cos\phi\right) \cos\left(m\phi\right) \mathrm{d}\phi = \cos\left(\frac{m\pi}{2}\right) \pi\, J_m(x) \tag{6.11}$$

and

$$\int_0^{\pi} \cos\left(x \sin\phi\right) \cos\left(x \cos\phi\right) \cos\left(m\phi\right) \mathrm{d}\phi = \cos\left(\frac{m\pi}{4}\right) \left[1 + (-1)^m\right] \frac{\pi}{2} J_m\left(x\sqrt{2}\right) \tag{6.12}$$

where $J_m(\cdot)$ is the m-th order Bessel function of the first kind. The first two integrals are listed in [44, pp. 441] while the derivation of the third one is straightforward by utilizing properties of the trigonometric and Bessel functions. Consequently, we have

$$\mathrm{R} = \frac{1}{2h^2}\left[2\,(1 - 2\beta) + \sum_{m=0}^{+\infty} a_m \cos\left(m\,\phi\right)\right] \tag{6.13}$$

where

$$\begin{aligned} a_m = (4\beta - 1) \left\{\left[1 + (-1)^m\right] \frac{\pi}{2} J_m\left(\tilde{k}\,h\right) + \cos\left(\frac{m\pi}{2}\right) \pi\, J_m\left(\tilde{k}\,h\right)\right\} - \\ - 4\beta \cos\left(\frac{m\pi}{4}\right) \left[1 + (-1)^m\right] \frac{\pi}{2} J_m\left(\tilde{k}\,h\sqrt{2}\right) \end{aligned} \tag{6.14}$$

For the behavior of a_m we make the following observations

$$\begin{aligned} a_m &= 0, \quad \text{if } m = 2\nu + 1,\ \nu \in \mathbb{Z}_+ \\ a_m &= 0, \quad \text{if } m = 2k \text{ and } k = 2\nu + 1,\ \nu \in \mathbb{Z}_+ \\ a_m &\neq 0 \quad \text{if } m = 2k \text{ and } k = 2\nu,\ \nu \in \mathbb{Z}_+ \end{aligned} \tag{6.15}$$

Hence the only non-zero coefficients are given by

$$a_{4\nu} = (4\beta - 1)\, 2\pi\, J_{4\nu}\left(\tilde{k}\, h\right) + (-1)^{\nu+1}\, 4\beta\pi\, J_{4\nu}\left(\tilde{k}\, h\sqrt{2}\right) \tag{6.16}$$

Therefore, R can be written in a Fourier series form as

$$R = \frac{1}{2h^2}\left[2\,(1 - 2\beta) + a_0 + a_4\cos(4\phi) + a_8\cos(8\phi) + \ldots\right] \tag{6.17}$$

Given the above expansion our goal is to minimize the coefficients corresponding to angle dependent terms, subject to the condition that the product $\tilde{k}\, h$ is a constant. First of all we observe that each of the above coefficients vanishes for a different value of β given by the solution of the following equation

$$a_{4\nu} = 0 \Rightarrow \underbrace{2\left[2\, J_{4\nu}\left(\tilde{k}\, h\right) + (-1)^{\nu+1}\, J_{4\nu}\left(\tilde{k}\, h\sqrt{2}\right)\right]}_{c_\nu}\beta = \underbrace{J_{4\nu}\left(\tilde{k}\, h\right)}_{d_\nu} \tag{6.18}$$

The above reveals that we cannot set the a_m coefficients equal to zero, simultaneously. Hence, an optimum β could be derived by employing a least square minimization approach. Hence if we define the following matrices $\mathbf{C} = [c_1\, c_2\, \ldots]^{\mathrm{T}}$ and $\mathbf{D} = [d_1\, d_2\, \ldots]^{\mathrm{T}}$ then according to the least square methodology, for a system of *linear* equations, β is given by

$$\beta = \frac{\mathbf{C}^{\mathrm{T}}\mathbf{D}}{\mathbf{C}^{\mathrm{T}}\mathbf{C}} \tag{6.19}$$

Our experimentation revealed that β converges to its final value by taking into account, in the minimization procedure, just the first two coefficients a_4 and a_8. As a matter of fact it turns out that for the computed beta, the values of the rest of the coefficients are negligible and they do not affect the minimization procedure. In Fig. 6.5 there is a graphic representation of β as a function of the grid resolution N_λ where we recall that $\tilde{k}\, h \sim N_\lambda^{-1}$.

Regarding to the behavior of β the following observations should be made. It can be seen that it is a monotonically decreasing function with an asymptote at $\beta = 1/12$. We recall that for $\beta = 1/12$

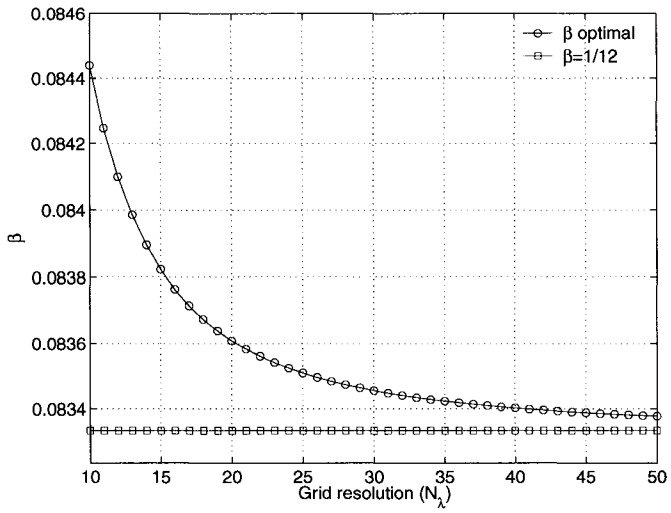

Fig. 6.5: Optimal β versus grid resolution $N_\lambda = \lambda/h$ (2-D case).

we retrieve the 4-th order isotropic extended-curl scheme that we described in Chapter 3. Therefore we can conclude that in order to obtain a fixed resolution isotropy optimization, it is required to perturb β as Fig. 6.5 dictates. Naturally this is translated as a perturbation of the isotropic Laplacian which is indirectly calculated during an FDTD time-step. In order to get a better insight of the above, let us Taylor expand R and set $\beta = \frac{1}{12} + \epsilon$. It is

$$\begin{aligned} R = & \frac{1}{4}\tilde{k}^2 - \frac{h^2}{48}\left\{1 + 3\epsilon\left[1 - \cos(4\phi)\right]\right\}k^4 + \\ & + \frac{h^4}{5760}\left\{\left[5 - \cos(4\phi)\right] + 30\epsilon\left[1 - \cos(4\phi)\right]\right\}k^6 + \mathcal{O}\left(h^6\right) \end{aligned} \tag{6.20}$$

It can be seen that the coefficients of the Taylor series have additional perturbation terms which contribution is controlled via the parameter ϵ. Apparently the existence of these terms plays a regulatory role that results in a super-isotropic behavior for a desired grid resolution. Note that R is not fourth order isotropic anymore. This implies that super-isotropy for a specific frequency, comes at the cost of a possible isotropy deterioration for other frequencies. This will be further demonstrated later in our analysis where the dispersion-anisotropy characteristics of the optimized scheme are examined.

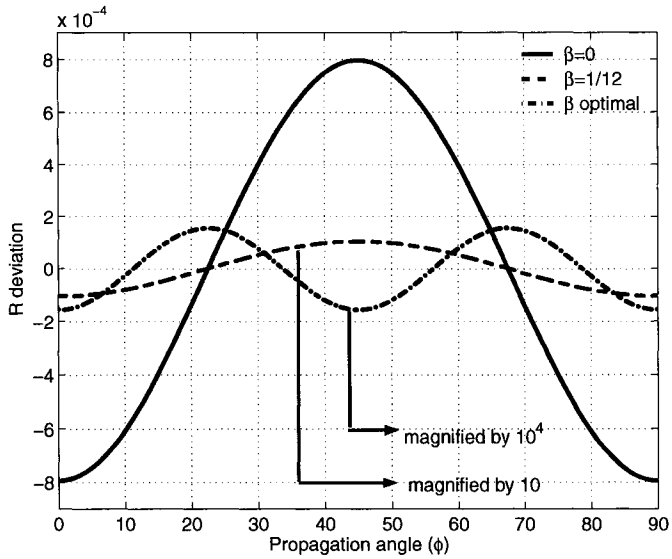

Fig. 6.6: Deviation of R with respect to its mean value versus angle of propagation ϕ. β optimal has been calculated for $\tilde{k}\,h = 2\,\pi/10$.

The effectiveness of the method presented so far is demonstrated in Fig. 6.6, where there are comparative plots of the R deviation, with respect to its mean value over all angles of propagation, for three different values of β. Note here that R corresponds to the spatial variation of the numerical dispersion relation and it should not be confused with the numerical phase velocity. Numerical phase velocity is a function of both the spatial and temporal dispersions and will be analyzed in the next paragraph. So, the solid line corresponds to the Yee scheme ($\beta = 0$), the dashed line is the fourth-order isotropic extended-curl scheme ($\beta = 1/12$), and the dash-dotted one corresponds to the optimized β. All three graphs have been computed for a grid resolution $\tilde{k}\,h = 2\,\pi/10$, where the optimal β is equal to 0.08443903506907. Notice that in order for the three graphs to be of the same order, and hence visually comparable, the values of R for $\beta = 1/12$, and the optimal β scheme had to be magnified by a factor of 10 and 10^4 respectively. This clearly indicates the significant improvement that has been achieved in the scheme's anisotropy behavior.

6.4.2. Stability and dispersion

For an actual FDTD simulation, given a desired grid resolution N_λ, an optimum value of β is determined. This requires an intermediate step which is that of the correspondence between N_λ and $\tilde{k}\,h$. These two quantities are related as:

$$\tilde{k}\,h \;=\; 2\,\arcsin\left[\frac{1}{S}\,\sin\left(\frac{\pi\,S}{N_\lambda}\right)\right] \tag{6.21}$$

The above relation creates an issue because for the general 2-D extended-curl scheme, the Courant stability limit is given by [Chapter 3]

$$S_{CL}\,(\beta) \;=\; \frac{1}{\sqrt{2\,(1\,-\,4\,\beta)}} \tag{6.22}$$

In other words the value of S_{CL} is determined by the value of β. However, according to (6.21) a Courant factor S has to be chosen in advance, in order to correspond N_λ to a $\tilde{k}\,h$. This may lead to a value for β which results in a Courant stability limit S_{CL}, less than S, and the scheme gets unstable.

Therefore, it is desirable to determine a Courant stability limit that guarantees stability regardless of the β value. Hence, from Fig. 6.5 we can see that the optimized values of β are greater than $1/12$. Therefore, given that (6.22) is monotonically increasing we have

$$\beta \geq \frac{1}{12} \;\Rightarrow\; S_{CL}\,(\beta) \geq S_{CL}\left(\frac{1}{12}\right) \;=\; \frac{\sqrt{3}}{2} \tag{6.23}$$

This implies that if we choose the Courant number in (6.21) equal to $S = \sqrt{3}/2$ then the resulting value of β will not lead to an unstable scheme. We recall that this is the Courant stability limit of the 4-th order isotropic extended-curl scheme, meaning that in terms of time-step size the two schemes are equally good.

The numerical dispersion relation for the frequency optimized scheme is the same as the one

for the general extended-curl schemes, that is

$$\left[\frac{1}{c\Delta t}\sin\left(\frac{\omega\Delta t}{2}\right)\right]^2 = \left[\frac{1}{\Delta x}\sin\left(\frac{\tilde{k}_x\Delta x}{2}\right)\right]^2\left[\alpha + 2\beta\cos\left(\tilde{k}_y\Delta y\right)\right] + \left[\frac{1}{\Delta y}\sin\left(\frac{\tilde{k}_y\Delta y}{2}\right)\right]^2\left[\alpha + 2\beta\cos\left(\tilde{k}_x\Delta x\right)\right] \tag{6.24}$$

Based on the above in Fig. 6.7(a) there is the phase velocity behavior versus angle of propagation for a grid resolution of $N_\lambda = 10$. The optimum value of β for this case was found to be equal to 0.08444861640266. It can be seen that the scheme exhibits highly isotropic phase velocity characteristics. In the inset figure there is a detailed illustration of the phase velocity deviation with respect to its mean value. It can be seen that the amplitude of the deviation ripple is of the order of 10^{-8}. This is 4 orders of magnitude less, than the $\beta = 1/12$ scheme. Moreover in Fig. 6.7(b) there is a plot of the maximum absolute phase error per wavelength versus grid resolution, defined as:

$$\psi = 360^\circ \max_{\phi}\left\{\left|1 - \frac{\tilde{v}_p}{c}\right|\right\} \tag{6.25}$$

It can be seen that the scheme is second order accurate since the slope is -2.

Additionally in Fig. 6.8 there are comparative plots of the anisotropy error versus grid resolution, defined as the difference between the maximum to the minimum value of $\tilde{v}_p$, relative to the speed of light c, for three different values of β. It can be seen that super-isotropy has been achieved for the desired grid resolutions, however the isotropy performance significantly deteriorates for higher grid resolutions.

From the above analysis we can conclude that in order to fully exploit the highly isotropic characteristics of the optimized scheme the scheme needs to be improved in terms of dispersion as well. This can be achieved by making the numerical wavevector equal to the exact along an appropriately chosen direction. If this condition is satisfied then the numerical phase velocity for this direction is equal to the speed of light. But due to the super-isotropic behavior of the numerical

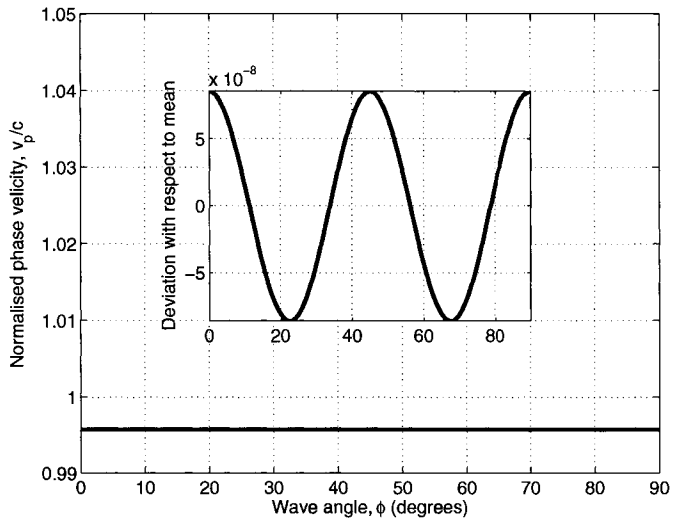

(a)

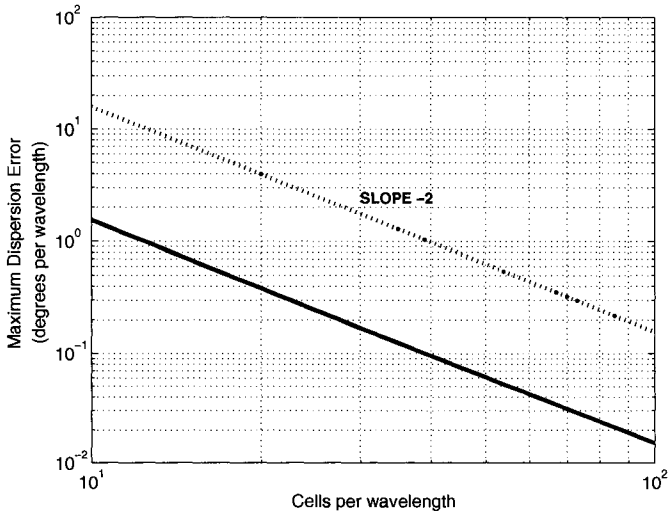

(b)

Fig. 6.7: (a) Normalized phase velocity versus angle of propagation ϕ, at $N_\lambda = 10$. (b) Maximum dispersion error.

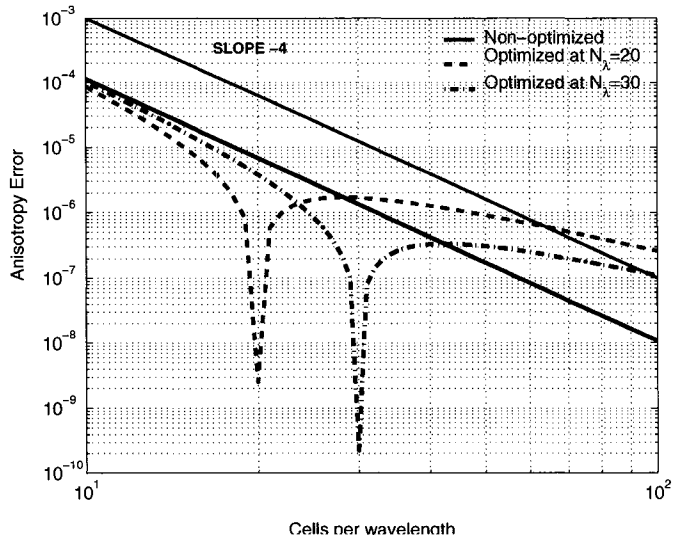

Fig. 6.8: Anisotropy error.

phase velocity, the latter will be equal to the speed of light at any other direction as well, up to the order of the anisotropy error. Hence, at $\phi = 0°$ (6.24) yields

$$\frac{1}{c\Delta t}\sin\left(\frac{\omega\Delta t}{2}\right) = \frac{1}{h}\sin\left(\frac{\tilde{k}\,h}{2}\right) \tag{6.26}$$

If we modify the above as

$$S\frac{\sin\left(\frac{k_0\,h}{2}\right)}{\sin\left(\frac{\omega_0\,\Delta t}{2}\right)}\frac{1}{c\Delta t}\sin\left(\frac{\omega\Delta t}{2}\right) = \frac{1}{h}\sin\left(\frac{\tilde{k}\,h}{2}\right) \tag{6.27}$$

then it is trivial to prove that

$$\omega = \omega_0 \Rightarrow \tilde{k} = k_0 \tag{6.28}$$

In others words this adjustment allows at a desired frequency ω_0, along the $\phi = 0°$ direction, the numerical wavevector to be equal to the exact one. Consequently, the scheme's numerical phase velocity will deviate from the speed of light at an order of the anisotropy error. This adjustment in the numerical dispersion relation can be justified either as a scaling of the free space material parameters or as a modified finite-difference operator which is usually referred to as non-standard

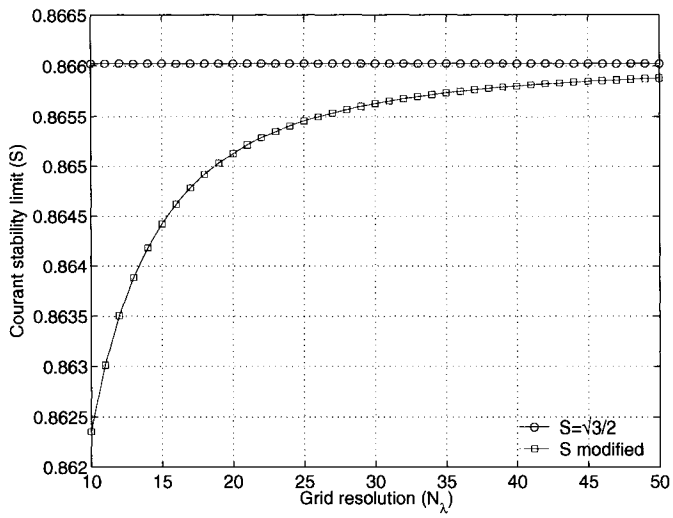

Fig. 6.9: Courant stability limit for the scaled scheme versus grid resolution N_λ. The calculation assumes $\beta = 1/12$.

finite-difference [45,46]. The first approach dictates to modify permittivity and permeability as

$$\widetilde{\varepsilon} = S \frac{\sin\left(\frac{k_0 h}{2}\right)}{\sin\left(\frac{\omega_0 \Delta t}{2}\right)} \varepsilon \quad \text{and} \quad \widetilde{\mu} = S \frac{\sin\left(\frac{k_0 h}{2}\right)}{\sin\left(\frac{\omega_0 \Delta t}{2}\right)} \mu \tag{6.29}$$

The second one suggests to replace the conventional spatial and temporal finite-difference operators with the following ones

$$\delta_x u_i = \frac{k_0}{2} \frac{u_{i+1/2} - u_{i-1/2}}{\sin\left(\frac{k_0 h}{2}\right)} \tag{6.30}$$

and

$$\delta_t u^n = \frac{\omega_0}{2} \frac{u^{n+1/2} - u^{n-1/2}}{\sin\left(\frac{\omega_0 \Delta t}{2}\right)} \tag{6.31}$$

The above operators essentially introduce frequency dependent spatial and temporal increments, that is

$$h \equiv \frac{2}{k_0} \sin\left(\frac{k_0 h}{2}\right) \quad \text{and} \quad \Delta t \equiv \frac{2}{\omega_0} \sin\left(\frac{\omega_0 \Delta t}{2}\right) \tag{6.32}$$

Both approaches have the same result which is the scaling of the speed of light as shown below

$$\widetilde{c} = \frac{\sin\left(\frac{\omega_0 \Delta t}{2}\right)}{S \sin\left(\frac{k_0 h}{2}\right)} c \tag{6.33}$$

The corresponding numerical dispersion relation is given by

$$\begin{aligned}\left[\frac{\sin\left(\frac{k_0 h}{2}\right)}{\sin\left(\frac{\omega_0 \Delta t}{2}\right)} \sin\left(\frac{\omega \Delta t}{2}\right)\right]^2 &= \sin^2\left(\frac{\tilde{k} h}{2} \cos\phi\right)\left[\alpha + 2\beta \cos\left(\tilde{k} h \sin\phi\right)\right] \\ &+ \sin^2\left(\frac{\tilde{k} h}{2} \sin\phi\right)\left[\alpha + 2\beta \cos\left(\tilde{k} h \cos\phi\right)\right]\end{aligned} \tag{6.34}$$

and after some straightforward manipulations it can be shown that the stability condition is given by

$$\Delta t \leq \frac{h}{c} \frac{N_\lambda}{\pi} \arcsin\left[\frac{\sin\left(\frac{\pi}{N_\lambda}\right)}{\sqrt{2\,(1 - 4\beta)}}\right] \tag{6.35}$$

where N_λ is the desired grid resolution to perform the optimization. The behavior of the above Courant stability limit versus grid resolution, for $\beta = 1/12$ is shown in Fig. 6.9. It can be seen that the maximum Courant number is monotonically increasing and has an asymptote at $S = \sqrt{3}/2$. It has to be mentioned that since the optimal values of β are greater than $1/12$ the stability limit can be slightly increased compared to the values shown in Fig. 6.9.

The performance of the scheme after the speed of light correction is demonstrated in Figs. 6.10(a) and 6.10(b). Specifically from Fig. 6.10(a) we can see that the same level of phase velocity variation has been retained as that of the non-scaled scheme [Fig. 6.7(a)], but its values have been shifted upwards around the speed of light as desired. Finally the improvement in the reduction of the maximum dispersion error is depicted in Fig. 6.10(b).

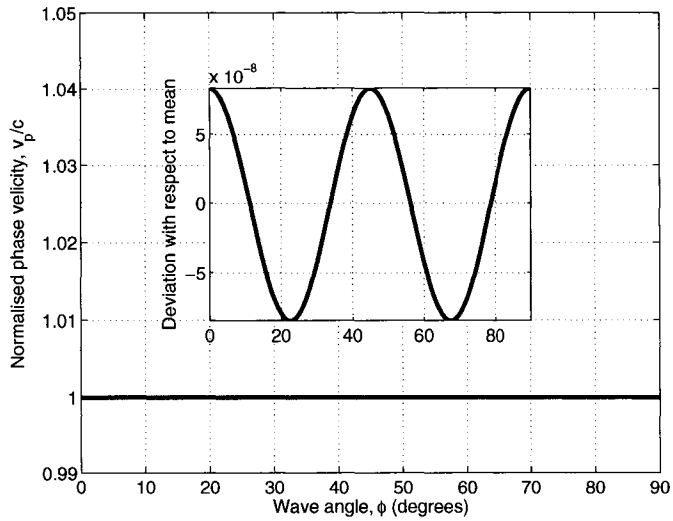

(a)

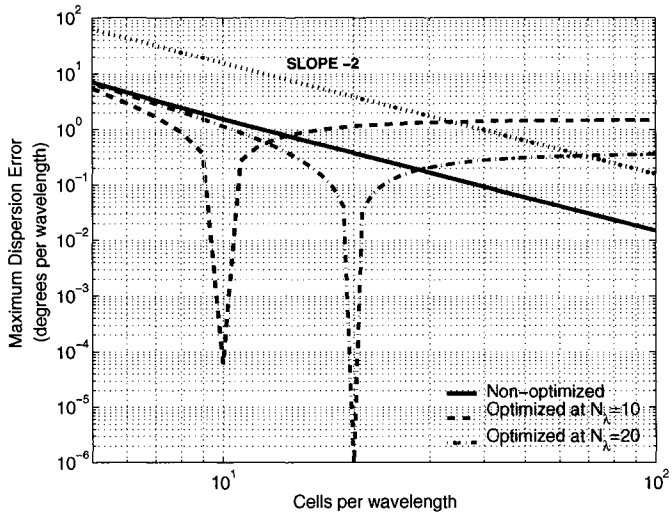

(b)

Fig. 6.10: (a) Normalized phase velocity versus angle of propagation ϕ, at $N_\lambda = 10$. (b) Maximum dispersion error.

6.5. Single frequency optimization of 3-D extended curl schemes

6.5.1. Formulation

In 3-D the optimization methodology parallels the 2-D one. Hence we begin from the spatial part of the numerical dispersion relation for the general 3-D extended curl scheme given by

$$\begin{aligned} R = & \left[\frac{1}{\Delta x}\sin\left(\frac{\tilde{k}_x\Delta x}{2}\right)\right]^2 \left[\alpha + 2\beta\cos\left(\tilde{k}_y\Delta y\right)\right]\left[\alpha + 2\beta\cos\left(\tilde{k}_z\Delta z\right)\right] \\ & + \left[\frac{1}{\Delta y}\sin\left(\frac{\tilde{k}_y\Delta y}{2}\right)\right]^2 \left[\alpha + 2\beta\cos\left(\tilde{k}_x\Delta x\right)\right]\left[\alpha + 2\beta\cos\left(\tilde{k}_z\Delta z\right)\right] \\ & + \left[\frac{1}{\Delta z}\sin\left(\frac{\tilde{k}_z\Delta z}{2}\right)\right]^2 \left[\alpha + 2\beta\cos\left(\tilde{k}_x\Delta x\right)\right]\left[\alpha + 2\beta\cos\left(\tilde{k}_y\Delta y\right)\right] \end{aligned} \tag{6.36}$$

where $\left(\tilde{k}_x, \tilde{k}_y, \tilde{k}_z\right) = k\ (\cos\phi\ \sin\theta, \sin\phi\ \sin\theta, \cos\theta)$. In principle R can be expanded in a series of spherical harmonics. Hence by following a procedure similar to the one described in the previous Section, isotropy improvement could be achieved. Unfortunately the involved integrals are extremely difficult to be computed in closed form (at least to the author's knowledge and ability). Therefore an alternative approach is attempted.

For brevity let us set $X = \cos\left(\tilde{k}_x\Delta x\right)$, $Y = \cos\left(\tilde{k}_y\Delta y\right)$, and $Z = \cos\left(\tilde{k}_z\Delta z\right)$. We rearrange R as a polynomial of β. It is

$$\begin{aligned} R = & 3\left[2 - 2\,(X + Y + Z) + 2\,(XY + XZ + YZ) - 2XYZ\right]\beta^2 + \\ & + \left[-6 + 4\,(X + Y + Z) - 2\,(XY + XZ + YZ)\right]\beta + \\ & + \frac{3}{2} - \frac{1}{2}(X + Y + Z) \end{aligned} \tag{6.37}$$

Now we assume that the 3-D space is sliced ϕ-wise according to a partition $\{\phi_j\}_1^N$. Hence for each ϕ_j, a plane is defined where R is dependent only on θ. Consequently by employing a procedure similar to the one described in the previous Section, for each one of these planes, a β can be calculated so that R is independent of θ. Therefore we will proceed as follows: for each ϕ_j we will

expand R with respect to θ and then we will obtain the optimum β via a least square approach which takes into account all ϕ_j. It is

$$R = \Big[6 + 3\sum_{m=0}^{\infty} A_m \cos(m\,\theta)\Big]\,\beta^2 + \\ + \Big[-6 + \sum_{m=0}^{\infty} B_m \cos(m\,\theta)\Big]\,\beta + \frac{3}{2} + \sum_{m=0}^{\infty} C_m \cos(m\,\theta) \tag{6.38}$$

where the expressions for A_m, B_m and C_m are shown in (6.39), (6.40) and (6.41). For a given ϕ_j the value of β for which the coefficients of the angle dependent expansion terms vanish,is given by

$$3\,A_m\,\beta^2 + B_m\,\beta + C_m = 0 \tag{6.47}$$

The above equation needs to be satisfied for all ϕ_j therefore we need to solve the following over-determined system of *non-linear* equations.

$$3\,\mathbf{A}\,\beta^2 + \mathbf{B}\,\beta + \mathbf{C} = \mathbf{0} \tag{6.48}$$

where

$$\mathbf{A} = \Big[\underbrace{A_1\,A_2\,\ldots}_{\phi_1}\Big|\ldots\Big|\underbrace{A_1\,A_2\,\ldots}_{\phi_j}\Big|\ldots\Big|\underbrace{A_1\,A_2\,\ldots}_{\phi_N}\Big]^{\mathrm{T}} \tag{6.49}$$

Matrices $\mathbf{B}$ and $\mathbf{C}$ are created in the same manner. In this case the value of β is obtained with successive approximations. We define

$$f_m(\beta) = 3\,A_m\,\beta^2 + B_m\,\beta + C_m \tag{6.50}$$

Given an initial guess β^0, then the perturbed value $f_m\left(\beta^0 + \Delta\beta\right)$ is approximated as

$$f_m\left(\beta^0 + \Delta\beta\right) \approx f_m\left(\beta^0\right) + f'_m\left(\beta^0\right)\Delta\beta = 0 \tag{6.51}$$

Hence by including all the available information, $\Delta\beta$ is given by

$$\mathbf{f}\left(\beta^0\right) + \mathbf{f}'\left(\beta^0\right)\Delta\beta = \mathbf{0} \Rightarrow \Delta\beta = -\frac{\mathbf{f}^{\mathrm{T}}\left(\beta^0\right)\mathbf{f}\left(\beta^0\right)}{\mathbf{f}^{\mathrm{T}}\left(\beta^0\right)\mathbf{f}'\left(\beta^0\right)} \tag{6.52}$$

$$A_m =$$
$$= -2\left\{ [1+(-1)^m]\,\frac{\pi}{2}\left[J_m\left(\tilde{k}\,h\,\cos\phi\right) + J_m\left(\tilde{k}\,h\,\sin\phi\right)\right] + \cos\left(\frac{m\pi}{2}\right)\pi\,J_m\left(\tilde{k}\,h\right)\right\} +$$
$$+ 2\,[1+(-1)^m]\,\frac{\pi}{4}\times$$
$$\times\left\{ \left[J_m\left(\tilde{k}\,h\,\rho_1\right) + J_m\left(\tilde{k}\,h\,\rho_2\right)\right] + 2\cos(m\theta_s)\,J_m\left(\tilde{k}\,h\,\rho_s\right) + 2\cos(m\theta_c)\,J_m\left(\tilde{k}\,h\,\rho_c\right)\right\} -$$
$$- 2\,[1+(-1)^m]\,\frac{\pi}{4}\left[\cos(m\theta_3)\,J_m\left(\tilde{k}\,h\,\rho_3\right) + \cos(m\theta_4)\,J_m\left(\tilde{k}\,h\,\rho_4\right)\right] \tag{6.39}$$

$$B_m =$$
$$= 4\left\{ [1+(-1)^m]\,\frac{\pi}{2}\left[J_m\left(\tilde{k}\,h\,\cos\phi\right) + J_m\left(\tilde{k}\,h\,\sin\phi\right)\right] + \cos\left(\frac{m\pi}{2}\right)\pi\,J_m\left(\tilde{k}\,h\right)\right\} -$$
$$- 2\,[1+(-1)^m]\,\frac{\pi}{4}\times$$
$$\times\left\{ \left[J_m\left(\tilde{k}\,h\,\rho_1\right) + J_m\left(\tilde{k}\,h\,\rho_2\right)\right] + 2\cos(m\theta_s)\,J_m\left(\tilde{k}\,h\,\rho_s\right) + 2\cos(m\theta_c)\,J_m\left(\tilde{k}\,h\,\rho_c\right)\right\} \tag{6.40}$$

$$C_m =$$
$$= -\frac{1}{2}\left\{ [1+(-1)^m]\,\frac{\pi}{2}\left[J_m\left(\tilde{k}\,h\,\cos\phi\right) + J_m\left(\tilde{k}\,h\,\sin\phi\right)\right] + \cos\left(\frac{m\pi}{2}\right)\pi\,J_m\left(\tilde{k}\,h\right)\right\} \tag{6.41}$$

$$\rho_1 = \sin\phi + \cos\phi \qquad \rho_2 = -\sin\phi + \cos\phi \tag{6.42}$$

$$\rho_c = \sqrt{1+\cos^2\phi} \qquad \rho_s = \sqrt{1+\sin^2\phi} \tag{6.43}$$

$$\rho_3 = \sqrt{1+\rho_1^2} \qquad \rho_4 = \sqrt{1+\rho_2^2} \tag{6.44}$$

$$\tan\theta_s = \frac{1}{\sin\phi} \qquad \tan\theta_c = \frac{1}{\cos\phi} \tag{6.45}$$

$$\tan\theta_3 = \frac{1}{\rho_1} \qquad \tan\theta_4 = \frac{1}{\rho_2} \tag{6.46}$$

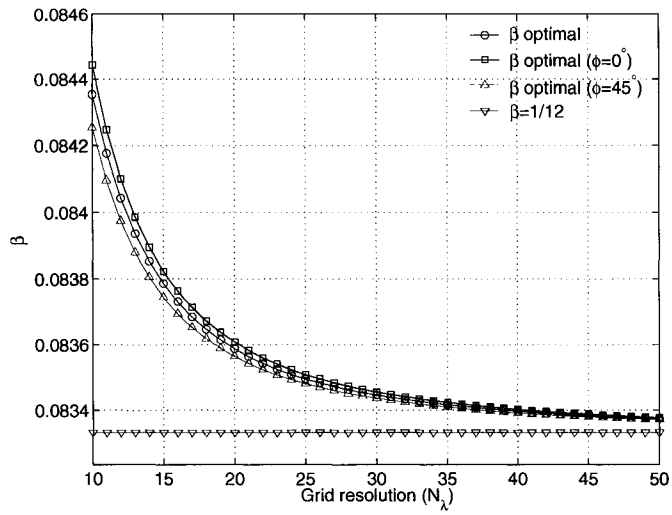

Fig. 6.11: Optimal β versus grid resolution $N_\lambda = \lambda/h$ (3-D case).

A new estimate for β is defined as

$$\beta^1 = \beta^0 + \Delta\beta \tag{6.53}$$

The previous procedure is repeated until some convergence criterion is satisfied. In Fig. 6.11 there are the optimum values of β versus grid resolution. Also there are the optimum values of β calculated for the $\phi = 0°$ and the $\phi = 45°$ planes, individually. It can be seen that especially for low grid resolutions there is a significant difference between the β values for the two planes. This implies that the value of β that achieves angle independence over the one plane, it does not certify the same over the other. Therefore the overall optimum β is expected to improve isotropy at an average sense and consequently super-isotropy cannot be achieved, as in the 2-D case. More precisely in Figs. 6.12(a) and 6.12(b) there are the R variations over the $\phi = 0°$ and the $\phi = 45°$ planes for different values of β. It can be seen that for the optimal β, R behaves overall more isotropically, however this improvement is only in the order of 10 for the reasons described previously.

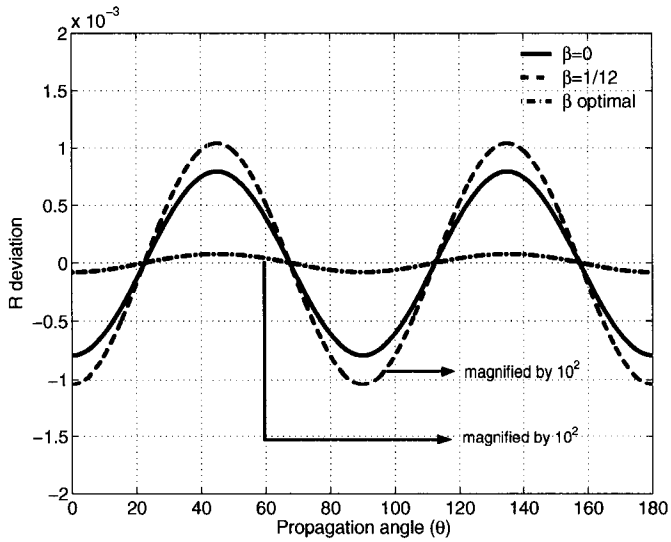

(a) $\phi = 0°$.

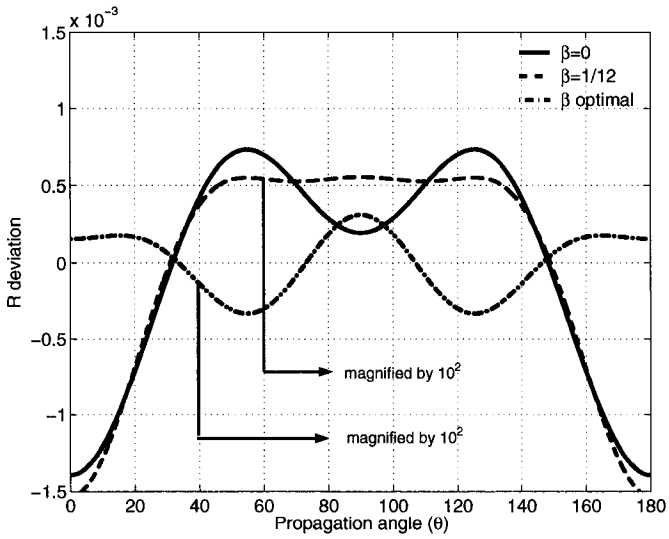

(b) $\phi = 45°$.

Fig. 6.12: Deviation of R with respect to its mean value versus angle of propagation θ. β optimal has been calculated for $\tilde{k}\,h = 2\,\pi/10$.

6.5.2. Stability and dispersion analysis

The stability and dispersion analysis for the 3-D case is similar to the 2-D one with the only difference being that the general Courant stability limit is given by [Chapter 4]

$$S_{CL} = \frac{1}{\sqrt{3}|1 - 4\beta|} \tag{6.54}$$

Similarly the speed of light scaling procedure is directly applicable here. For completeness the modified numerical dispersion relation is given below

$$\left[\frac{\sin\left(\frac{k_0 h}{2}\right)}{\sin\left(\frac{\omega_0 \Delta t}{2}\right)} \sin\left(\frac{\omega \Delta t}{2}\right)\right]^2 = \tag{6.55}$$

$$\begin{aligned}
&= \sin^2\left(\frac{\tilde{k}h\cos\phi\sin\theta}{2}\right)\left[\alpha + 2\beta\cos\left(\tilde{k}h\sin\phi\sin\theta\right)\right]\left[\alpha + 2\beta\cos\left(\tilde{k}h\cos\theta\right)\right] \\
&+ \sin^2\left(\frac{\tilde{k}h\sin\phi\sin\theta}{2}\right)\left[\alpha + 2\beta\cos\left(\tilde{k}h\cos\phi\sin\theta\right)\right]\left[\alpha + 2\beta\cos\left(\tilde{k}h\cos\theta\right)\right] \\
&+ \sin^2\left(\frac{\tilde{k}h\cos\theta}{2}\right)\left[\alpha + 2\beta\cos\left(\tilde{k}h\cos\phi\sin\theta\right)\right]\left[\alpha + 2\beta\cos\left(\tilde{k}h\sin\phi\sin\theta\right)\right]
\end{aligned} \tag{6.56}$$

and the corresponding stability limit can be easily shown to be the following

$$\Delta t \leq \frac{h}{c}\frac{N_\lambda}{\pi}\arcsin\left[\frac{\sin\left(\frac{\pi}{N_\lambda}\right)}{\sqrt{3}\,(1 - 4\beta)}\right] \tag{6.57}$$

Moreover, in Fig. 6.13(a) there are comparative plots of the anisotropy error versus grid resolution. It can be seen that for the optimized β, the error curves exhibit shallow nulls, almost three orders of magnitude more that the corresponding 2-D ones. This has a direct impact on the dispersion error performance. As shown in Fig. 6.13(b) for the optimized grid resolutions the dispersion error has been reduced but not as significantly as in the 2-D case.

6.6. Numerical examples

In this section numerical results are presented to support the previously analysis. We examine the propagation of a monochromatic plane wave in an FDTD domain. For this experiment, a 130 $\times$

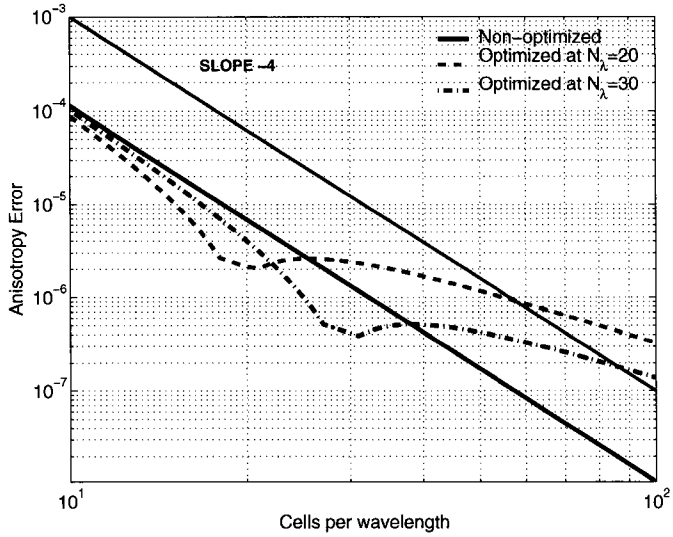

(a)

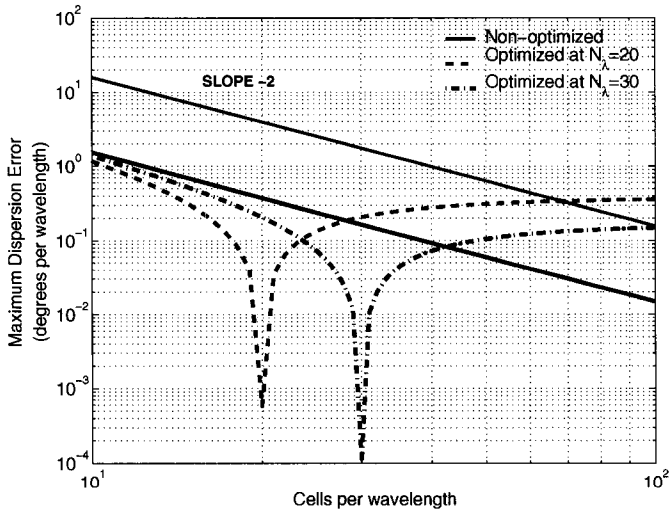

(b)

Fig. 6.13: (a) Anisotropy error. (b) Maximum dispersion error.

130 cells domain is chosen where the cell size is $h = \lambda/30$. The Huygens' box is placed within 20-cells from the computational domain boundary, and the latter is surrounded by a 12-cell thick perfectly matched layer. A monochromatic TEM (E_y, H_z) plane wave is generated, propagating along the $\phi = 0°$ direction.

Two different cases were compared, namely: $\beta = 1/12$ and β optimized at $N_\lambda = 30$. For both case the speed of light was adjusted, however the adjustment was made with respect to the wavevector along the $\phi = 45°$ direction, given by

$$\tilde{k} = \frac{2\sqrt{2}}{h} \arcsin \sqrt{\frac{1 \pm \sqrt{1 - 16\beta \left[\frac{1}{S\sqrt{2}} \sin\left(\frac{\pi S}{N_\lambda}\right)\right]}}{8\beta}} \tag{6.58}$$

We let the plane wave propagate for a sufficient number of time-steps and then a discrete Fourier transform was performed to extract its magnitude and phase. These quantities were compared to the corresponding analytical ones and the results are shown in Figs. 6.14(a)-6.15(b). The superiority of the optimized scheme is apparent where we can see that the phase error had been decreased by two orders of magnitude and the magnitude variations are constant throughout the injection area.

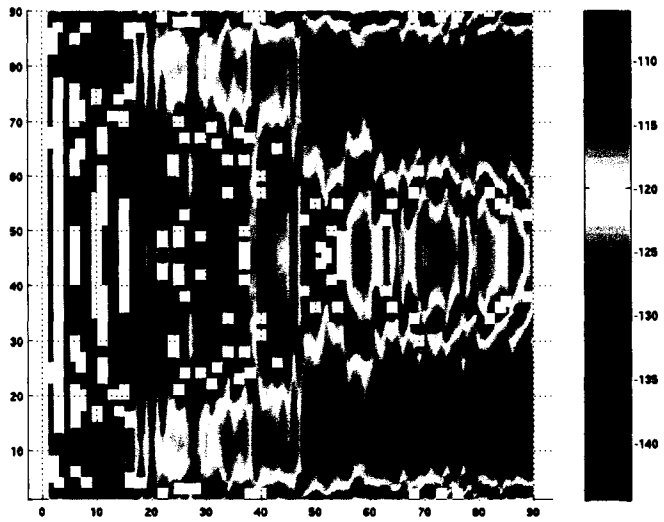

(a) Magnitude.

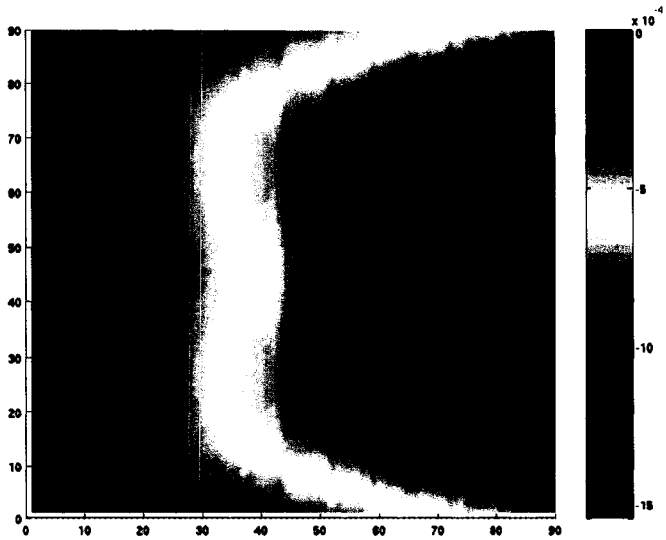

(b) Phase.

Fig. 6.14: Plane wave injection error, $\beta = 1.12$.

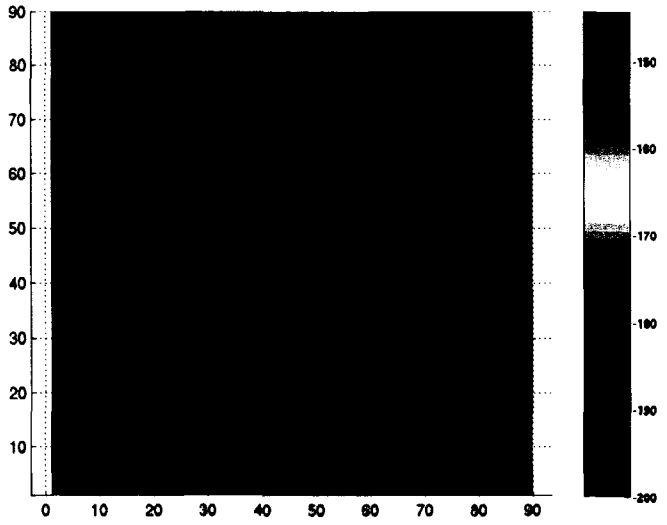

(a) Magnitude.

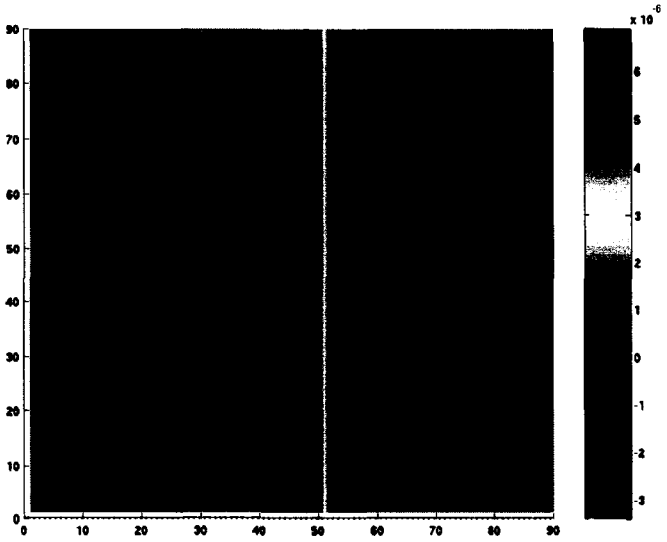

(b) Phase.

Fig. 6.15: Plane wave injection error, β optimized at $N_\lambda = 30$.

CHAPTER 7

CONCLUSIONS AND FUTURE WORK

We have described a general framework for the design of stable FDTD schemes with improved approximations of the transverse Laplacian term associated with the curl-curl operator. Depending on the Laplacian approximation the resulting scheme can be more isotropic, less dispersive and have a higher Courant number than the conventional Yee algorithm and many of its improvements found in the literature. Representative numerical experiments were performed that verified the theoretically expected behavior.

There are two main points that should be emphasized with respect to this work. First, this development of an improved extended transverse curl should not be confused with higher order approximations of the individual partial derivatives involved in the curl (as in (2,4) schemes). Such approaches extend the FDTD stencil linearly in the direction of the derivative, risking the acquisition of superluminal information in order to better approximate the derivative. The 9-point extended curl here minimizes the amount of superluminal information acquired since, as shown in Chapter 3, the extra terms can be seem as mapping unto the corners of the cell in question. Thus the increased isotropy is gained at no expense to the dispersion. In fact dispersion is reduced overall in the sense that the Courant number can be increased if desired all the way to one and still stability is preserved. A higher Courant number implies a more efficient computational space since to every frequency available via a Fourier transform of the time history corresponds a real wavenumber. To see this consider conventional 2D FDTD with Courant number $S = 0.707$ so that $\Delta t = 0.707\, h/c$. The limit radian frequency of the Fourier Transform is $\omega_{lim} = \pi/\Delta t$ which might lead us to believe that we can see wavenumbers as high $\omega_{lim}/c = \pi\, c/(0.707\, h\, c) = 1.414\, \pi/h$. The reality is that the discrete nature of h limits the highest possible wavenumber in our space to π/h. Therefore the

frequency domain spectrum between $\pi/\Delta t$ and $0.707\,\pi/\Delta t$ is really wasted since it can never be sampled in our discretized space. A Courant number of one makes the limit frequency and the limit wavenumber of the discretized space time of FDTD match, wasting nothing.

Second, the consequences of improving the Laplacian cannot be over emphasized. Although most FDTD practitioners are used to living with the dispersion problems of FDTD, it can be seen that the real problem is not dispersion itself but the anisotropy of that dispersion. If, as we show here, the anisotropy of FDTD can be virtually eliminated (the extended curl renders the scheme fourth order accurate in isotropy) then frequency domain dispersion can be readily dealt with by other means. That is, since in the extended curl all waves in all directions suffer from the same dispersion, a simple algebraic dispersion correction [2], works globally to render all the results of a time harmonic steady state FDTD run virtually indistinguishable from a frequency domain solution in the same space. The implications are wide ranging. For instance, the injection of time harmonic plane wave fields into FDTD domains now becomes simply an exercise in correct mapping of the equivalent currents from the frequency domain continuum into the discretized world of FDTD.

This work provided a comprehensive study of the FDTD method as applied to Maxwell's equations. Although many aspects of the method were explored, several useful conclusions were drawn and many interesting improvements were suggested, there are a lot of things that need to be further examined. First of all an elegant solution for the treatment of PEC boundaries is highly desired. Image theory does provide a remedy, however it is hard to program when arbitrary geometries need to be modeled, and in principle it is not accurate when finite domains are involved. In addition, the behavior of the extended curl operator along material interfaces should be examined to ensure accurate material modeling.

Another challenging task is to combine extended curl schemes with higher order time integrators. The Runge-Kuta scheme is an option however it introduces artificial dissipation and hence one

has to resort to very small time-steps. One very interesting and promising technique is symplectic integrators [47,48] since they provide higher order accuracy and they are non-dissipative, since they are based on the modeling of a Hamiltonian system.

Finally, it would be of great interest to achieve wideband optimization of FDTD schemes. A trivial approach to this would be to attempt a multi-objective optimization of the numerical dispersion relation. A more radical and revolutionary approach would be to attempt a time-frequency discretization for Maxwell's equations. Such methods are very common in signal processing and allow for a more compact represtation of time-varying signals.

REFERENCES

[1] K. S. Yee, "Numerical solution of initial boundary value problems involving Maxwell's equations in isotropic media," *IEEE Trans. Antennas Propagat.*, vol. 14, no. 8, pp. 302–307, May 1966.

[2] A. T. Taflove and S. C. Hagness, *Computational Electrodynamics: The Finite-Difference Time-Domain Method*, 2nd ed. Artech House, 2000.

[3] J. Fang, "Time domain finite difference computation for Maxwell's equations," Ph.D. dissertation, University of California at Berkeley, Berkeley, CA, 1989.

[4] A. Yefet and P. G. Petropoulos, "A staggered fourth-order accurate explicit finite difference scheme for the time-domain Maxwell's equations," *Journal of Computational Physics*, vol. 168, no. 2, pp. 286–315, 2001.

[5] T. T. Zygiridis and T. D. Tsiboukis, "Low-dispersion algorithms based on the higher order (2,4) FDTD method," *IEEE Trans. Microwave Theory Tech.*, vol. 52, no. 4, pp. 1321–1327, Apr. 2004.

[6] G. Sun and C. W. Trueman, "Optimized finite-difference time-domain methods based on the (2,4) stencil," *IEEE Trans. Microwave Theory Tech.*, vol. 53, no. 3, pp. 832–842, Mar. 2005.

[7] M. F. Hadi and M. Piket-May, "A modified FDTD (2,4) scheme for modeling electrically large structures with high-phase accuracy," *IEEE Trans. Antennas Propagat.*, vol. 45, Feb. 1997.

[8] J. L. Young, D. Gaitonde, and J. S. Shang, "Toward the construction of a fourth-order difference scheme for transient EM wave simulation: staggered grid approach," *IEEE Trans. Antennas Propagat.*, vol. 45, no. 11, 1997.

[9] S. K. Lele, "Compact finite difference schemes with spectral resolution," *J. Comput. Phys.*, vol. 101, pp. 16–42, 1992.

[10] Y. Liu, "Fourier analysis of numerical algorithms for the Maxwell equations," *J. Comput. Phys.*, vol. 124, pp. 396–416, 1996.

[11] F. Xiao, X. Tang, and X. Zhang, "The construction of low-dispersive FDTD on hexagon," *IEEE Trans. Antennas Propagat.*, vol. 53, no. 11, pp. 3697–3703, Nov. 2005.

[12] J. S. Juntunen and T. D. Tsiboukis, "Reduction of numerical dispersion in FDTD method through artificial anisotropy," *IEEE Trans. Microwave Theory Tech.*, vol. 48, no. 4, pp. 582–588, Apr. 2000.

[13] S. Wang and F. L. Teixeira, "A finite-difference time-domain algorithm optimized for arbitrary propagation angles," *IEEE Trans. Antennas Propagat.*, vol. 51, no. 9, pp. 2456–2463, Sept. 2003.

[14] ——, "Dispersion-relation-preserving FDTD algorithms for large-scale three-dimensional problems," *IEEE Trans. Antennas Propagat.*, vol. 51, no. 8, 2003.

[15] ——, "A three-dimensional angle-optimized finite-difference time-domain algorithm," *IEEE Trans. Microwave Theory Tech.*, vol. 51, no. 3, 2003.

[16] ——, "Grid-dispersion error reduction for broadband FDTD electromagnetic simulations," *IEEE Trans. Magn.*, vol. 40, no. 2, 2004.

[17] ——, "Lattice models for large-scale simulations of coherent wave scattering," *Phys. Rev. E*, vol. 69, 2004.

[18] K. L. Shlager and J. B. Schneider, "Comparison of the dispersion properties of several low-dispersion finite-difference time-domain algorithms," *IEEE Trans. Antennas Propagat.*, vol. 51, no. 3, pp. 642–653, Mar. 2003.

[19] B. Finkelstein and R. Kastner, "Finite difference time domain dispersion reduction schemes," *J. Comput. Phys.*, 2006, doi:10.1016/j.jcp.2006.06.016.

[20] J. S. Hesthaven, "High-order accurate methods in time-domain computational electromagnetics: a review," *Advances in Imaging and Electron Physics*, vol. 127, 2003.

[21] G. Cohen, "A class of schemes, fourth order in space and time, for the 2D wave equation," in *Proc. 6th IMACS Intenat. Symp. on Computer Methods for Partial Differential Equations*, Bethlehem, PA, USA, June 1987, pp. 23–27.

[22] G. Mur, "Absorbing boundary conditions for the finite-difference approximation of the time-domain electromagnetic-field equations," *IEEE Trans. Electromagn. Compat.*, vol. 23, no. 4, pp. 377–382, 1981.

[23] J.-P. Bérenger, "A perfectly matched layer for the absorption of electromagnetic waves," *J. Comput. Phys.*, vol. 114, no. 1, pp. 185–200, 1994.

[24] ——, "Perfectly matched layer for the FDTD solution of wave-structure interaction problems," *IEEE Trans. Antennas Propagat.*, vol. 44, no. 1, pp. 110–117, 1996.

[25] ——, "Three-dimensional perfectly matched layer for the absorption of electromagnetic waves," *J. Comput. Phys.*, vol. 127, pp. 363–379, 1996.

[26] Z. S. Sacks, D. M. Kingsland, R. Lee, and J. Lee, "A perfectly matched anisotropic absorber for use as an absorbing boundary condition," *IEEE Trans. Antennas Propagat.*, vol. 43, no. 12, pp. 1460–1463, Dec. 1995.

[27] L. Zhao and A. C. Cangellaris, "GT-PML: Generalized theory of perfectly matched layers and its application to the reflectionless truncation of finite-difference time-domain grids," *IEEE Trans. Microwave Theory Tech.*, vol. 44, no. 12, pp. 2555–2563, 1996.

[28] S. D. Gedney, "An anisotropic PML absorbing media for the FDTD simulation of fields in lossy and dispersive media," *IEEE Trans. Antennas Propagat.*, vol. 16, pp. 399–415, 1996.

[29] K. S. Kunz and R. J. Luebbers, *The Finite Difference Time Domain Method for Electromagnetics.* CRC Press, 1993.

[30] M. Patra and M. Karttunen, "Stencils with isotropic discretization error for differential operators," *Numerical Methods for Partial Differential Equations*, vol. 22, no. 4, pp. 936–953, July 2006.

[31] G. H. Cohen, *Higher-order numerical methods for transient wave equations.* Germany: Springer, 2002.

[32] M. S. Min and C. H. Teng, "The instability of the Yee scheme for the magic time step," *J. Comput. Phys.*, vol. 166, pp. 418–424, 2001.

[33] S. L. Ray, "Grid decoupling in finite element solutions of Maxwell's equations," *IEEE Trans. Antennas Propagat.*, vol. 40, no. 4, pp. 443–445, Apr. 1992.

[34] E. A. Forgy and W. C. Chew, "A time-domain method with isotropic dispersion and increased stability on an overlapped lattice," *IEEE Trans. Antennas Propagat.*, vol. 50, no. 7, pp. 983–996, July 2002.

[35] M. Celuch-Marcysiak and W. K. Gwarek, "On the nature of solutions produced by finite difference schemes in the time domain," *Int. J. Numer. Model.*, vol. 12, pp. 23–40, 1999.

[36] R. F. Harrington, *Time-Harmonic Electromagnetic Fields.* New York: Wiley-Interscience, 2001.

[37] L. Collatz, *The numerical treatment of differential equations*, 3rd ed. Springer-Verlag, 1966.

[38] A. H. Panaretos, J. T. Aberle, and R. E. Díaz, "The effect of the 2-D Laplacian operator approximation on the performance of finite-difference time-domain schemes for Maxwell's equations," Dec. 2006, submitted.

[39] ——, "A three-dimensional finite-difference time-domain scheme based on a transversely extended curl operator," *IEEE Trans. Microwave Theory Tech.*, Dec. 2006.

[40] G. Kron, *Diakoptics: The Piecewise Solution of Large-Scale Systems.* London: MacDonald, 1963.

[41] R. Mittra and S. W. Lee, *Analytical techniques in the theory of guided waves.* New York: Macmillan, 1971.

[42] D. Su, J.-S. Park, Y. Qian, B. Houshmand, and T. Itoh, "Waveguide bandpass filter analysis and design using multimode parallel FDTD diakoptics," *IEEE Trans. Microwave Theory Tech.*, vol. 47, no. 6, pp. 867–876, June 1999.

[43] G. P. Tolstov, *Fourier Series.* Dover, 1976.

[44] I. S. Gradshteyn and I. M. Ryzhik, *Tables of integrals, series, and products*, 5th ed., A. Jeffrey, Ed. Academic Press, 1994.

[45] R. E. Mickens, *Nonstandard finite difference models of differential equations.* World Scientific, 1994.

[46] R. E. Mickens, Ed., *Advances in the applications of nonstandard finite difference schemes.* World Scientific, 2005.

[47] I. Saitoh, Y. Suzuki, and N. Takahashi, "The symplectic finite difference time domain method," *IEEE Trans. Magn.*, vol. 37, no. 5, 2001.

[48] I. Saitoh and N. Takahashi, "Stability of symplectic finite-difference time-domain methods," *IEEE Trans. Magn.*, vol. 38, no. 2, 2002.